Fabrication and Characterization of Wafer-Level Gold Thermocompression Bonding

by

Christine H. Tsau

S.B., Materials Science and Engineering
Massachusetts Institute of Technology, 1998

Submitted to the Department of Materials Science and Engineering
in partial fulfillment of the requirements for the degree of

Doctor of Philosophy

at the

MASSACHUSETTS INSTITUTE OF TECHNOLOGY

September 2003

MASSACHUSETTS INSTITUTE OF TECHNOLOGY
JAN 07 2004
LIBRARIES

© Massachusetts Institute of Technology 2003. All rights reserved.

Author .....
Department of Materials Science and Engineering
August 8, 2003

Certified by 8/8/03
Martin A. Schmidt
Professor of Electrical Engineering
Thesis Supervisor

Certified by .....
S. Mark Spearing
Associate Professor of Aeronautics and Astronautics
Thesis Supervisor

Accepted by .....
Harry Tuller
Chairman, Department Committee on Graduate Students

ARCHIVES

Fabrication and Characterization of Wafer-Level Gold Thermocompression Bonding

by

Christine H. Tsau

Submitted to the Department of Materials Science and Engineering
on August 8, 2003, in partial fulfillment of the
requirements for the degree of
Doctor of Philosophy

Abstract

Packaging is an important aspect of microelectromechanical systems (MEMS) design. As MEMS devices traverse multiple energy domains, sometimes operating in hostile conditions, the need to maintain reliability and functionality makes packaging a challenging problem. Often, the package needs to be specially designed for each device. Given the typically low volume productions, the packaging cost can often exceed the device cost. One way to lower that cost is to package at the wafer-level. This thesis explores a low temperature wafer bonding technique: thermocompression bonding.

This technique relies on the applied pressure and temperature to forge a bond. The pressure brings two surfaces into close proximity while the temperature reduces the pressure requirement to deform the surface asperities. In this work, gold thin film was used to bond two silicon substrates. The thesis discusses the fabrication process, its associated challenges, and provides guidelines to achieve successful bonding. Characterization of the process focused mainly on the effects of bonding temperature (260 to 300°C), pressure (1.25 to 120 MPa) and time (2 to 90 min). The resultant bond was quantified using a four-point bend-delamination technique. High bond toughness was obtained and the bond quality was found to improve with increases in the bond temperature and pressure. However, non-uniform bonding was observed. Using finite element analysis, correlation between the mask layout and non-uniform pressure distribution was found.

The four-point bend-delamination technique was also evaluated for its effectiveness in measuring high toughness bonds. Non-ideality in the load-displacement behavior were observed due to the variation in the bond toughness. A cohesive zone model was used to model the fracture process. The finite element results showed qualitative agreement with experimental data. The results also indicated that the technique is not well suited for bonds with large variations in bond toughness.

Thesis Supervisor: Martin A. Schmidt
Title: Professor of Electrical Engineering

Thesis Supervisor: S. Mark Spearing
Title: Associate Professor of Aeronautics and Astronautics

Acknowledgments

This thesis is a formal record of my research activity. But it is also a product of my interaction with many people in the past 5 years. Everyone associated with MTL and TELAC has in some ways enriched my graduate experience, has helped and encouraged me along the way. But there are few individuals who really shaped my MIT experience and whom I would like to acknowledge.

First, I would like to thank Marty and Mark for taking me on when I knew little about MEMS or research. Besides providing technical and professional guidance, they also gave me opportunities to explore and learn about myself. Their support in these endeavors will benefit me for years to come. Marty and Mark are also responsible for assembling a group of talented individuals. The discussions with everyone in the groups, past and present, broadened my horizons, and our social interactions made a big difference on my happiness scale. In particular, Joel and Samara had helped orient this clueless senior to the ins and outs of the group and MTL and they are very much the role models I look up to. Jo-Ey was instrumental in solving the source spitting mystery, and Sam always had ready answers for so many things. I could count on fruitful discussions on mechanics with Kevin, and always felt better after running sanity checks by him. Jeremy initiated me on the quest of the cohesive zone modeling.

I would like to thank members of my committee, Profs. Thompson and Suresh, for their advice. I benefitted from discussion with students in their labs. Rob kindly provided access to their busy Tencor for the stress measurements. Dr. O'Handley, for his advice and support early on. I also got plenty of help from various post-docs. Hyung-Soo built the 3-D model on bonding and answered my incessant questions on ABAQUS. Rebecca taught me all the tricks on transparency mask making, and Arturo helped me create the first process.

Without Vicky and the MTL staff, there wouldn't be any experiments. Kurt assisted in countless ways. Barry helped me get comfortable with the sometimes temperamental e-beam. Tom and Dennis kept me informed on the quirky tool-of-the-day and saved me many a times when I had to have wafers STS etched. John always made sure the testing equipment down in TELAC was setup properly. Anne, for facilitating the paper work and keeping track of various meeting schedules and SRC filings.

A special thanks goes to Qingda, for providing the fortran code and making himself so readily available as I learned about the program and how to modify the code.

The friends I have made through all the years I've been at MIT helped me maintain my sense of equilibrium through this sometimes bumpy ride. LW, for reading many of the initial drafts, and being there, for events big and small. Finally, to Mom, Dad, and T.: thank you for your love, encouragement and faith.

Contents

1 Introduction **13**

1.1 Low-Temperature Wafer Bonding 14

1.1.1 Direct Bonding 14

1.1.2 Anodic Bonding 15

1.1.3 Solder/Eutectic Bonding 16

1.1.4 Thermocompression Bonding 17

1.1.5 Gold Thermocompression Bonding 18

1.2 Bond Strength Measurements 19

1.2.1 Razor-Blade Test 20

1.2.2 Four-Point Bending 21

1.3 Scope of the Thesis 23

2 Fabrication **25**

2.1 Process Flow 25

2.2 Substrate Etches 29

2.3 Silicon Diffusion 31

2.4 Image Reversal Process 32

2.5 Gold Deposition Process 34

2.6 Gold Film Characterization 35

2.6.1 Grain Size and Surface Roughness 36

2.6.2 Film Stress 37

3 Mechanical Testing **41**

3.1 Mixed Mode Fracture 41

3.2 Crack Path and Interfacial Toughness 43

3.3 Material Systems Examined Using Four-Point Bend 44

3.4 Testing Procedure 45

3.5 Areal Correction in $\mathcal{G}_c$ 46

3.6 Determination of P_c 47

4 Bond Toughness Characterization **49**

4.1 Factors That Influence Bond Quality 49

4.2 Thickness Effect 50

4.2.1 Experimental Procedure 50

4.2.2 Results 50

4.3 Repeatability 52

4.3.1 Experimental Procedure 52

4.3.2 Results 53

4.4 Pressure and Temperature 55

4.4.1 Experimental Procedure 55

4.4.2 Results 56

4.5 Bond Time 62

4.5.1 Experimental Procedure 62

4.5.2 Results 63

4.6 Discussion and Conclusion 64

5 Finite Element Modeling **67**

5.1 Asymmetric Delamination 67

5.1.1 Modeling Environment 68

5.1.2 Simulation Results 69

5.2 Non-ideal Load-Displacement 69

5.2.1 Cohesive Zone Model 70

5.2.2 Model Description 72

5.2.3 Traction-Separation Law 74
5.2.4 Simulation Results 75
5.2.5 Fracture Simulation Conclusions 82
5.3 Bond Pressure Distribution 83
5.3.1 Model Description 84
5.3.2 Result and Discussion 84
5.4 Conclusion 89

6 Conclusions **91**
6.1 Thesis Summary 91
6.2 Process Guidelines 94
6.3 Future Work 95

A Fabrication flow **97**

B MATLAB code: Fractured surface image processing **99**

C ABAQUS code: Fracture process **107**

D FORTRAN code: Cohesive zone model **113**

E ABAQUS code: Bonding simulation **125**

Bibliography **135**

List of Figures

1-1 Schematic of a typical four-point bend specimen. 22

2-1 Schematic of the process flow 27

2-2 Schematic of the bond stack 28

2-3 Wafers with patterned lines bonded orthogonally 29

2-4 Schematic of specimens under loading, in the near notch region. . . . 30

2-5 SEM images of the gold surface without the SiO_2 barrier layer 32

2-6 Resist profiles from two different exposure times 34

2-7 SEM image of gold balls on the surface due to source spitting. 35

2-8 AFM image of as deposited, 0.5 μm thick film 36

2-9 AFM images of specimens annealed at 300°C for 10 min 37

2-10 Stress of blanket gold film as a function of temperature. 39

3-1 Experimental load-displacement curve exhibiting ideal behavior . . . 47

4-1 $\mathcal{G}_c$ vs. gold bond layer thickness 51

4-2 SEM images of the fractured surfaces of a specimen with 0.72 μm thick bond layer 52

4-3 IR image of a wafer pair with lines bonded orthogonally 53

4-4 $\mathcal{G}_c$ vs. n/N for 7 wafers bonded at 300°C and 73 MPa for 10 min. . . 54

4-5 $\mathcal{G}_c$ vs. n/N of 7 wafers bonded at 300°C and 73 MPa for 10 min . . . 56

4-6 $\mathcal{G}_c$ vs. n/N of all specimens bonded at 260°C 57

4-7 $\mathcal{G}_c$ vs. n/N for all of specimens bonded at 300°C 58

4-8 Fractured surface of poorly bonded pads. (a) Region with adhesive failure. (b) Signs of deformation visible only at the edges of the lines. 60
4-9 Fractured surface of pads showing both fracture modes 61
4-10 Bond quality of specimens bonded under various conditions. 62
4-11 Fractured surface showing high plastic deformation 63
4-12 $\mathcal{G}_c$ vs. n/N with varying bond time 65

5-1 Mesh of the ideal four-point bend model used in FRANC. 68
5-2 $\mathcal{G}_{tot}$ vs. crack length for symmetric and asymmetric crack propagation. 70
5-3 Schematic of a mode I traction-separation law used by Yang *et al.* . . 71
5-4 Mesh of four-point bend model with periodic bonds. 73
5-5 Schematic of geometries explored in the simulation. (a) Continuous bonds. (b) Periodic bonds. (c) Periodic bonds with spaces. 73
5-6 Schematic of the user element that defines the gold bonding layer. . . 74
5-7 Schematic of the traction-separation law used in the simulations . . . 75
5-8 Load vs. displacement of continuous bonds with toughness of 8.2 J/m^2. 77
5-9 Load vs. displacement of periodic pads with constant toughness. . . . 78
5-10 Load vs. displacement of orthogonally bonded pads with constant toughness. 79
5-11 Load vs. displacement of orthogonally bonded pads with varying toughness. 80
5-12 2-D mesh of the bonding process model. 85
5-13 Average pressure per pad. 86
5-14 Displacement of the wafer in the diesaw alley. 87
5-15 Mesh for the local 3-D model. Courtesy of H.-S. Moon. 88
5-16 Pressure distribution in the pads from the 3-D model. Courtesy of H.-S. Moon. 88

List of Tables

2.1 Concentration of Si with varying SiO_2 thickness 33

3.1 Example of material systems reported in literature 45

4.1 Fabrication details of specimens bonded at 300°C and 73 MPa 55

4.2 Bond temperature and applied pressure (on gold) 55

4.3 Fabrication details of specimens bonded with varying temperature and pressure 58

4.4 E-beam chamber pressure prior to Ti deposition and during Au deposition 59

5.1 Traction-separation law parameters. 76

5.2 Toughness assignment in toughness variation simulation 79

Chapter 1

Introduction

Packaging is an important yet often overlooked aspect of microelectromechanical systems (MEMS) device design. Unlike integrated circuits, these devices have mechanical and electrical components that operate in a wide range of environments. Some may require a vacuum for optimal performance; few may interface with corrosive or biological agents; still others may have delicate structures that need protection from harsh processing such as dicing. Each device requires a unique packaging scheme. Based on these considerations, it is not surprising that packaging often constitutes over 70% of the total MEMS device cost [1].

One way to lower this cost is to package at the wafer-level. As with die-level packaging, the device wafer is bonded to another substrate. However, packaging at the wafer-level permits simultaneous capping of multiple devices in a controlled environment and under a desired pressure. Throughput is increased and devices are protected from back-end processes. Furthermore, by combining through-wafer via technology with wafer-level bonding, devices are ready for standard ceramic or plastic housing upon dicing. This greatly simplifies the packaging process. Wafer bonding became an active area of research in the 1980's and has enhanced MEMS fabrication technology. This thesis focuses on thermocompression bonding and the development of a mechanical testing procedure to probe the relationship between process and property.

This chapter begins with an introduction to the various low temperature wafer

bonding techniques and their applicability to device packaging. The discussion continues with a survey of thermocompression bonding as reported in the literature. Several bond strength measurement techniques are presented next. The chapter concludes with an outline of the remainder of the thesis.

1.1 Low-Temperature Wafer Bonding

The joining of two substrates can be achieved directly or via a thin film intermediary. Although the bonding mechanisms depend on the interfacial materials, wafer bonding methods can be broadly categorized into 4 groups: direct, field-assisted, solder/eutectic and thermocompression. Direct bonding joins two substrates without a bonding layer, which is in contrast to solder/eutectic bonding, which relies on the low melting temperature of the bonding material. Field-assisted bonding, also known as anodic bonding, is a method in which an applied electric field enables the bonding between an insulating and a conducting substrate. Lastly, thermocompression bonding refers to the simultaneous application of heat and pressure during the bonding process. This section provides an overview of each category. Bonding involving polymers tends to be a low temperature process, e. g. [2, 3, 4, 5], but good hermeticity generally cannot be realized [6]. Therefore, it will not be discussed.

1.1.1 Direct Bonding

The most prominent example of direct bonding is silicon direct bonding. Successful Si-Si and Si-SiO_2 bonds were first demonstrated in 1986 by Shimbo *et al.* [7] and Lasky [8], respectively. The weak hydrogen and Van der Waals bonds formed upon room temperature contact are strengthened after a high temperature anneal, usually in the ranges of 700 - 1100°C [9], resulting in wafers that have electrical and mechanical properties similar to those of bulk silicon. However, this method places stringent requirements on contamination control and the cleanliness, smoothness and flatness of the bonding surfaces [10, 11]. Moreover, the high annealing temperature renders this unacceptable for packaging applications.

In the past few years, several groups have worked to lower the temperature requirement. Gösele *et al.* obtained a surface energy similar to that of a high temperature bond (around 3 J/m^2) by contacting the wafers under a few mbar of vacuum and over 60 hours of anneal at 150°C [10]. Surface activation with oxygen or argon plasma is another route being pursued. An hour long post-bonding anneal between 200 and 400°C results in surface energy around 2 J/m^2 [12]. Without annealing, surface energy reaches a maximum of 1 J/m^2 after 24 hours at room temperature [13]. Bengtsson *et al.* reported such wafers to be robust enough for handling in solutions such as water rinse, resist developer, acetone, Au/Cr etchant, EPW etchant and fuming nitric acid. They also demonstrated bonding of quartz and oxidized silicon wafers with similar plasma treatments [13]. Plasma assisted, room temperature bonding is intriguing. However, oxygen and argon plasma exposure produces several nm of oxide on the surface [13], which may be detrimental to some electrical and mechanical components. Moreover, plasma can damage or etch materials on the wafer. Selective shielding of plasma is often difficult since contact is made immediately after plasma treatment. Also, it is not clear whether 1 J/m^2 is sufficient for packaging needs. Lastly, stringent requirements on the cleanliness and flatness of the surfaces remain. Gui *et al.* showed that the bondability of room temperature direct bonding rests on a dimensionless parameter, which requires a surface to have surface roughness less than 1 nm and minimal surface asperities [14].

1.1.2 Anodic Bonding

Introduced in 1969 by Wallis and Pomerantz, anodic bonding uses electrostatic attraction to pull the bonding surfaces together [15]. It is a common technique for bonding of silicon and metals with glass. A typical glass-silicon bonding consists of applying an electric field of 100-1000 V across the structure, at temperatures between 300-400°C [16, 17]. The silicon is held at a positive potential with respect to the glass, driving away the mobile sodium ions from the interface. An electric field is thus formed at the interface, which draws the two surfaces together. Anodic bonding is less sensitive to surface irregularities and particulates than silicon direct bond-

ing. However, the thermal coefficient of expansion of the substrates must be closely matched to minimize induced thermal stress. This is why Corning 7740 Pyrex, whose thermal coefficient of expansion (3.25e-6) is closely matched with Si (3.5e-6) near 300°C, is the most commonly used glass material [6, 18]. Another way to reduce the thermal mismatch is to use a sputtered glass on Si, which also allows for a decrease in the bonding voltage [17].

The application of high voltage is an important concern in some cases. For packaging applications, the glass is often used as the capping wafer. Schjølberg-Henriksen *et al.* found significant leakage current in the MOS capacitors from wafers that were bonded with 800 V at 400°C for 10 min when the gap between the glass and gate oxide is small (10 μm) [19]. Attention must then be paid in the design to ensure electric field shielding or larger separation between glass and device substrates. Lastly, glasses can outgas at a rate of 10^{-6} L-Torr/m^2-sec at room temperature. For applications that require hermetic sealing, the glass must be outgassed at elevated temperature prior to bonding to ensure reliability [20].

1.1.3 Solder/Eutectic Bonding

Eutectic or solder bonds are fairly low temperature processes and are less susceptible to particulates and surface roughness than direct bonding [11]. In addition, common solder materials are also conductive, which provides an electrical connection between the device and package. Hard solders are often preferred over soft solders such as Sn-Pb because the latter's susceptibility to thermal fatigue reduces their reliability [21]. Common hard solders are Au-Sn, Au-Ge and Au-Si, which have eutectic temperatures of 280°C, 361°C and 363°C, respectively [22]. Solder bonding relies on good wetting between the solder and the substrate near the eutectic temperature. However, oxide formation on any component will prevent proper wetting, which leads to poor bonding [22, 23]. Silicon, germanium and tin oxides are readily formed under ambient conditions. Rubbing or brazing of the surfaces is thus required for reliable bond formation. This must be well controlled, otherwise voids or inhomogeneity in the bonding layer will be introduced [22].

1.1.4 Thermocompression Bonding

In analyzing room temperature direct wafer bonding, Gui *et al.* stated that the three relevant factors are surface energy of adhesion, surface roughness of both surfaces and material deformability [14]. While the surface energy and roughness of the materials are difficult to modify beyond certain limits, deformation of the material can be achieved over wide ranges by the application of pressure or temperature. The pressure not only enhances the deformation of the bonding material so local asperities can be accommodated, it also affects the substrate as a whole. Wafer bow may be reduced under pressure, thus facilitating contact between the surfaces. For most materials used as bonding interlayers, the limited plastic deformation at room temperature requires high applied pressure for bonding to occur. When the process temperature is raised, the pressure requirement can be relaxed. The simultaneous application of pressure and temperature – thermocompression bonding – thus allows bonding under conditions that otherwise would not be achieved by one parameter alone.

The thermocompression technique has been used by several groups to lower the bonding temperature for a variety of materials. While the fundamental challenges associated with each bonding method remain – such as cleanliness and surface roughness issues for silicon and glass direct bonding and surface oxide formation for solder bonding – the utilization of pressure reduces the annealing temperature required to achieve good bonding, as will be shown in the next couple of examples.

Li and Bower combined plasma activation with thermocompression to achieve low temperature bonding of silicon [24]. Following plasma activation, bonding surfaces were brought together and bonded under greater than 0.4 MPa of pressure at 200°C for 30 minutes. This was followed by a 24 hour anneal at 200°C to ensure a surface energy greater than 1 J/m^2, although the effectiveness of the anneal was not reported[1]. Direct bonding of glass at lower temperatures using thermocompression was also demonstrated. Sayah *et al.* bonded microscope glass slides under applied pressures between 6 and 50 MPa and temperatures between 100 and 200°C [25]. After 12 hours,

[1]This is comparable to the 1 J/m^2 reported by Bengtsson and Amirfeiz in their plasma activated process with 24 hours storage at room temperature [13].

bond strengths better than those from HF-assisted or plasma-assisted bonding were obtained. However, it was lower than the values they measured on fusion-bonded glass at 600°C.

Pressure also allows for solder bonding below the eutectic temperature. Au-Sn solder was bonded at 240°C in 20 minutes with 0.4 MPa of pressure [22] and Al-Au bonds were made at 350°C under 45 MPa for 30 min [26]. Both were die-level bonds. Another variation on thermocompression is localized bonding of silicon to glass with an Al intermediary. Cheng *et al.* used Pyrex glass to cap the silicon chip, which contained a resonator device with Al selectively deposited on micro-heaters [27]. An applied pressure of 0.2 MPa and heat supplied by the micro-heaters resulted in the bonding of Al with Pyrex after 10 minutes. Good vacuum sealing was obtained. This was packaged at the die-level; it is not known if parallel heating could be effectively carried out at the wafer-level.

1.1.5 Gold Thermocompression Bonding

Thermocompression has been a standard microelectronics packaging technique, in both wire and tape automated bonds. While several materials are bondable under modest temperature and pressure, bonding is easier to achieve in some materials than others. For instance, the oxides that naturally occur on the surface of solders prevent the formation of a strong bond. For successful bonding, these oxides must be removed either chemically or mechanically. Consequently, oxidation resistant materials such as gold are often preferred. The low yield stress of pure gold aids the thermocompression process, and its corrosion resistance and electrical conductivity are desirable properties for packaging. In addition, gold does not attract inorganic substances such as slurry particles [28]. Lastly, as a metal, gold is expected to be effective as a hermetic sealing material [6].

Thermocompression bonding of gold was first used in wire-bonds. Jellison examined the effects of UV-ozone pre-bonding treatment and post-bonding anneal on bond strength [29]. Condra *et al.* studied the deformation properties of gold to understand better the thermocompression process [30]. When larger arrays of bonds became de-

sirable, studies on bump-lead bonds began. Kim *et al.* bonded 328 contacts to tape automated bonding leads and reported pressure and duration as important bonding parameters [31].

All of the studies cited thus far were for die-level bonds. True large array bonding of bumps was described by Furman and Mita, where up to 60 000 contact pads were bonded on 127 mm x 127 mm ceramic substrates using a heated press [32]. The minimum pressure of 0.689 MPa was applied for as long as 3 hours, with 1 hour at the peak temperature of either 400 or 375°C and a peak pressure that ranged from 0.689 to 2.76 MPa. These are the pressures that were applied to the substrate. Since the actual bonding area was some fraction of the bond pads, each 150 μm x 450 μm, the actual bonding pressure on the Au was greater than the peak pressure reported.

Gold bumps for tape automated bonding tend to be thick (> 20 μm). One demonstration of thin film bonding was in the sealing of capacitive pressure sensor dice: pressure of approximately 2 MPa was applied to 1.2 μm thick gold at 350°C for 2 min [33]. Very little work has been reported on bonding at the wafer-level. Drost *et al.* reported a pressure of 0.06 MPa at the wafer-level as insufficient for continuous bond formation: bonds were highly localized and on the micrometer scale [34]. At the chip-level, 4 μm Au films were bonded for 1 min with varying temperatures and pressures on the Au, from 350 to 450°C and 0.32 to 17.86 MPa, respectively. An increase in daisy chain resistor yield was reported for pressures up to 1 MPa; further increases in pressure or temperature showed little benefit. However, additional bonding time was found to improve bond homogeneity [34].

This thesis investigates wafer-level bonding using a thin film approach for the gold deposition. Although the gold on Si-substrate process will be described, it will be clear that the process is transferable to other substrate materials.

1.2 Bond Strength Measurements

In order to understand the correlation between process parameters and bond quality, it is important to develop a bond strength measurement technique. The technique

must be robust and quantitative as well as sensitive so that slight effects of the process can be detected. Several techniques have been reported for bond strength measurements. A brief discussion of each is given, followed by the technique that is used in this work.

One way to determine the bond strength is to measure the strength of the material. Shimbo *et al.* used a blister test by applying hydrostatic oil pressure to a hollowed silicon chip that was bonded to a through-holed silicon disk. The measured fracture strength was taken as the adhesion strength [7]. Tensile testing is another option. The specimen is bonded to a slightly smaller stub, which is pulled normal to the bonding interface until rupture. This test is sensitive to the alignment of the stub. Any flaws along the edges of the specimen, which could be incurred during dicing, also can lead to premature failure, resulting in inaccurate measurements [10].

Bond strength can also be determined through fracture mechanics methods, based on the idea that crack propagation changes the potential energy of the material. Fracture creates free surfaces, with an associated surface energy, γ. That is balanced by the energy of an external load and a reduction in the stored elastic strain energy in the material. The change in the total potential energy with area is known as the strain energy release rate and can be viewed as the driving force for crack propagation. Cracks do not propagate until the critical strain energy release rate, $\mathcal{G}_c$, is reached. Therefore, $\mathcal{G}_c$ and γ both provide a measure of the mechanical integrity of the bond. Techniques for measuring $\mathcal{G}_c$ and γ are described in the next two sections.

1.2.1 Razor-Blade Test

By far the most popular measurement technique used by the wafer bonding community is the razor-blade test. First described by Maszara *et al.*, this is an easy test to perform in which the insertion of a razor blade results in a crack length opening that is measurable in the IR [35]. The crack length is related to the surface energy, γ:

$$\gamma = \frac{3}{8}\frac{Et^3y^2}{L^4}, \tag{1.1}$$

where E is the Young's modulus, t is the thickness of the wafer, y is half of the blade thickness, and L is the measured crack length.

There are several shortcomings with this method, however. The razor typically cannot be forced between the wafers in high toughness bonds, resulting in only a qualitative description of whether the bond is "good" or "bad". But when quantitative toughness can be obtained, comparison between research groups is difficult because measurements rely on factors that are often not reported, such as the distance and how the blade is inserted, and measurement conditions [36]. Humidity is known to affect the observed surface energy considerably in systems that are known to suffer environmental corrosion, such as glass (and oxide) [10]. The second issue is that it is often difficult to keep the blade perfectly perpendicular to the interface so that the crack front is straight and parallel to the flat edge of the blade. Moreover, the insertion distance of the blade affects the measured surface energy: it is much higher close to the edge of the wafer, and decreases to an asymptotic value around 5 mm away from the wafer edge [36]. Some of the variability in the measurements can be removed with the modification suggested by Pasquariello and Hjort, which replaces the blade with built-in mesa spacers [36]. However, the fundamental relationship between γ and L^4 in Equation 1.1 remains. The demand for accurate measurement of the crack length using IR wavelengths greatly compromises the utility of the razor-blade technique. Measurement accuracy and wafer-to-wafer variation in surface quality induce experimental errors on the order of $\pm$ 15% [37].

1.2.2 Four-Point Bending

A test method that eliminates the crack length measurement is the four-point bending test. In 1989, Charalambides *et al.* presented a test procedure for the measurement of interfacial fracture resistance [38]. The specimen is a bimaterial beam with a through-thickness, central notch in one of the layers, and a precrack along the interface, as shown in Figure 1-1. Four point loading establishes a constant moment condition in the region between the inner rollers. Once the crack length has significantly exceeded the thickness of the upper layer, the crack propagates at a constant velocity under

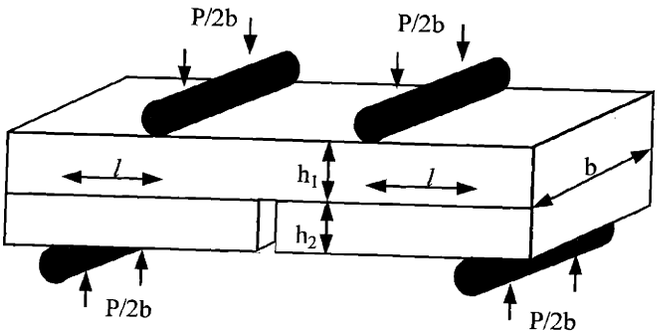

Figure 1-1: Schematic of a typical four-point bend specimen.

a constant load, and the strain energy release rate reaches steady state. The crack then decelerates upon reaching the region between the inner and outer loading points. Further propagation would require increase in the load [38].

Based on the beam theory, the strain energy release rate of the specimen in steady state can be given by an analytical expression, simplified from the general form in [38] for the case of homogenous beams:

$$\mathcal{G}_c = \frac{1.5(1-\nu^2)}{E}\left(\frac{P_c\, l}{b}\right)^2\left(\frac{1}{h_1^3} - \frac{1}{(h_1+h_2)^3}\right), \tag{1.2}$$

where P_c is the critical load at which crack propagation occurs, l is the distance between the inner and outer rollers, b is the width of the specimen, and E, ν, h_1 and h_2 are the Young's modulus, the Poisson's ratio, the thickness of the unnotched wafer and notched wafer, respectively. Equation 1.2 shows $\mathcal{G}_c$ as functions of the specimen geometry and applied load, both of which can be measured quite accurately by commercially available equipments.

This technique has been used to determine the bond toughness by a number of groups. The expected crack propagation at constant load, given a constant interfacial fracture energy, has been observed experimentally. This is the technique used to characterize toughness of bonds in this thesis. More background on the technique is provided in Chapter 3.

1.3 Scope of the Thesis

The primary goal of this thesis is to characterize wafer-level thermocompression bonding. An attempt is also made to provide users of the technique with guidance regarding process optimization to achieve high quality bonds for packaging application needs. These goals require a fabrication process and a methodology for quantifying the resultant bonds. The characterization thus focuses on the mechanical integrity of the bonds, rather than metrics such as electrical functionalities of devices or reliability of the bonds. A fabrication process has been developed to explore the process space, with consideration to the needs of the mechanical test specimens.

Chapter 2 describes the fabrication process, related challenges and materials characterization of the gold film thus fabricated. Chapter 3 provides more theoretical background on the mechanical testing procedure and description of the testing procedure and non-ideal load-displacement curves that were obtained experimentally. In Chapter 4, the experimental data on the effects of various process parameters are presented. Chapter 5 describes the finite element modelings that were performed in order to further the understanding of the non-ideality and variation in the data. Finally, conclusions, remarks on the accomplishments of the thesis and future work will be made in Chapter 6.

Chapter 2

Fabrication

Characterization of the wafer-level thermocompression bonds by their mechanical performance is one of the central goals of this thesis. Thus, the fabrication process was developed with consideration given to the mechanical test. This chapter will describe the fabrication process in detail, but the main fabrication steps consisted of substrate preparation, deposition of metals on Si, aligned bonding and dicing for testing. It is a relatively short process that can be easily modified on device wafers for performance studies or with substrates other than Si. Despite its simplicity, however, there are several critical steps, which are discussed in turn. Finally, characterization of the gold thus fabricated is be presented.

2.1 Process Flow

This section describes the fabrication flow; step-by-step details may be found in Appendix A. Each bond pair consisted of 4" n-type Si wafers with average thicknesses of 525 μm and 450 μm, the latter being a double-side polished (DSP) wafer.

The 500 μm wide and 60 μm deep central trench in the DSP wafer shown in Figure 2-1(a) was formed by etching the wafer in 20% KOH at 80°C. Next, a 100 μm wide, 1-2 μm deep feature was anisotropically dry etched around the perimeter of the central trench. Following the growth of approximately 3000 Å thermal oxide, both wafers were patterned with Clariant AZ5214-E image reversal resist. A 10 nm Ti

adhesion layer and 0.1 to 0.7 μm of Au were then e-beam deposited onto both wafers. After soaking the wafers in acetone, excess metals were removed by lift-off. Seven groups of 50 μm by 60 mm metal lines remained on the substrate, as illustrated in Figures 2-1(f),(g). The spacing between lines within each group was 250 μm while that between groups was $\sim$2 mm. The latter forms the diesaw alley, thus facilitating dicing of the mechanical specimens. Metals were routinely successfully lifted-off. Nevertheless, the wafers were subjected to 1 to 2 min of ultrasonic vibration to ensure complete removal of undesirable stringers, especially on DSP wafers near the trench. The major process steps and a schematic of the wafers after lift-off are shown in Figure 2-1.

Although gold does not oxidize under most conditions, organics readily adsorb onto the surface. UV-ozone was reported to be effective in removing the organic contaminants [29]. Hence, wafers were soaked for 5 min in acetone and methanol, rinsed with deionized water, spun dry and exposed to UV-ozone for 90 min immediately before wafer alignment using Alignment System from Electronic Visions. At the end of the alignment step, the wafers were held in place on a stainless steel chuck by a quartz plate that was clamped to the chuck. The quartz plate, touching the DSP wafer at three points as shown in Figure 2-2, has a wafer-shaped opening. A stainless steel pressure diffuser plate fits in that open space, on top of the wafers. A vertical separation between wafers was maintained by three triangular flags, each about 100 μm thick and 1 cm long, that were inserted between the wafers at the edges. Bonds were made in Electronic Visions AB1-PV or EV501 bonders. The bonding chamber was first purged with nitrogen, then pumped to achieve slight vacuum. Following the temperature ramp (approximately 18°C/min) and the three-minute stabilization period at the bonding temperature, a small force was applied over the wafer and the separators were withdrawn. The bonding force was then applied across the wafer for the desired time, typically 10 min. The temperature was subsequently ramped down.

The maximum pressure over a 4" wafer that could be applied by the bonders was around 0.5 MPa. But the average bonding pressure on the gold depends on the density of the contact area. In the following pages, rather than quoting the pressure

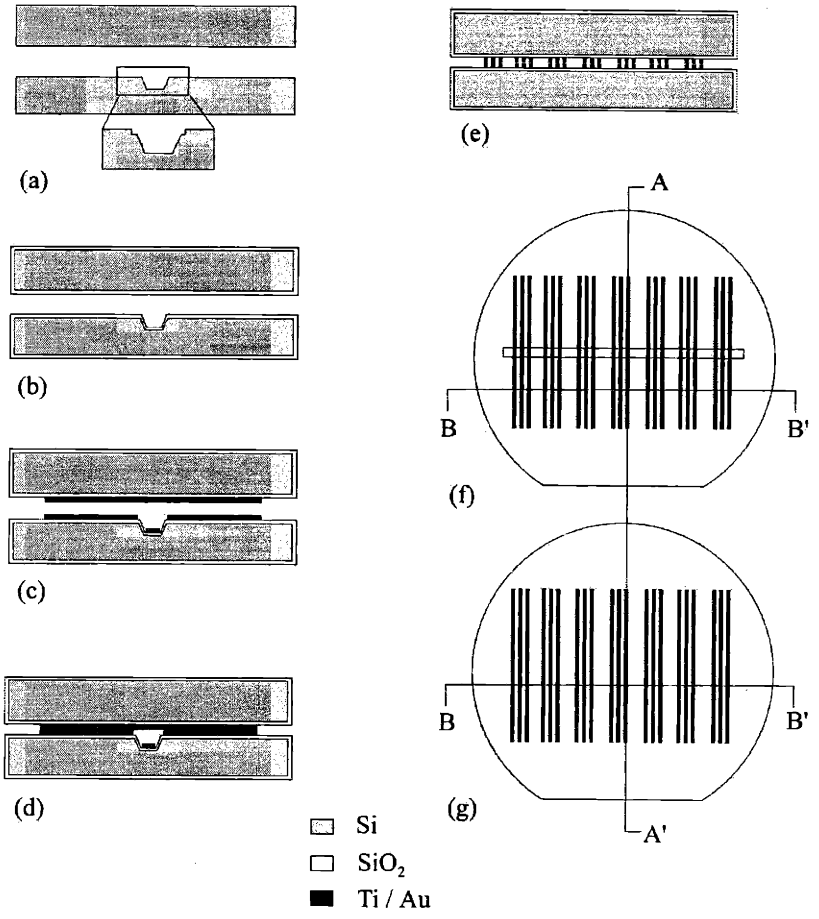

Figure 2-1: Schematic of the process flow, with cross sections taken along A-A' in (a)-(d), and along B-B' in (e). (a) Bonding pair. Detail shows notch region in DSP wafer (bottom) after KOH and shallow anisotropic etching. (b) Thermal oxidation. (c) Metal deposition. (d),(e) Aligned bonding that matched features on both wafers. (f),(g) Top view of DSP and regular wafers after lift-off, respectively. Dashed central rectangle in (f) indicates the location of the etched trench.

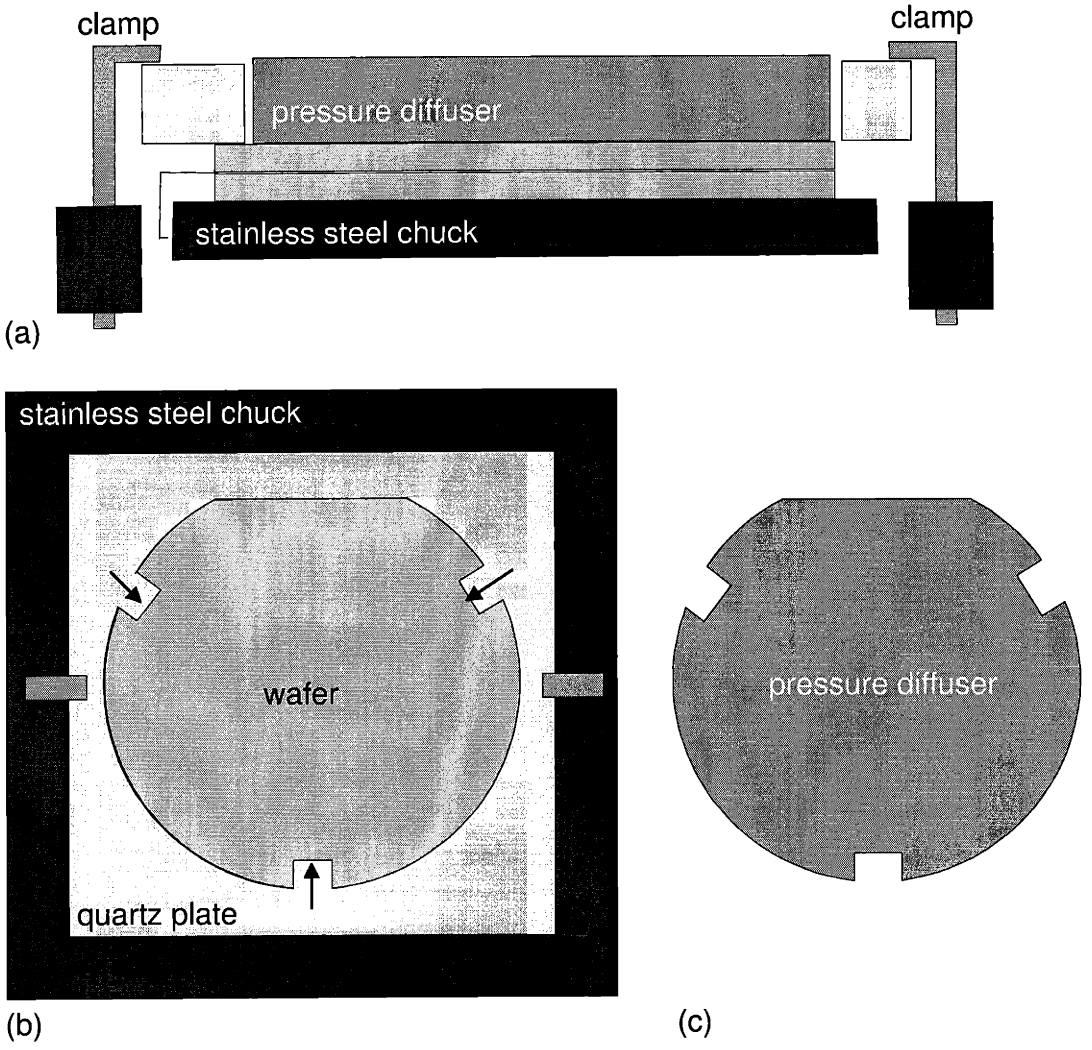

Figure 2-2: Schematic of the bond stack after alignment. Arrows in (b) indicate the location of separation flags, which are situated between the 2 wafers. (c) Stainless steel diffuser plate which fits inside the quartz plate on top of the wafers in actual bonding.

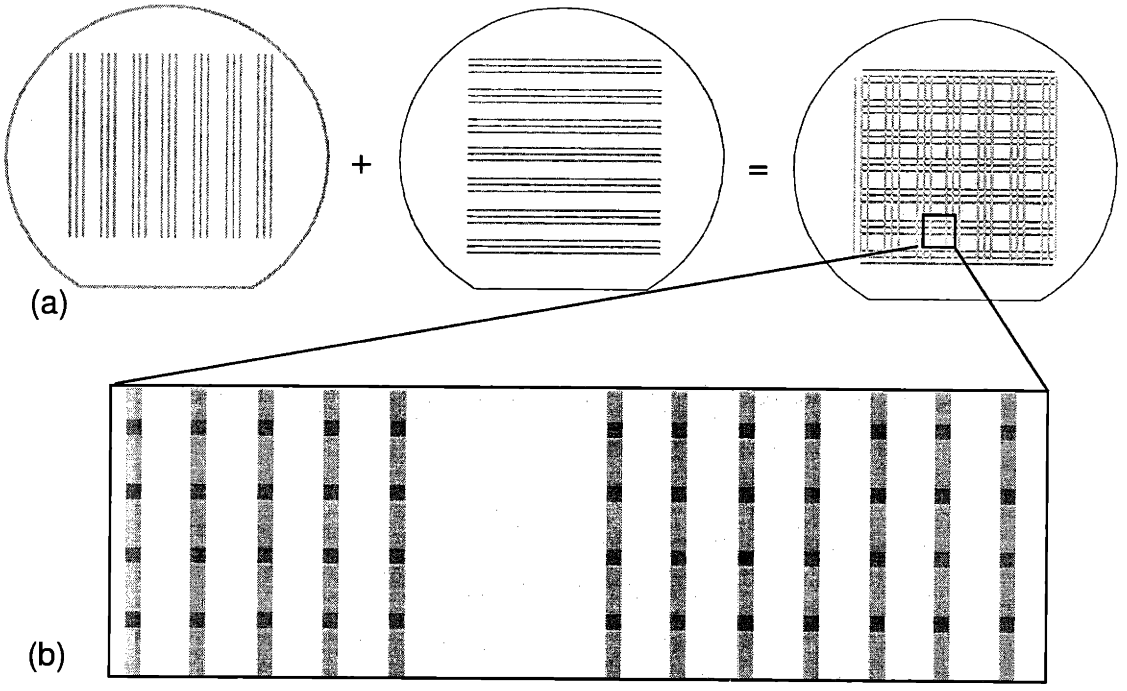

Figure 2-3: (a) Wafers with patterned lines bonded orthogonally. (b) Top view of one of the wafers, highlighting square bond pads thus formed.

applied over the wafer, the bonding pressure will refer to the pressure applied on the gold. Given the mask layout described above, when the metal lines are aligned in parallel, as shown in Figure 2-1, the maximum average bonding pressure on the gold is 7 MPa. Higher bonding pressure was achieved by aligning the patterned lines orthogonally, forming 50 x 50 μm^2 pads at the intersection of the lines, as shown in Figure 2-3. The bonding area was thus reduced to 1/6 of the parallel aligned ones, effectively allowing higher bonding pressures to be applied to the gold.

Mechanical test specimens were made by dicing the bonded wafers into 8 mm wide strips. A width-wise cut was made above the KOH-etched notch to the DSP wafer, exposing the bonded interface.

2.2 Substrate Etches

This section discusses the first two steps of the process flow described in Section 2.1, which is the etching of the DSP wafer. These steps were necessitated by the mechan-

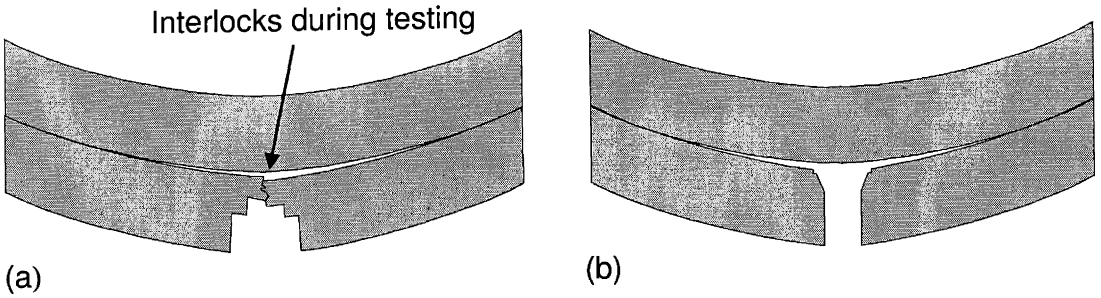

Figure 2-4: Schematic of bending specimens in the near notch region. (a) Notch made by successive diesaw cuts and three-point bending to induce a precrack. (b) Notch made by KOH etch. Possibility of mechanical interlocking during loading is eliminated.

ical testing. As described by Charalambides *et al.*, the test specimen has a notch in one of the substrates so that the interface is exposed and the crack propagates along the interface [38]. For a thin interface, as in the current specimen, dicing with micrometer scale precision across the wafer would be required. An alternative is to place the notch to within tens of microns of the interface, and then to load the specimen in a three-point bending fixture to produce a precrack that runs through the remaining ligament in the DSP wafer, and even a short distance along the interface. To confine the precrack direction and to reduce mechanical interlocking during testing, two cuts were made at the notch: a deep, wide cut of approximately 220 μm in width, followed by a 30 μm wide cut that stops approximately 30 μm away from the bond interface [39]. But the pre-cracks were not always straight, as illustrated in Figure 2-4(a), and mechanical interlocking could still occur during testing.

The solution finally adopted in the present work is to eliminate the need to manually create precracks. This was achieved by KOH etching a central trench as described. Dry etch using DRIE (deep reactive ion etching) would work as well [40], but since most etchers have single wafer handling capability, it is a much more time consuming process. The wafers were thus bonded with a central cavity at the interface, which was exposed once the notch cut met the bottom of the etched feature.

Although a depth of 60 μm is not deep by bulk micromachining standards, it caused step coverage problems with thin resist such as AZ5214-E. The resist was

found to recede from the edges of such a feature after post bake, possibly due to the change in surface tension as solvents were baked out. The pull back length was about 20 μm and the shape of the receding line was wavy and irregular. Metal would thus be deposited along the perimeter of the trench and connect the metal lines horizontally at the edges of the notch. By having a shallow recess around the perimeter, the bonding features remain separated as designed. The 1-2 μm deep and 100 μm wide feature around the perimeter of the central trench was achieved by patterning with thick resist AZ4620 (Hoechst-Celanese) and dry etched. The thick resist was used in order to etch over 1 μm deep using a standard Si etch recipe.

2.3 Silicon Diffusion

When bonds were made with unoxidized substrates, discoloration of gold was observed on portions of the wafers that failed to bond. Figure 2-5 shows discoloration concentrated at the grain boundaries. Using Auger spectroscopy, the elemental composition in those regions was identified as silicon with varying amounts of oxygen. By sputtering away the surface atoms, it was determined that the oxygen signal came from oxidation of silicon at the surface. Moreover, the signal intensity of the silicon decreased with distance into the gold. Experiments using a germanium substrate indicated that the silicon had originated from the substrate and had diffused through the gold layer.

While the eutectic temperature is 363°C, the interdiffusion of silicon and gold occurs at significantly lower temperatures. Si was observed to accumulate on the gold surface below 340°C [41]. Although the thin film stack included a Ti adhesion layer, no trace of Ti was detected despite the fact that the bonding temperature exceeded the reaction temperature of Ti and Au, which is around 200°C [42, 43]. With only 10 nm of Ti, it is possible that the Ti had completely reacted with either Au or Si (titanium silicides are relatively easy to form as well), preventing elemental Ti from diffusing through the Au layer. The presence of Si at the Au bonding surface will prevent bonding because Si hardens Au, which hampers the thermocompression

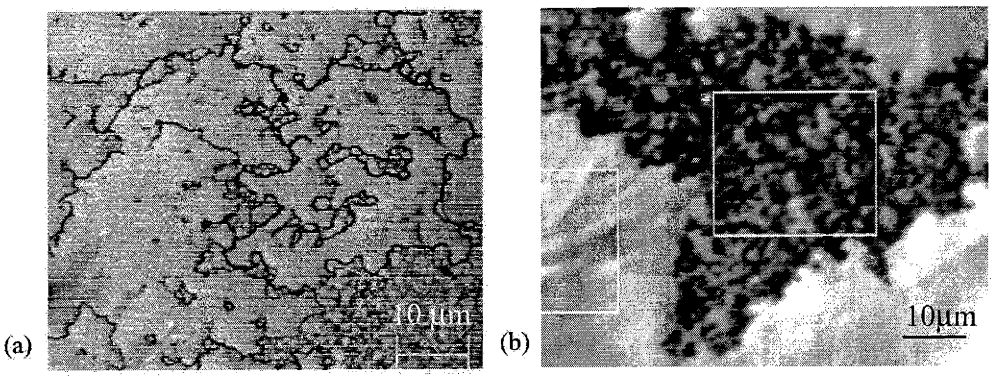

Figure 2-5: (a) SEM image of gold surface without SiO_2 barrier layer after 10 min annealing at 300°C. Si (dark regions) decorates the grain boundaries. (b) Another specimen, annealed in air, after a few sputtering cycles to remove the surface carbon.

process [31]. A diffusion barrier layer is thus needed.

Silicon dioxide was chosen as a possible candidate and a series of diffusion experiments were performed. Thermal oxides of varying thickness were grown, followed by standard photolithography and metal deposition processes. The gold thickness was kept constant at approximately 0.7 μm throughout. In order to duplicate the bonding conditions, annealing at 300 and 350°C was carried out in a tube furnace with nitrogen. Concentration of Si was obtained by multiplexing scans around the Au3 and Si2 Auger electron energy peaks. After 10 cycles of such scans, the ratio of the counts were taken. At 300°C, no detectable amount of Si was found with oxide thickness greater than 1500 Å, as shown in Table 2.1. On the other hand, Si was detected on specimens with 3000 Å thick oxide annealed at 350°C. For the bonding experiments to be discussed in upcoming chapters, approximately 3000 Å thick oxides were used and bond temperature were kept at or below 300°C.

2.4 Image Reversal Process

Patterning of films can be achieved either by lift-off or etching. The latter, a more common microfabrication technique, requires a certain selectivity of the film to the masking material in the etching environment. Lift-off is a simpler process, and the photoresist mask can be used for any metal that can be deposited. However, suc-

Table 2.1: Concentration of Si with varying SiO_2 thickness

Temp [°C]	Anneal [min]	SiO_2 [Å]	Si [%]	Note
300	10	0	35	post 2 sputter cycles
		480	6	
		1550	–	
	10	3030	–	
	30		–	
	60		–	
350	30	3030	8	
	60		13	
	100		11	

cessful patterning, especially of thick films such as those used in this work, requires a negatively sloped resist profile. If the resist profile is perpendicular, deposition on the substrate connects with those on the resist, and feature edges would be torn as excess films are removed. A negative sloped profile, on the other hand, has a wider top that would block deposition at the foot of the resist, thereby ensuring that films are deposited as disconnected features. It also allows timely diffusion of the solvent during the soak period.

Image reversal resist, such as AZ5214, is a positive resist that acts as a negative one. It requires a slightly different procedure from a standard positive resist process: after the initial exposure with a mask, the wafers are baked for a short time and the entire wafer is exposed again. The process terminates with resist development, without the usual postbake. Resists have photochemical compounds that enhance their solubility in developers after exposure to a UV source. For an image reversal resist, the initial exposure also activates the photochemical compound, transforming it to carboxylic acid. But the additional imidazole molecules in image reversal resists attach themselves to the carboxylic acid, forming a salt [44]. Upon heating and the release of CO_2, the originally exposed area loses solubility in the developer. Now, when the full wafer is exposed, the photochemical compound is activated in the originally unexposed area and dissolved away as the wafer is being developed.

Among the photolithography steps – initial exposure, bake, and flood exposure

– the slope of the resultant profile was found to be dictated by the duration of the initial exposure. Figure 2-6 shows two profiles with a difference of 10 seconds in the exposure time on a 320 nm exposure wavelength contact aligner. A longer exposure time increases the slope of the resultant profile.

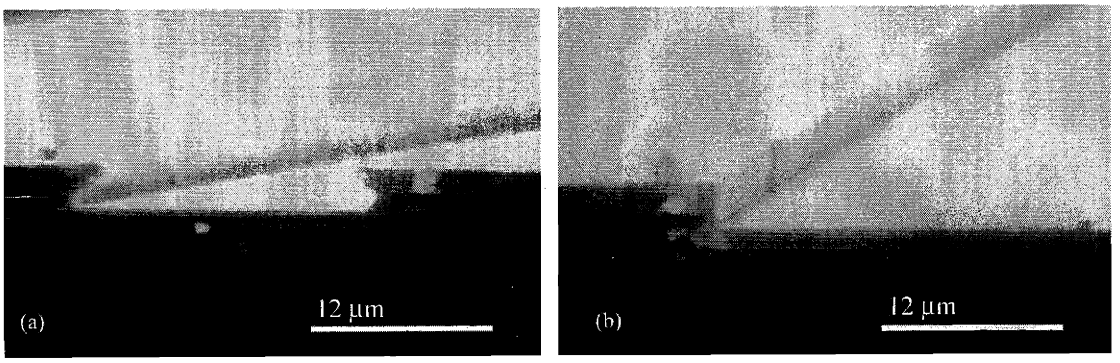

Figure 2-6: Resist profiles from two different exposure times. (a) Desired negative slope (20s exposure using an exposure wavelength of 320 nm). (b) An additional 10s exposure results in a nearly straight profile.

2.5 Gold Deposition Process

In a bonding process that requires mating surfaces to come into atomic proximity, a smooth surface is preferred. The metal deposition process used an electron beam to melt and evaporate the solid source. Nonuniform and rapid heating of the source could cause the melt to bubble and push about the remaining solid particles. These particles could be ejected from the melt, resulting in spitting [45]. Micrometer diameter sized gold balls, as shown in Figure 2-7, can thus populate the surface, which made bonding difficult.

To ensure a uniform melt prior to deposition, small amplitude rastering of the beam and a longer soaking period was implemented. In addition, the deposition rate was increased slowly (from 2 Å/s to 5 Å/s) over the first 100 nm of the deposition. Most importantly, a tungsten inner liner was added to the graphite crucible. The presence of graphite has been correlated to spitting in the evaporation of germanium and copper [46]. Instead of making modifications to the graphite crucible, gold spit-

ting was eliminated by using a refractory tungsten liner, which is inert to gold. In addition, the wetting property of gold on tungsten helps the melt to spread. This is an advantage as long as it is controlled and the melt does not overflow.

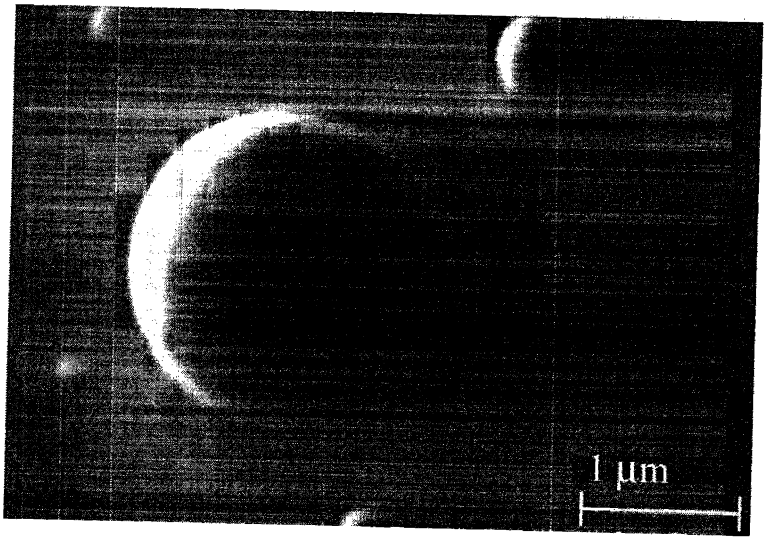

Figure 2-7: SEM image of gold balls on the surface due to source spitting.

2.6 Gold Film Characterization

As the bonding material in the thermocompression process, some understanding of the gold film is necessary. The material properties of polycrystalline thin films are closely related to their grain structure. Therefore, besides the obvious properties of interest, namely surface roughness and yield stress, the grain size of the films were measured.

Evaporatively deposited FCC materials such as gold, copper and silver tend to develop columnar structures with (111) texture. For materials with high atomic mobility such as gold, grain growth may occur even during room temperature deposition, and the grain size could scale with the film thickness [47]. However, the grain size is a strong function of the processing conditions. During deposition, not only would the target material be deposited, but any impurities in the system as well. Impurities tend to migrate to grain boundaries and impede their motion, resulting in grain

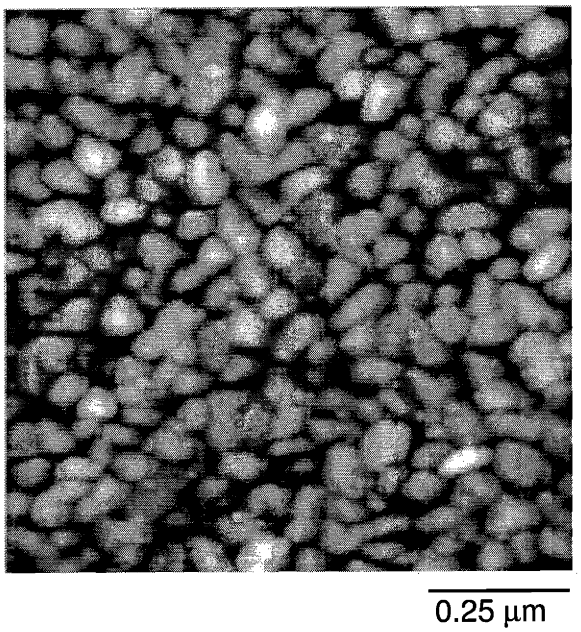

Figure 2-8: AFM image of as deposited, 0.5 μm thick film. The scan size is 1 x 1 μm^2.

boundary drag or grain growth stagnation [47]. In addition, the grain structure may be much smaller at the base of the film than on the surface.

2.6.1 Grain Size and Surface Roughness

The surface roughness of the gold film was characterized using tapping mode atomic force microscopy (AFM). A nominally 0.5 μm film deposited at a background pressure of 5 E-6 torr was found to have a surface roughness of 3.14 nm. The AFM image, Figure 2-8, shows that the grain size is on the order of 60 nm, which is comparable with those deposited at similar background pressures [48, 49]. However, given that the deposition was not in UHV condition, some impurity atoms most likely would have been incorporated in the film.

The diffusion mechanism less than 300°C was reported to be surface diffusion dominant, and has a tendency to smooth out surface features with annealing time [48]. Surface roughness were also measured on several bonded specimens in areas that were designed not to be bonded (i.e. spaces between pads when lines were bonded orthogonally). The surface roughness was reduced slightly to around 2 nm. Some

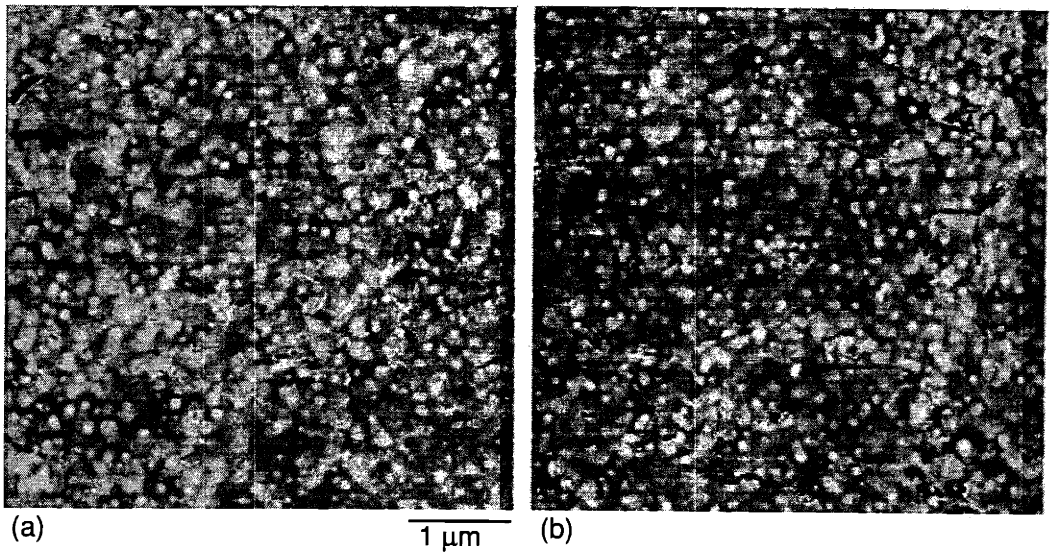

Figure 2-9: 5 x 5 μm^2 AFM images of specimens annealed at 300°C for 10 min. (a) 9D. (b) 9F (see Table 4.2)

grain growth had occurred due to the temperature treatment, although the grains were not clearly defined in the AFM images obtained. Figure 2-9 also indicates that there was some grain clustering.

2.6.2 Film Stress

The yield stress of the film at the bonding temperature is an important material property in this work. The yield stress, estimated from the stress-strain curve of films with grain size on the order 20 nm, is around 100 MPa [50]. Lozinskiy *et al.* showed the hardness decreases with annealing temperature, with increased softening observed around 300°C [51]. In these very large grained films (400-900 μm), the yield stress at 300°C was approximately 60 MPa[1]. Clearly, the strength of the film is closely tied to the grain size. The yield stress has some form of an inverse relationship to the grain size, although the exact dependence on the grain size has not been agreed on [52]. Therefore, yield stress of the film is most informative if it is measured on films fabricated by the process used in the present work.

[1]Using the approximation of yield stress as 1/3 of the hardness value, which they reported to be around 180 MPa.

Yield stress may be obtained from the hardness using an indentation technique. Nanoindentation of 0.5 μm thick films annealed for 10 min at 300°C was performed, but the hardness value was found to be a function of the indentation depth, therefore cannot be considered as a material property. A reliable value of the hardness of the films could not be obtained due to the substrate effect [53].

Another way to obtain yield stress is to find the stress as a function of temperature. Typically this could be done with a curvature measurement technique. Curvature measurement of a blanket gold film on an oxidized Si wafer was carried out using a Tencor FLX-2320 measurement system with a heating and cooling stage, at a rate of 6°C/min. Prior to the temperature cycle, the wafer was exposed to UV-ozone for 90 min, to simulate the process wafers would undergo in actual bonding. The wafer was heated from room temperature to 300°C, held for 10 min, then cooled down. Although gold does not oxidize easily, forming gas (20:80 H_2:N_2) flowed on top of the wafer during the temperature cycle. Another reference curvature reading was taken at room temperature after Au and Ti had been stripped. From the wafer curvature measurements, the stress of the 0.5 μm thick film, σ, can be then be calculated using the Stoney formula [54]:

$$\sigma = \frac{M h_{sub}}{6 h_{Au}} \left(\frac{1}{R} - \frac{1}{R_o} \right), \tag{2.1}$$

where M is the biaxial modulus of Si (1.81 GPa), h_{sub} is the thickness of the Si substrate (525 μm), h_{Au} is the thickness of the Au film (0.5 μm), R is the radius of curvature at a given temperature, and R_o is the reference radius of curvature.

Judging from Figure 2-10, where stress is plotted as a function of the temperature, there is very little stress in the gold film. At room temperature, the film is slightly tensile. At around 100°C, the film is slightly compressive, and seemed to undergo some relaxation or grain coarsening. The stress is fairly constant above 200°C, suggesting the film was deforming plastically at a constant yield (flow) stress. In the cooling cycle, however, the film behaved more as if it was covered by an elastic capping layer [55]. The stress finally seemed to plateau around 120 MPa when the film was cooled

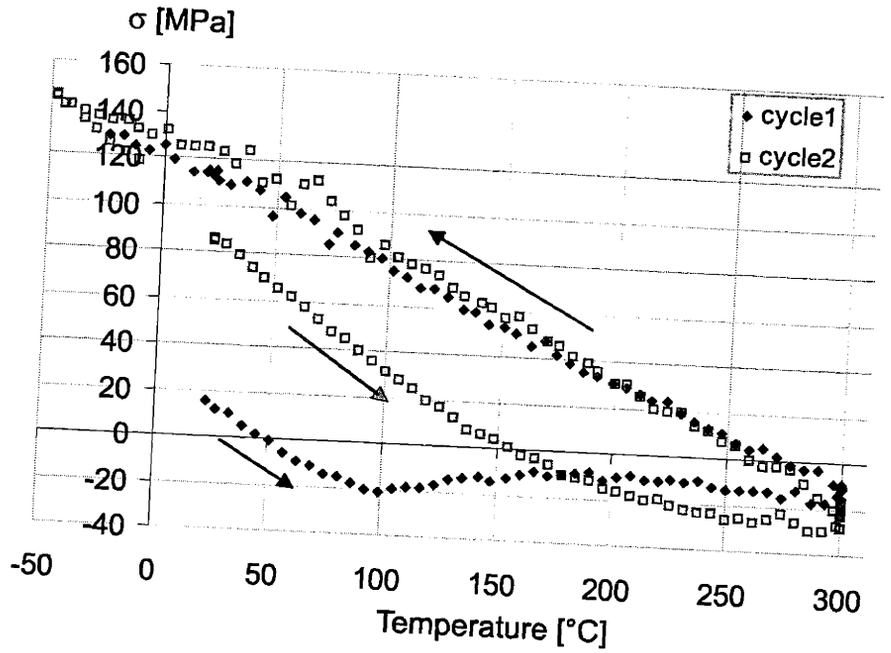

Figure 2-10: Stress of blanket gold film as a function of temperature.

to -24°C. Since the first temperature cycle is often complicated due the the various mechanisms that could take place in the film upon heating, a second heating-cooling cycle was performed one day later. Similar behavior was again found. Although Auger spectroscopy was not performed on this particular film, data from Section 2.3 indicated that the surface should be free of silicon oxide. Moreover, forming gas was used during the cycle. It is not clear why the stress-temperature curve behaved as that of a capped film in the cooling cycle. However, given the small grain size of the as-deposited film, this may be related to the amount of impurities in the film. Impurities can also impede grain boundary motion, confining them in the same fashion as a capped film would [55].

Understanding of the stress evolution in the gold film requires further study. For the thermocompression bonding process, only the stress of the first heating curve is relevant. As mentioned, film stress is highly correlated to processing. For the film fabricated by the process flow described, the flow temperature is approximately 200°C. At the bonding temperatures, the yield stress is low, taking a value well below 100 MPa.

Chapter 3

Mechanical Testing

The fracture behavior of multi-layered structures is important in a number of areas, including composites and microelectronics. Since the late 1980's, the four-point bend delamination test technique has been used to study a number of materials systems. This chapter begins by discussing some theoretical considerations of this test and experimental results found by a number of investigators in the field. The mechanical test procedure used in the thesis is described next. Finally, experimentally observed non-idealities and how they affect the interpretation of the critical load are presented.

3.1 Mixed Mode Fracture

As mentioned in Chapter 1, the main advantage of the four-point bend test is the decoupling of crack length and the critical load that promotes crack propagation. The pure bending condition, located between the inner rollers, results in mixed mode fracture. Mode mixture, Ψ, is given by

$$\Psi = \tan^{-1}\left(\frac{K_{II}}{K_I}\right), \tag{3.1}$$

where K_I and K_{II} are the stress intensity factors in mode I and II, respectively. Clearly, Ψ varies from 0° to 90° as mode changes from pure mode I to II, or from pure normal (tensile) loading to pure shear loading with respect to the direction of

crack propagation. The strain energy release rate, $\mathcal{G}$, is known to vary as a function of the mode mixture [56], and is typically lower in pure mode I. The mode mixture at the crack tip thus becomes important. The mode mixture for a typical four point bend specimen depends on the ratio of the layer thickness and modulus mismatch between the two layers. For the specimen used in this work, $\Psi \sim 41°$, which has approximately equal contribution from both modes [56].

Friction and residual stress are inevitably present in real systems. Charalambides *et al.* reported friction had no effect on Ψ in the constant moment region [57]. On the other hand, friction may result in overestimation of $\mathcal{G}_c$. They found minimal frictional effects in specimens having small ratio of total beam thickness to the moment arm; values between 0.25 and 0.5 were recommended. For the structures used in this work, that ratio is 0.0975. Charalambides *et al.* also reported that residual stress can have major impact on the toughness and mode mixture. A tensile stress in the notched layer led to a resistance curve (R-curve) behavior in the Al-glass system they examined [57].

For testing involving thin films, a sandwiched system – the thin film of interest bonded between two elastic substrates of the same material – is often used. The effect of residual stress is minimized in such configuration because changes in film stress as the crack propagates are confined [58, 59]. Although there are three layers in the sandwich system, most investigators still use the results of Charalambides *et al.*, which are for a two-layered structure. The validity of this approximation was examined by Suo and Hutchinson [60]. The analytical results of a homogeneous two-layered structure was compared to that of a sandwiched one, with the thin film being a different material. The mode mixture at the crack tip was found to be similar. The difference in stress intensity factor could be accounted for by a scaling factor, p:

$$p = \sqrt{\frac{1-\alpha}{1-\beta^2}}\,, \tag{3.2}$$

where α and β are Dundurs' parameters [60]. For the Au-Si system studied in this work, p $\sim$ 0.9. Hence, to first order, results of a 2 layered structure are valid for

calculating the toughness of the specimens tested in this thesis.

3.2 Crack Path and Interfacial Toughness

In a ceramic-metal-ceramic sandwiched structure, the crack may propagate along the substrate-metal interface or within the metal. In an isotropic homogeneous brittle solid, defined as one in which the plastic zone is less than 1/25 of the layer thickness, the crack propagates along a path where $K_{II} = 0$ [61]. Under pure mode I loading, such a path exists at the middle of the bond layer. However, in sandwiched specimens, elastic mismatch and mode mixture (locally and in the far field) could veer that path away from the centerline and into the interface. The stability of the path was shown to depend not only on the elastic mismatch but the local T-stress, the stress that acts parallel to the crack plane, as well [61].

Evans and Dalgleish divided interfacial failure involving ductile bonding materials into two categories: ductile fracture or brittle debonding [59]. In ductile fracture, crack grows by void nucleation and both of the fractured surfaces show cup-and-cone features of classical ductile failure. In thin bonding layers, the toughness is linearly related to the bond layer thickness. In thicker films, however, the number of void nucleation sites becomes the governing factor. The voids were believed to originate at the triple grain junctions and the plastic energy dissipated in the material between the voids. Brittle debonding, on the other hand, was defined as failure that occurs strictly at the metal-substrate interface. Elastic fracture is typically lower. However, high toughness values were still found in some systems undergoing brittle debonding due to plastic dissipation in the adjacent metal [59].

In this work, the failure modes will be described by two terms: cohesive and adhesive failure. Cohesive failure refers to failure within the bulk of the bonded material, typically with features associated with ductile fracture. Adhesive failure describes failure at the thin film-substrate interface, which was determined by Auger spectroscopy to be at the Ti-SiO_2 interface.

3.3 Material Systems Examined Using Four-Point Bend

Four-point bend delamination has been used by many investigators to study the fracture behavior and materials toughness of sandwiched specimens. Examples of the material systems studied are listed in Table 3.1, ranging from composites [62, 63] to the common microelectronic thin film stacks sandwiched between Si substrates [58, 64, 65]. Crack propagation under constant load was observed experimentally by most investigators. In the microcasted stainless steel and copper specimens, unstable crack propagation was found, with a large load drop after every debonding [62]. The authors attributed this phenomenon to nonuniformity of the interface as a result of the microcasting process.

Many of the thin film specimens were formed by what the authors called diffusion bonding, or thermocompression bonding as defined in Section 1.1.4. The sapphire-gold-sapphire system studied by Reimanis was formed by inserting gold foil between sapphire substrates and heating the stack to 1040°C for 1 - 48 hours while under 5 MPa pressure [66, 67, 68]. Voids at the gold-sapphire interface were found to decrease with an increase in the bond time; although ~10 % void area still remained after 48 hrs. The toughness was found to range from 10-50 J/m^2, much lower than the expected fracture energy of ductile metals (typically around 10^4 J/m^2) due to adhesive failure [67]. In addition, the crack velocity was found to depend on the applied load, since sapphire is susceptible to humidity corrosion.

The Si-dielectric-metal system investigated by Dauskardt *et al.*, Lane *et al.* and Ma was formed by Cu-Cu [58, 64, 65] or Au-Au [64] diffusion bonding. Metal were deposited on stacks of thin film dielectrics and two such similarly processed wafers were bonded at 400°C for 4 hrs under 12 MPa of pressure. Adhesive failure were observed. The interfacial $\mathcal{G}_c$ ranged from 5 to 10 J/m^2 for metal layer thickness up to approximately 1 μm. An exponential increase in $\mathcal{G}_c$ was found when the Cu layer thickness was varied between 0.3 to 16.4 μm [65]. Interfacial failure, whether it be TiN-SiO_2 or TaN-SiO_2, were observed in the Cu-Cu system [58, 64, 65]. Ma noted

Table 3.1: Example of material systems reported in literature

material			thickness			
substrate	film	substrate	substrate [mm]	film [μm]	substrate [mm]	ref.
Al	epoxy	PMMA	total > 6 mm			[38]
steel	Cu	steel	6	1	6	[62]
-	NiAl	steel	–	1900	1.5	[62]
-	Ti	Ti alloy	–	500 - 2000	1.5 - 3	[63]
PMMA gl Al_2O_3	epoxy tp, s, Al gl	Al gl Al_2O_3	–	$\sim$ 25	–	[57]
Al_2O_3	Al	Al_2O_3	–	10, 25, 100	–	[66]
Al_2O_3	Au	Al_2O_3	0.5 - 1	10 - 250	2.5 - 4	[67]
Al_2O_3	Au	Al_2O_3	1	10, 25, 100	3.5	[68]
Si-SiO_2	Cu	SiO_2-Si	0.6	0.2	0.6	[58]
Si-SiO_2	Cu, Au	SiO_2-Si	0.6	0.2	0.6	[64]
Si-SiO_2-TaN	Cu	TaN-SiO_2-Si	0.76	0.03 - 16.4	0.76	[65]

gl = glass, s = steel, tp = thermoplastic

that failure occurred 20-40 nm in SiO_2 layer when Au-Au bonds were involved. It was attributed to change in the local mixture due to the difference in modulus between Cu and Au, where the mode I path exists in SiO_2 rather than at the interface between TiN and SiO_2.

3.4 Testing Procedure

This section describes the procedure used to test the specimens. The beam-like specimens were formed after the bonded wafers were diced. As mentioned in Chapter 2, each specimen was 8 mm wide, with a width-wise cut in the middle that was located above the KOH-etched trench in order to expose the bond interface. Mechanical tests were performed using an Intron mechanical testing machine in displacement-controlled mode at a rate of either 0.15 or 0.075 mm/min. The specimen rested on the outer rollers, which sat on a fixture that was rigidly attached to the upward moving crosshead. The inner rollers were attached to the stationary portion of the testing

machine via an adjustable grip. The adjustable grip improved the positional leveling of the top apparatus [69]. The alignment of the apparatus was checked immediately prior to testing with strain gauges located below the inner rollers. The distance from the outer to the inner roller was 1 cm while that between the inner rollers was 2 cm. A 100 N load cell was used to monitor the load. Load and cross-head displacement data were captured by a LabVIEW program while real-time observations of the specimen were made with a long working distance microscope. The video images were also recorded.

After the test was completed, the crack lengths on either side of the KOH-etched notch were noted. Two width-wise lines, just above the end of each of the cracks, were scribed on the surface of the DSP wafer using a diamond scribe. The specimen was then loaded in a three-point bend jig to promote crack growth from the scribed line to the bond interface, thereby detaching the delaminated segments from the still bonded portion of the specimen. Since minimal force was required for this procedure, any observable deformation reflected those sustained during the four-point bend delamination test. The fracture surfaces were examined using a scanning electron microscope (SEM) and optical microscopes.

3.5 Areal Correction in $\mathcal{G}_c$

Once the test is completed, the critical load associated with delamination can be used in Equation 1.2 to obtain the $\mathcal{G}_c$ of the bond. However, Equation 1.2 assumes the bond extends the full width of the specimen. In the specimen used in this work, only a fraction of the width is bonded. A correction for the actual bonding area is thus needed. When the gold lines were bonded in parallel, the correction factor is a simple ratio of specimen width to the total width of the gold layer. The equation thus becomes:

$$\mathcal{G}_c = \frac{1.5(1-\nu^2)}{E}\left(\frac{P_c\, l}{b}\right)^2\left(\frac{1}{h_1^3}-\frac{1}{(h_1+h_2)^3}\right)\left(\frac{w_{Si}}{w_{Au}}\right), \tag{3.3}$$

where w_{Si} and w_{Au} are the widths of the Si beam and the Au lines, respectively.

When the metal lines are bonded orthogonally, not only is the gold discontinuous along the width but along the length of the beam as well. The spacing between the 50 μm wide lines is 250 μm. Therefore, an additional factor of 6 would be included in Equation 3.3 for those calculations.

3.6 Determination of P_c

Ideally, the critical load, P_c, for delamination can be easily determined from the load-displacement curves such as the one shown in Figure 3-1 since the crack propagates under constant load in the constant moment region. This was found in elastic systems such as Si fusion bonds [40] as well as in systems involving ductile layers, such as Cu-Cu [58, 65]. The ideal load-displacement curve was found in some specimens in this work. However, there were many that exhibited non-ideal behaviors. In these instances, the P_c value in Equation 3.3 is the average of several loads.

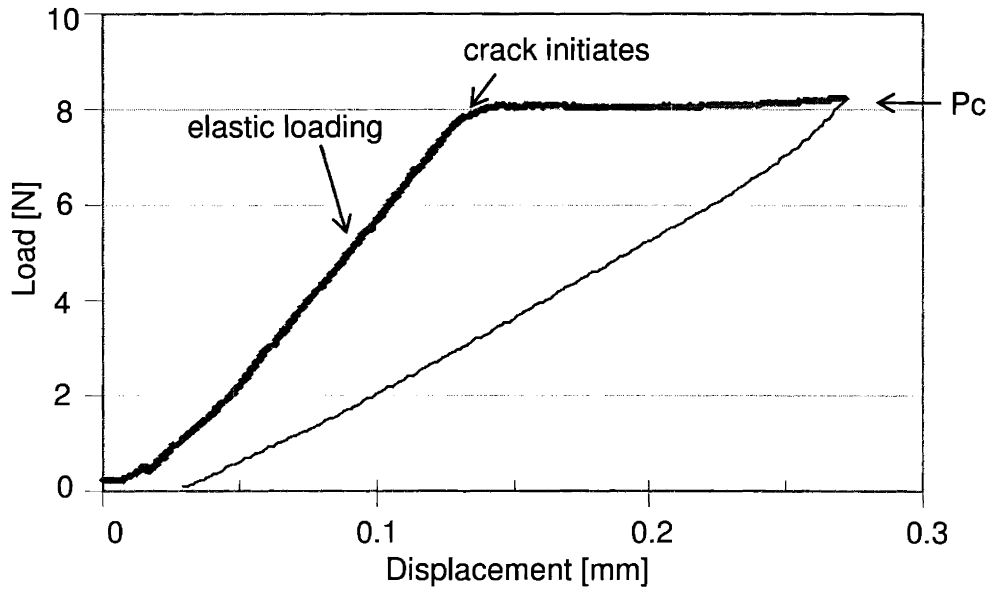

Figure 3-1: Ideally behaved experimental load-displacement curve, exhibiting a load plateau during crack propagation.

For instance, some specimens showed several constant load regions. The $\mathcal{G}_c$ for those specimens were calculated based on an average of the loads. Other specimens

exhibited a load peak followed by a load drop, upon which elastic loading resumed. In these specimens it was assumed that the crack propagated at the load peak. This was supported by the more compliant load-displacement curve as well as an increase in crack opening, which was often observable. The maximum load was thus used. A variant of such behavior is a peak load followed by a smaller but constant load. Since crack opening was observed to increase continually as the load remained constant, the crack was certainly propagating. This, as will be shown in Chapters 4 and 5, occurs due to local variations in toughness. The average of these loads was used in calculating $\mathcal{G}_c$. The longer the constant load region is, the less weight the peak load has using this method, and the resultant $\mathcal{G}_c$ may not even reflect the toughness at the peak load. This is a shortcoming, but given the indeterminant shape of the crack profile during testing, it would be impossible to match the loads with the areas that resulted. Load averaging provides an average toughness of the bonds in the area tested. As long as the load extraction method is consistent, comparison between process and property could still be determined using the average toughness as a metric.

Chapter 4

Bond Toughness Characterization

4.1 Factors That Influence Bond Quality

Bonding of surfaces occur when the distances between the two are so small that it becomes energetically favorable for the surfaces to coalesce in order to eliminate the interfacial energy. In thermocompression bonding, surfaces are brought together by the pressure applied during the bonding process. Due to surface roughness, bonds initially form where the surfaces touch at asperity contacts. As the materials deform under pressure, the asperity heights decrease, and more areas are brought into contact. At room temperature, in a material such as gold, relatively high pressures are needed for interatomic attraction to overcome surface asperities [70]. Metals tend to soften with increasing temperature due to increasing dislocation mobility and diffusion. Therefore, the pressure requirement can be offset by increasing the processing temperature. Hence, the required pressure depends on the mechanical properties of the material, such as yield stress, young's modulus, creep and diffusion characteristics. The elastic constants of crystalline gold are known to decrease with increasing temperature [71]. The creep and diffusion typically have an exponential dependence on temperature as well. It is thus expected that increasing temperature and applied pressure will facilitate the bonding process.

There are many parameters besides the mechanical behavior of the material that affect the bond: the flatness of the substrates, cleanliness of the surfaces, the deposi-

tion method, purity of the metal, just to name a few. Among the host of variables, this thesis focuses on parameters believed to have major impact on the bond quality, namely parameters that will bring surfaces into close proximity for bonding to occur. This chapter discusses the effects of bond pressure, temperature, time, and the bonding layer thickness on the measured bond toughness.

4.2 Thickness Effect

4.2.1 Experimental Procedure

In this set of experiments, the metal lines were bonded in parallel at 300°C for 10 min. The bonding layer thickness ranged from 0.26 to 1.2 μm. In addition to the layout with 50 μm lines, a mask with 7 lines, each 6mm wide, was used. The pressure was nominally 7 MPa for the 50μm wide lines and 1.25 MPa for the 6mm wide lines. After testing, failure modes of the specimens were examined. Misalignment was measured in the SEM at 1000x magnification and the actual bonded area was used in the toughness calculation.

4.2.2 Results

For a crack to propagate in a material, energy is needed to overcome the bonding between the constituent atoms or molecules to create additional surface area. In elastic systems, nearly all of the energy input is used in that process. In systems with ductile materials, however, energy can be dissipated in the surrounding materials in the form of plastic deformation. More strain energy is thus required when crack propagation involves plasticity. Confinement of the thinner layers prevents plastic dissipation as well. Generally speaking, Figure 4-1 agrees with the findings of Cu-Cu and Al-Cu systems [58, 65], with an observed trend of increasing $\mathcal{G}_c$ with bond layer thickness in both geometries. Thin specimens with adhesive failure were found to have $\mathcal{G}_c$ in the 10-20 J/m^2 range. For specimens with a bonding layer greater than or equal to 0.52 μm, $\mathcal{G}_c$ ranges from 37-67 J/m^2. In the Cu-Cu thin film system, such

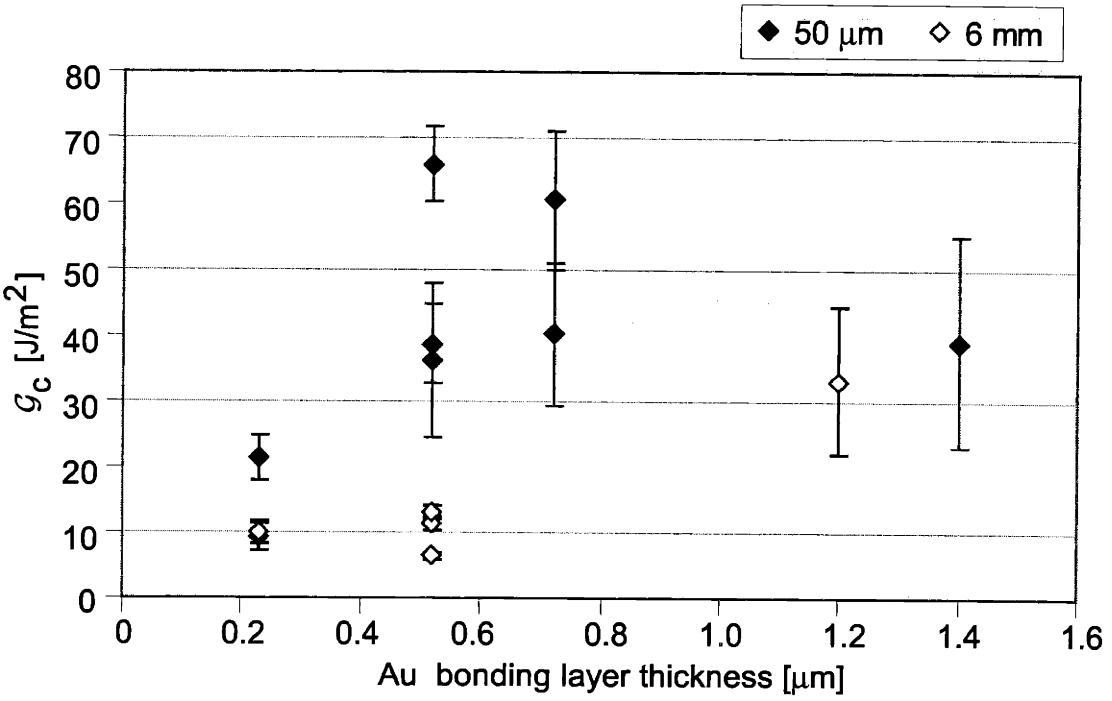

Figure 4-1: $\mathcal{G}_c$ as a function of Au bond layer thickness for the two geometries tested: 50μm (7 MPa) and 6 mm (1.25 MPa) lines. Each point represent 4-7 measurements from one wafer. The error bar indicates 1 standard deviation.

high $\mathcal{G}_c$ values corresponded to Cu thicknesses greater than 6 μm [65]. The debonding interface in that work is in the elastic adhesive layers. Moreover, the yield strength of Au is less than that for Cu; thus, more plastic dissipation is expected from Au. However, the exact relationship between $\mathcal{G}_c$ and bond layer thickness was not clear in the narrow range of thicknesses studied.

The failure mode in the thinner specimens was predominantly adhesive failure. The measured values of $\mathcal{G}_c$ were also more uniform within specimens, and between specimens, when compared to specimens with thicker bonding layer, as shown in Figure 4-1. As energy was dissipated via plastic deformation, more scatter in the toughness was found. Part of the scatter was due to nonuniformity in the bonding. An example of such a bond is shown in Figure 4-2. Plastic deformation was evident in the top two lines of Figure 4-2(b), indicating good bonding. In contrast, relatively little deformation occurred elsewhere; it is difficult to judge from Figure 4-2(a) how much of those areas were actually bonded. Few adhesive failures could be seen in the

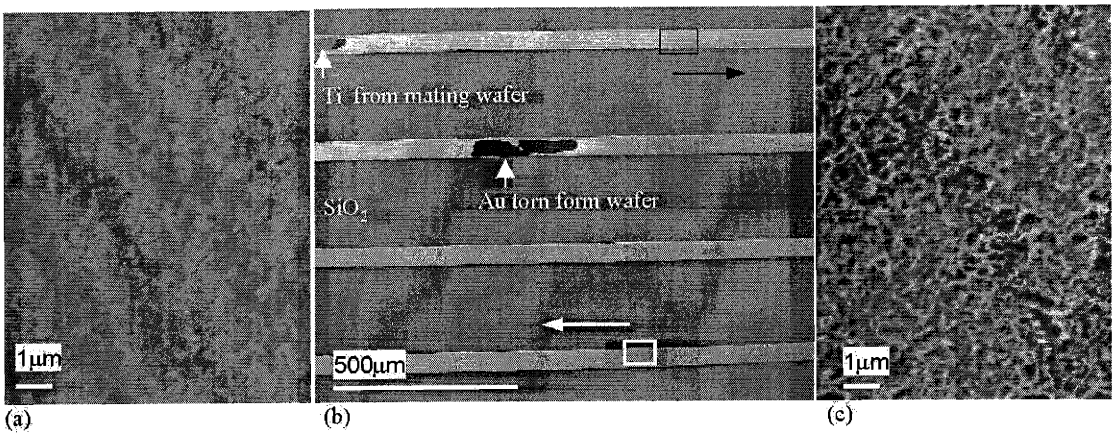

Figure 4-2: SEM images of the fractured surfaces of a delaminated specimen with a 0.72 μm bonding layer. (a) Area with low plastic deformation. (b) Areal image of 4 line showing variation in plastic deformation. Bright areas correspond to high plasticity. Adhesive failure is also observed. (c) Area with more plasticity.

micrograph, as is the case for specimens with bonding layer thickness greater than or equal to 0.72 μm for both linewidths. Although, as Figure 4-2(a) shows, some "cohesive" failures were result of poor bonding.

4.3 Repeatability

4.3.1 Experimental Procedure

The repeatability of the process and toughness measurement was studied with specimens bonded at 300°C with a pressure of 73 MPa for 10 minutes. Fabrication of the specimens followed the general process flow described in Chapter 2. The metals, around 0.5 μm thick on each wafer, were deposited in three different e-beam runs. Two pairs of wafers (8G and 8H) were bonded using EV AB1-PV while the other 5 pairs used EV501 bonder[1]. Specimens were tested, in random order, as described in Chapter 3, with a displacement rate of 0.075 mm/min.

[1]AB1-PV is dedicated to 4" processing while EV501 is a newer tool, capable of handling both 4" and 6" wafers. Although the fixtures and chucks are different for the two equipments, their designs are basically the same.

4.3.2 Results

The mask was designed with ~2 mm wide dicing alleys, as described in Chapter 2. When the lines are bonded orthogonally, the dicing alleys and the KOH etched trench partition the specimen into four sections, as illustrated in Figure 4-3. The unbonded region between sections is wide enough that an increase in crack opening and an associated load drop could be observed during testing. Hence, a single specimen may be sub-divided into quarters, allowing four toughness values to be obtained from one test specimen. In order to show the distribution of the toughness values obtained, all the N data points per bonding condition were ranked in ascending order, with n={1,..,N}.

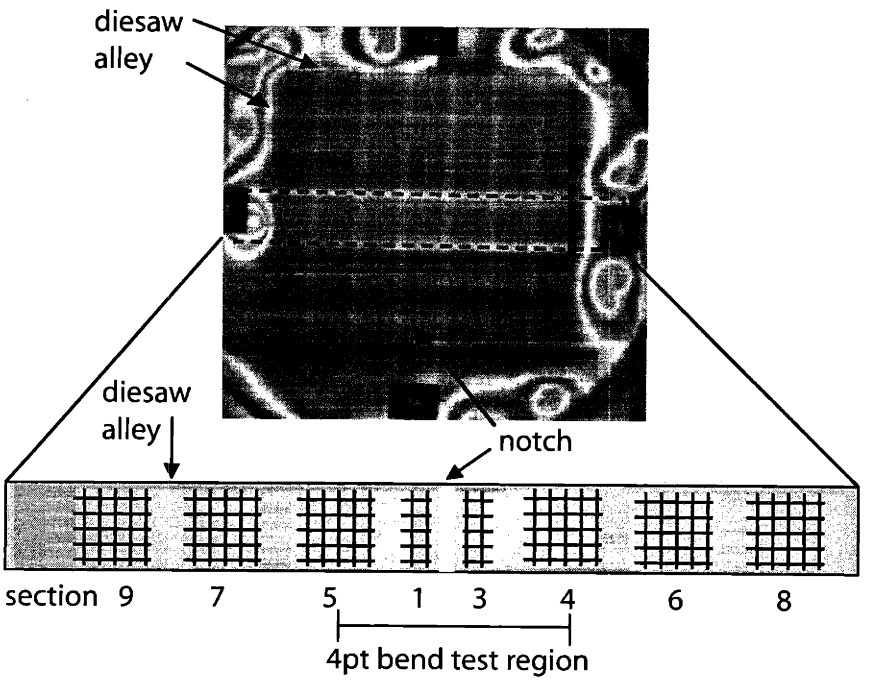

Figure 4-3: IR image of a wafer pair with lines bonded orthogonally. Each specimen has 2 sections on either side of the notch in the area that would be in the constant moment region when loaded in four-point bend testing.

There is no strong indication of tool dependence in the data shown in Figure 4-4. There is, however, significant variation from wafer to wafer as well as within the same wafer. Failure was observed to occur predominantly within the gold layer. For specimens with $\mathcal{G}_c < 100$ J/m^2, large areas of poor, or possibly non-bonding, pads

were found. As $\mathcal{G}_c$ increases, so do the number of bonded pads and the degree of plastic deformation. At $\mathcal{G}_c \sim 300$ J/m^2, nearly all of the pads were found to be bonded and plastic deformation was easily identified under an optical microscope.

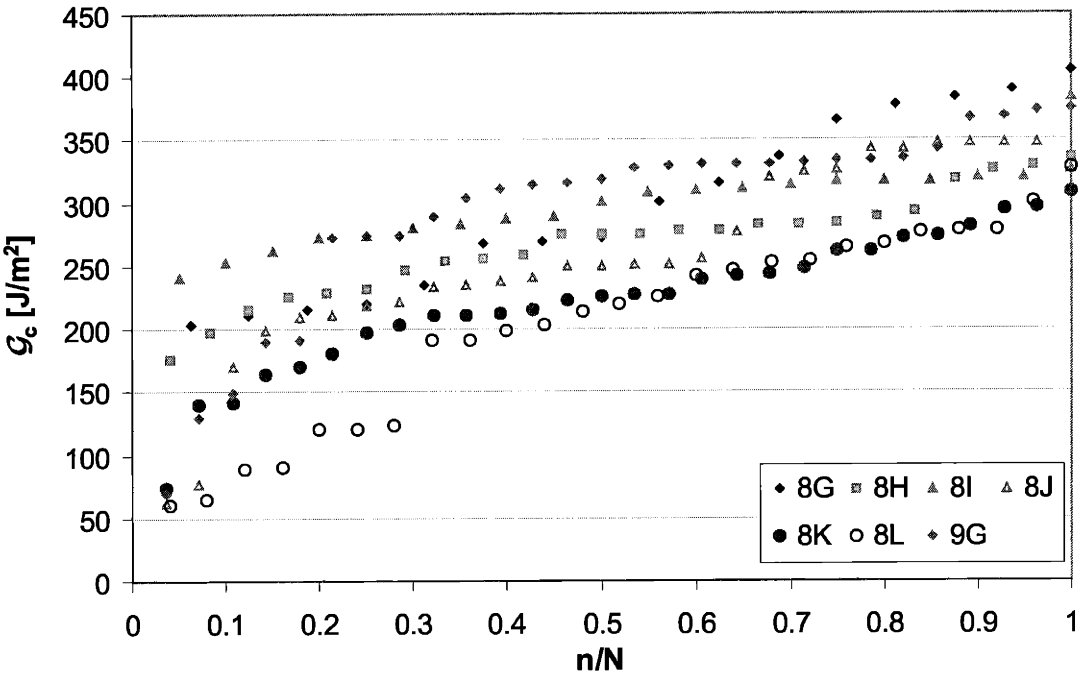

Figure 4-4: $\mathcal{G}_c$ as a function of n/N for 7 wafers bonded at 300°C and 73 MPa for 10 min.

Small variations in the bonding process are listed in Table 4.1. The bonder temperature at the start of the bonding process may influence the microstructure, since gold may undergo some grain growth as the temperature ramps up to the bonding temperature. However, given a ramp rate of 18°C/min, the variation in grain growth would not be significant. The data also do not support strong correlation with other variations such as the chamber pressure or removal temperature[2].

When all the data points are plotted together in Figure 4-5, the majority of the $\mathcal{G}_c$ values fall between 200 - 350 J/m^2. Despite the large scatter in $\mathcal{G}_c$ per wafer, the amount of scatter is about the same for any given wafer. Therefore, data from 1 or 2

[2]The temperature at which the bond chuck was removed from the bonder; the wafer stack remained on the stainless steel chuck to cool; i.e. cool enough to touch the stainless steel diffuser plate.

Table 4.1: Fabrication details of specimens bonded at 300°C and 73 MPa

Bonder	Wafer ID	e-beam run	P_{Bonder} [mbar]	Bonder Temp [°C]	
				Start	Removal
AB1-PV	8G	a	7	20	80
	8H	a	5	51	25
EV501	8I	b	1 E-3	60	280
	8J	b	12	20	134
	8K	b	7 E-4	54	168
	8L	b	5 E-4	84	177
	9G	2	9	100	115

wafers adequately capture the toughness trend for a given processing condition.

4.4 Pressure and Temperature

4.4.1 Experimental Procedure

To examine the effects of pressure and temperature, the bonding layer thickness was held constant around 1 μm. Specimen fabrication follows the general process flow described in Chapter 2, with the bonding temperature and pressure on the gold varied as shown in Table 4.2. The metals were deposited in three different e-beam runs. Specimens were tested as described in Chapter 3, with a displacement rate of 0.075 mm/min.

Table 4.2: Bond temperature and applied pressure (on gold)

Temp [°C]	P_{Au} [MPa]	Wafer ID	e-beam run
260	30	9B & 9E	1 & 2
	73	9C & 9H	1 & 3
	120	9J & 9L	1 & 3
300	30	9D & 9F	2 & 3
	73	9G	2
	120	9I & 9K	3 & 2

In addition to bond toughness, the percentage of bonded pads was also noted by examining the fractured surfaces. The fractured surface of pads that were bonded

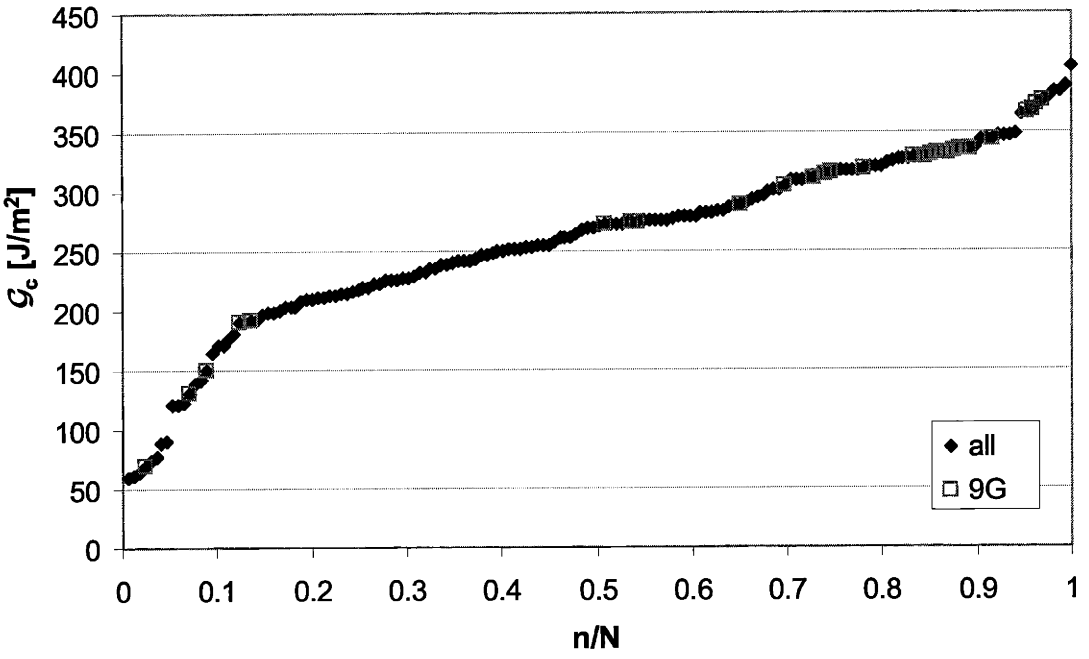

Figure 4-5: $\mathcal{G}_c$ as a function of n/N for all of specimens bonded at 300°C and 73 MPa for 10 min. 9G specimens are shown to demonstrate that specimens from 1 wafer capture the trend in $\mathcal{G}_c$, despite the large scatter in the result.

were rougher than the gold on either side of it, which was not bonded. The roughness is a result of plastic deformation, which is visible under an optical microscope. Highly deformed pads appear dark. Hence, this visual contrast can be used to assess whether a pad has been bonded or not. Digital images of the fractured surfaces of the two sections immediately on either sides of the notch were taken. A MATLAB program was then used to process the images and count the percentage of pads that were successfully bonded. A pad was considered bonded if $\leq 10\%$ of the pixels in the pad were of the same greyscale or lighter[3] than the surrounding gold.

4.4.2 Results

Similar to results in Section 4.3, Figures 4-6 and 4-7 show that the toughness spans a wide range. There were four known deviations from the standard process. One

[3]Undeformed/unbonded Au is more reflective and appears brighter under optical microscope.

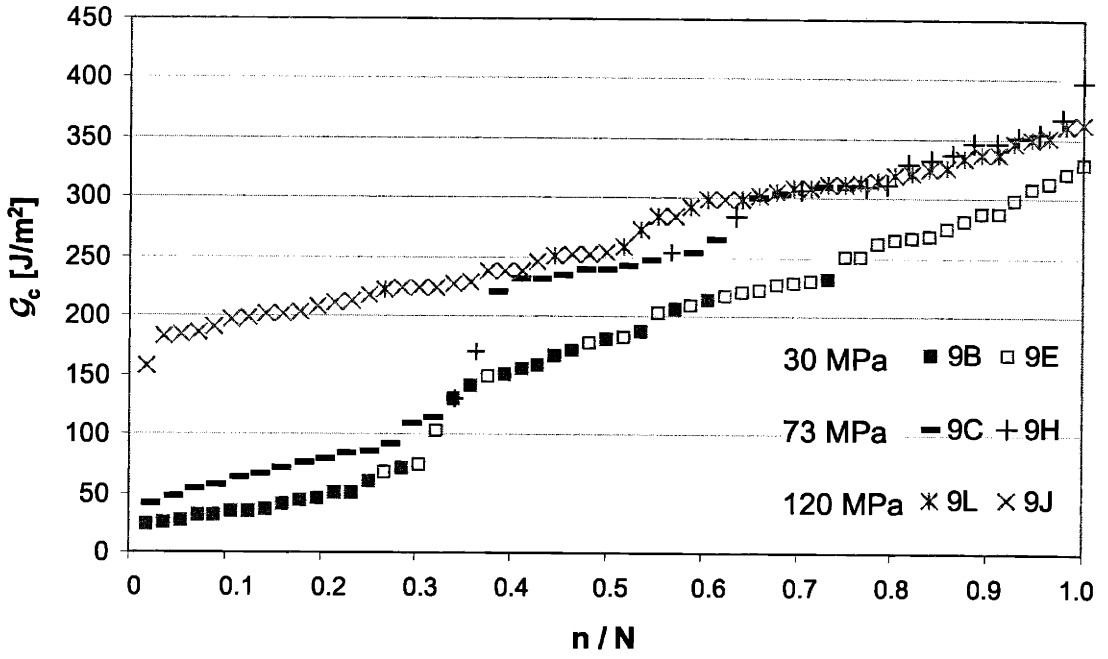

Figure 4-6: $\mathcal{G}_c$ as a function of n/N of all specimens bonded at 260°C.

was the delay time between the end of the UV-ozone clean and wafer alignment, as listed in Table 4.3. UV-ozone is used to reduce the organic contaminants. Jellison found no difference in the specimens treated with or without UV-ozone (for 16-20 hrs) when the bonding temperature was 350°C. Heat served to break up the organics; the carbon layer was found to be reduced from 20 to 2 Å when the substrate was heated to 300°C. [29]. Thus the effect of the delay is expected to be minor given that the wafers were heated prior to bonding. Another deviation was the absence of one of the separation flags between the wafers prior to bonding. The flexible flags could become bent with use. When that happens, the wafers were unable to sandwich it between them in the alignment process. Also, 9I was exposed to the UV environment twice – the wafers were not bonded after the first clean due to pressure gauge failure of the bonder. Finally, the pump, normally turned off after the nitrogen purge cycles, remained on during the bonding of 9J. While the effects of these anomalies cannot be entirely discounted, they do not appear to be the source of variation in the measured toughness.

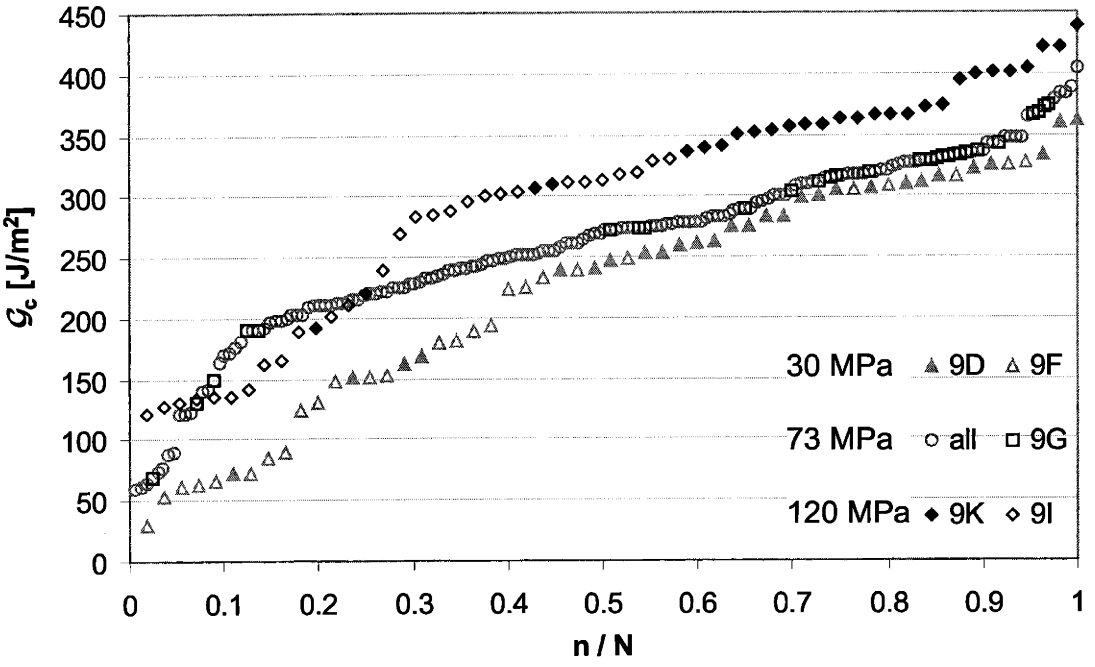

Figure 4-7: $\mathcal{G}_c$ as a function of n/N for all of specimens bonded at 300°C.

Table 4.3: Fabrication details of specimens bonded with varying temperature and pressure

Wafer ID	e-beam run	$P_{chamber}$ [mbar]	Bonder Temp [°C]		Delay bt UV & bond	Flag Not inserted
			Start	Removal		
9B	1	10	84	84		
9E	2	6	84	110		
9D	2	9	38	120	30min	X
9F	3	10	79	102		
9C	1	9	69	126		
9H	3	9	87	92		
9G	2	9	100	115	15min	
9J	1	4E-4	75	102		X
9L	3	8	25	95		
9I	3	14	25	92		
9K	2	10	65	75		

Table 4.4: E-beam chamber pressure prior to Ti deposition and during Au deposition

e-beam run	P_{base} [torr]	P_{base} during Au dep[torr]
a	8E-7	1E-6
b	2E-6	2E-6
1	1E-6	1E-6 to 7E-7
2	7E-7	2E-7
3	4.5E-7	1E-6

Figures 4-6 and 4-7 indicate variation between wafers bonded under same nominal conditions; one wafer typically had higher toughness than the other. In particular, wafers with higher toughness in several pairs – 9E, 9G and 9K – came from e-beam Run 2, which had the lowest background pressure during Au deposition. Typically, lower background pressure results in the incorporation of fewer impurities. This may yield larger grained films, which would have a lower yield stress. The grain size of the as-deposited films from these deposition runs was not known. But, the grain size of films deposited at 5 E-6 torr was measured to be around 60 nm, which, as stated in Section 2.6.1, is comparable to those reported in the literature. Moreover, an order of magnitude change in background pressure may not alter the grain size significantly; the grain size of Au deposited at 2 E-8 torr was reported to be around 50 nm [72]. Significantly large grain films could be obtained if they were deposited under UHV conditions [47]. Therefore, the apparent higher toughness is not a result of the deposition pressure. Just for comparison, AFM measurements of Au in the areas which were not meant to be bonded were taken after a few of the specimens were tested. Indeed, similar surface roughness values were obtained for 9H, 9C, 9F, 9D: 2.13 nm, 1.65 nm, 1.9 nm and 1.79 nm, respectively. In addition, the AFM images did not reveal significant differences amongst these specimens.

For wafers bonded at 260°C and 30 MPa, although low toughness specimens had few cohesive failures and some adhesive failures, the majority were poorly bonded, often the only indication of bonding was near the edges of pads, as shown in Figure 4-8. Little energy is thus required to delaminate the specimens. As the toughness increased, an increasing number of pads were found to exhibit either of the fail-

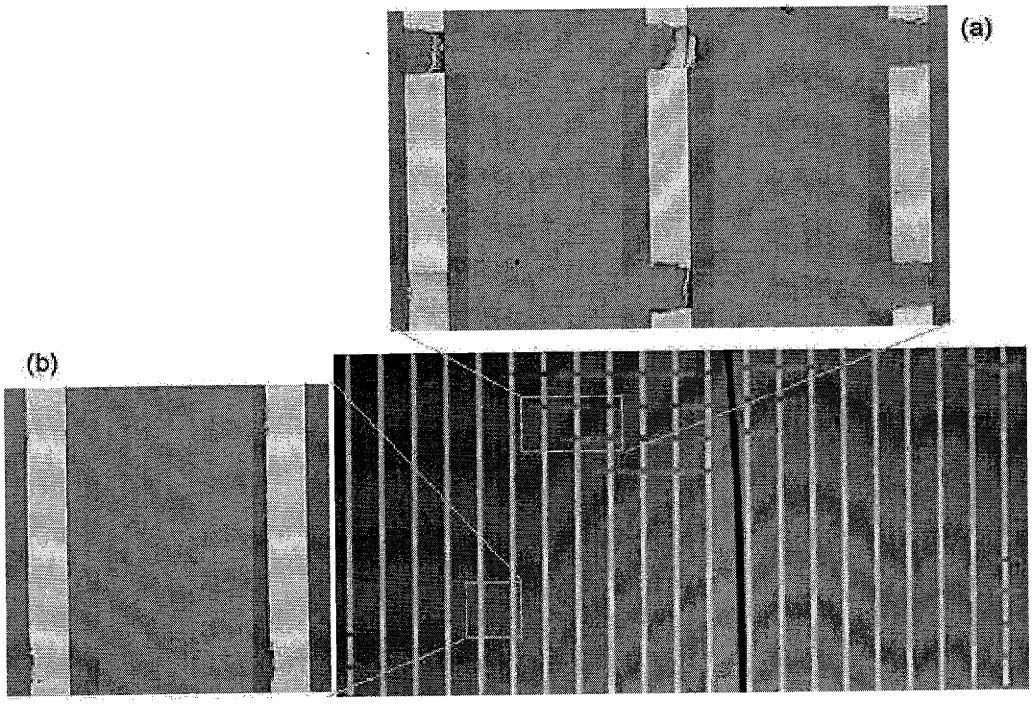

Figure 4-8: Fractured surface of poorly bonded pads. (a) Region with adhesive failure. (b) Signs of deformation visible only at the edges of the lines.

ure modes, indicating an improvement in the bond quality. Since more energy is dissipated in ductile deformation, higher toughness values were obtained from specimens with more cohesively failed pads. At the high end of the toughness range ($\geq$ 200 J/m^2), most failures were cohesive with deformation that was clearly visible under an optical microscope.

Toughness is expected to increase when the bonding temperature and pressure are raised. However, Figures 4-6 and 4-7 show that even those wafers bonded under high pressure had some specimens exhibiting low toughness. Similar to 9B and 9E specimens, a couple of specimens had large areas of poor or no bonding in the low toughness range, $\mathcal{G}_c \leq 60$ J/m^2. In the mid-to-lower toughness range, $60 < \mathcal{G}_c \leq 250$ J/m^2, many of the pads were bonded. In fact, under the highest applied pressure, bonding is nearly 100%. The relatively low toughness stemmed from the adhesive failure mode. As mentioned in Section 4.2, less energy is dissipated in adhesive failure due to the lack of plasticity. In principle, adhesive failure should produce a fairly constant toughness, given it is an elastic energy release. But, experimental

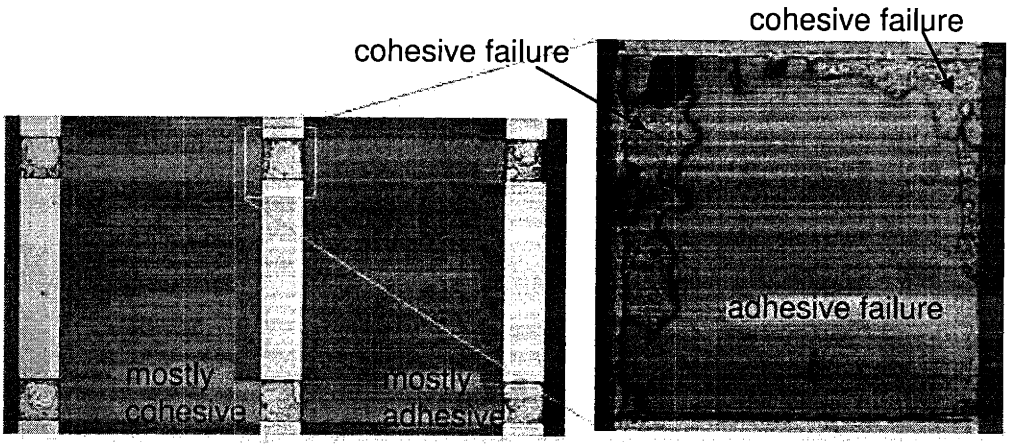

Figure 4-9: Fractured surface of pads showing both fracture modes. Zoom in view shows a pad with mostly adhesive failure but plastic deformation is also visible.

data on Cu bonds showed that the ductility of neighboring films allowed additional energy to be dissipated, even when failure mode was adhesive [65]. Hence, there was variation in the toughness measured, depending on the ratio of adhesive to cohesive failed bonds in a given specimen and the amount of energy dissipated in the process. Adhesive failures with varying degrees of plasticity were observed. Some were obvious, while others could be inferred, as shown in Figure 4-9. As the failure mode shifts toward being predominantly cohesive, the toughness increased.

For a fixed bonding temperature, the range of toughness generally increases with pressure. Likewise, for a given pressure, the toughness increases with temperature. As greater deformation may be obtained with either an increase in pressure or decrease in modulus of the material (due to increase in temperature), the data support the expectation that increased toughness results when the bonding temperature and pressure are raised. Improved bond quality is evident in toughness values and yield. Results for the percentage of pads that were bonded, shown in Figure 4-10, compliment the toughness result. At the highest pressure, nearly 100% of the pads were bonded. The toughness values for these specimens were also high, indicating these are well bonded pads. 9B shows large areas that are not bonded, corresponding to the generally lower toughness values. With the exception of specimens bonded at 300°C and 120MPa (9K and 9I), which exhibited $\mathcal{G}_c > 400$ J/m^2 at the high end, most of the

specimens from several bonding conditions merge and peak around around 350 J/m^2. All showed high plasticity such as that in Figure 4-11. The rms surface roughness of these highly deformed pads was measured using AFM to be 82 nm. The peak to valley distance was 475 nm, indicating that most of the layer had undergone plastic deformation. The data suggest 300-375 J/m^2 as the upper bound of toughness that may be expected when bonding under the conditions studied.

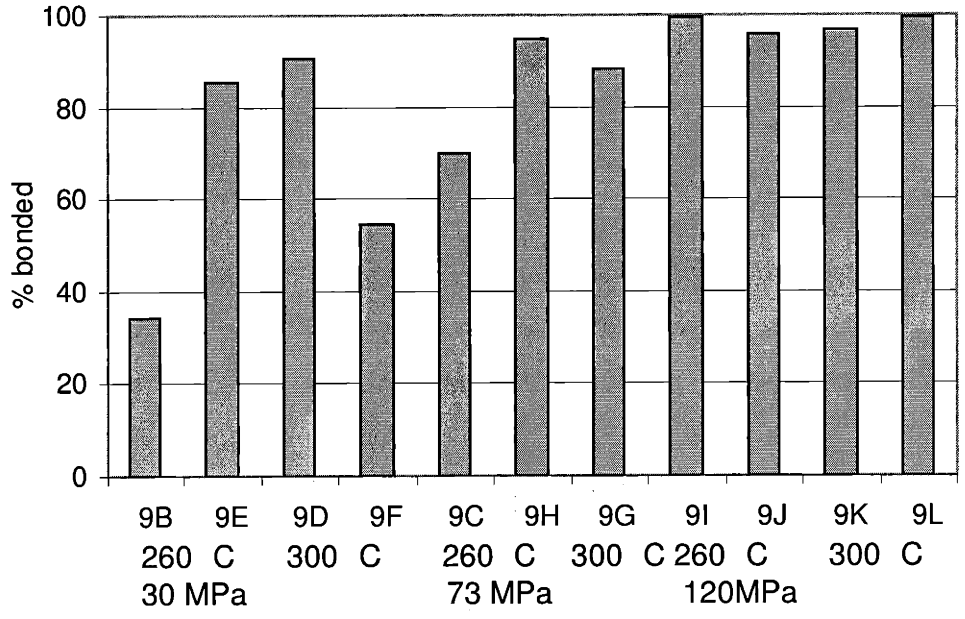

Figure 4-10: Bond quality of specimens bonded under various conditions.

4.5 Bond Time

4.5.1 Experimental Procedure

To explore the effect of bond time, the bonding layer thickness was again held constant at approximately 1 μm. The metals were deposited in two separate runs: DSP wafers in one and the regular wafers in the other. Three pairs of wafers were bonded at 300°C with an applied pressure of 30 MPa. The bond times were 2, 40 and 90 min. An additional pair was fabricated by holding substrates at 300°C for 48 min and then the pressure was applied for 10 min.

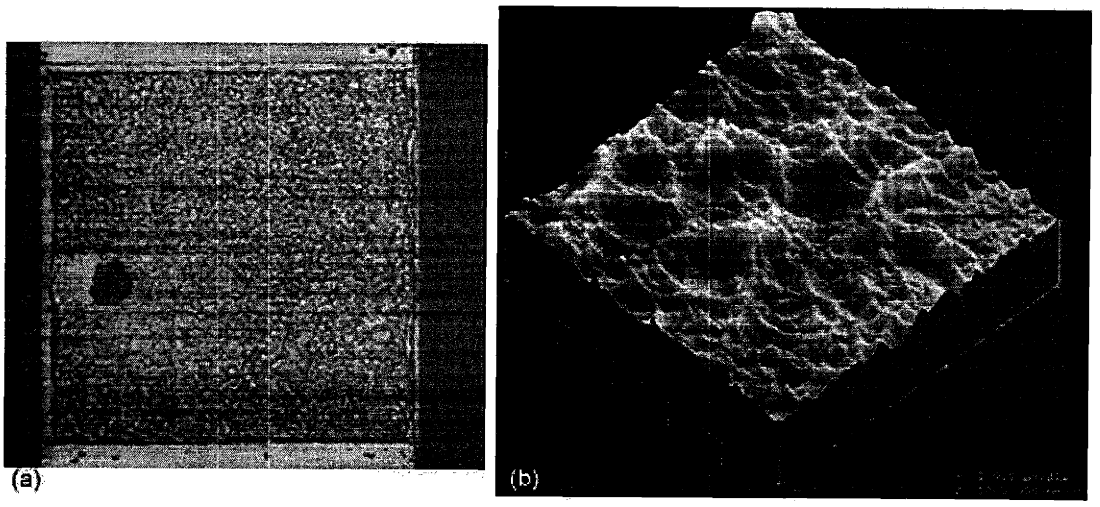

Figure 4-11: Fractured surface of pad showing high plastic deformation. (a) Optical micrograph. (b) AFM image of a 5 x 5 μm^2 area, with rms of 82 nm.

4.5.2 Results

Figure 4-12 shows the results of specimens bonded for 2, 40 and 90 min together with the results of 9D and 9F from Section 4.4, which were bonded for 10 min. While scatter in the data remains, $\mathcal{G}_c$ ranges are comparable, whether the specimen was bonded for 2 or 90 mins. The $\mathcal{G}_c$ values of 10B (40 min bond time), on the other hand, are generally much lower than those of other two wafers. The failure mode in these wafers was mostly cohesive failure. The fractured surface of 10B had areas which showed no difference between the pad and the surrounding Au, indicating poor or no bonding. In contrast, few pads from 10A and 10C specimens were found not to have bonded. The bond time does not seem to affect the toughness or the bond quality. Recall that from the results of the curvature measurement in Section 2.6.2, the film stress was around 30 MPa and fairly constant above 200°C (Figure 2-10). The applied pressure thus brings surfaces together, with help from the relatively fast surface diffusion. But if there are gaps between bonded surfaces, more pressure would be required to bring the surfaces closer. In solid-state joining, the time-scale for which improvement may be seen is usually very large compared to the typical (and practical) bonding times [73]. As thermocompression is a class of solid-state joining, it is not surprising that results show bond time having limited effect on the bond quality or

toughness.

Regarding the wafer with the 48 min anneal, although test structures were successfully diced from the wafer, the bond interfaces looked as if debonding had occurred. Of the four specimens tested, all had observable crack opening at 1-2 N loads. The cause of poor bonding is not clear, and would require more specimens to be fabricated in future studies.

4.6 Discussion and Conclusion

This chapter presented experimental results and discussed the effects of several bonding parameters. Energy dissipation is confined when the bonding layer thickness is thin, resulting in low $\mathcal{G}_c$ values, on the order of tens of J/m^2 for lines bonded at 1.25 and 7 MPa. The failure mode was observed to be mostly adhesive, and there was a measurable difference in $\mathcal{G}_c$ for the two pressures for thickness less than or equal to 0.52 μm. As the bond layer thickness increases, cohesive failures were observed, and more scatter in the data were found. Data (Figure 4-1) suggest but do not perfectly match the expectation of increase in $\mathcal{G}_c$ with increasing bond layer thickness.

It was also expected that higher deformation of the gold would lead to improved bonding. Indeed, the overall trend of the data showed increased toughness with increasing bonding temperature or pressure. Thickness effects aside, $\mathcal{G}_c$ of specimens bonded under 7 MPa of pressure were much lower compared to those at 30, 73 or 120 MPa: tens vs. hundreds of J/m^2. The increase in toughness manifested itself in the form of plasticity. For specimens bonded with pressure less than or equal to 7 MPa, plastic deformation was only visible under the SEM. For specimens bonded at greater than 30 MPa, much of the deformation was visible using an optical microscope under low magnification. The surface roughness of an as-deposited film was around 3 nm. That value dramatically increased to 37 nm or even 80 nm for $\mathcal{G}_c$ of 100-150 and 300 J/m^2, respectively. At the high end of the $\mathcal{G}_c$ measured, the peak-to-valley height could be as much as 475 nm, which was about half of the bond layer thickness.

The exact effects of temperature or pressure on $\mathcal{G}_c$ are difficult to define given

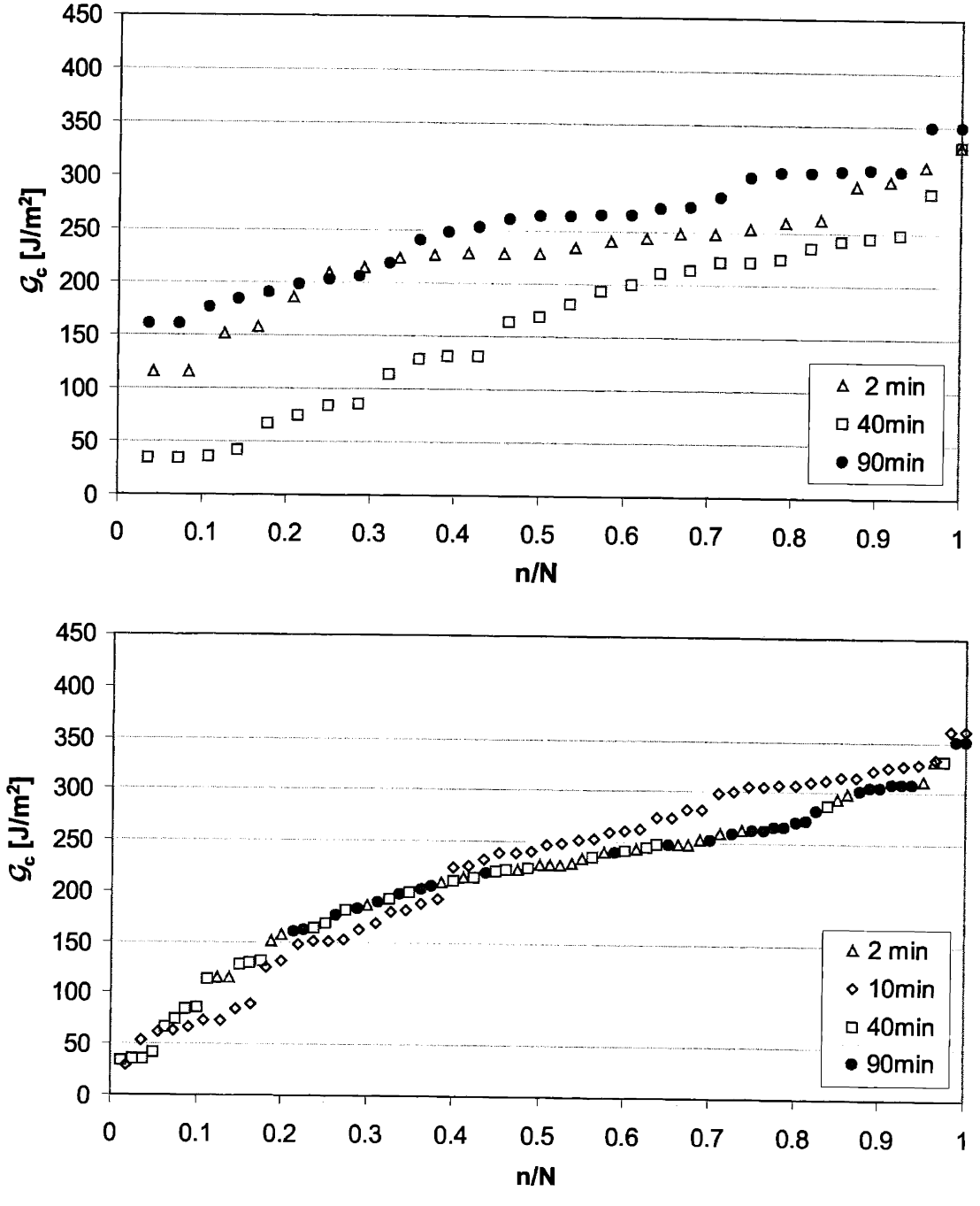

Figure 4-12: $\mathcal{G}_c$ as a function of n/N. Bond times are 2, 10, 10, 40 and 90 min for 10A, 9D, 9F, 10B, and 10C, respectively.

the large scatter observed. The scatter does not appear to be related to process variations such as initial temperature of the bonder, background pressure during the gold deposition, delays between UV-ozone clean and alignment. However, the range of scatter shown per wafer is fairly representative of the scatter that could be expected for the given bonding condition, as results from Section 4.3 showed. Ductile fracture can involve much more energy than that required to break the bonds at the interface due to the ability to dissipate energy by plastic deformation. There are several mechanisms by which plastic energy is dissipated: directly as in visible ductile fracture within bulk gold, indirectly in the gold even though the eventual fracture occurs adhesively, or in combination. In many of the systems studied by other investigators, interfacial (adhesive) failures were found. But both adhesive and cohesive failures were observed in the specimens tested in the present work. The prediction of the crack path is rather complicated and was not pursued in this work. Only experimental observations were noted. It was found that when a lower value of $\mathcal{G}_c$ was measured, the specimens tended to fail adhesively while higher $\mathcal{G}_c$ corresponded to cohesive failures.

Bond time variation, between 2 to 90 min, was shown not to affect the resultant $\mathcal{G}_c$. High numbers of bonding pads were found in specimens bonded for 2 min (10A), despite the short bonding time. The fractured surfaces of specimens bonded with 2, 40 or 90 min consistently showed low plastic deformation. However, they had $\mathcal{G}_c$ values comparable to the 10 min specimens (9D and 9F). The latter had more inconsistency in deformation morphology, but more visible deformation. The strain energy release rate measures the macro scale phenomenon based on beam bending. It will not capture the exact, subtle changes at the crack tip; thus the fractured surfaces of these specimens may appear different even when the $\mathcal{G}_c$s are comparable.

Chapter 5

Finite Element Modeling

Given the non-ideal behaviors observed during testing and the large scatter in the resultant $\mathcal{G}_c$ that could not be satisfactorily explained by process variations, it was hoped that finite element modelling would further the understanding on both issues. Asymmetric delamination of the specimens was studied by evaluating the strain energy release rate, $\mathcal{G}$, at the crack tip. A cohesive zone model was used to describe the fracture process in order to compare the load-displacement curves with experimental data. Finally, modeling of the bonding process is discussed.

5.1 Asymmetric Delamination

The axisymmetric configuration of the four-point bend specimen lends itself to the ideal assumption that cracks propagate equally on either side of the notch. Whether this is realized experimentally is almost never reported in literature. It is likely that one side delaminates slightly before the other, as observed by Turner in the case of Si-Si fusion bonded specimens [74]. But the difference is sufficiently small that the ideal assumption holds. Among the numerous reports listed in the Bibliography, only Ma mentioned that asymmetric crack propagation was observed and that one of the sides dominates the propagation at a given time [64]. However, neither the time difference nor the crack length was stated.

For the test setup used in this work, the inner rollers were spaced 2 cm apart,

therefore allowing steady state propagation of approximately 8 mm on either side of the notch. Symmetric delamination was infrequently observed. Typically, one side would delaminate first and the crack would grow several mm before the other side began to propagate. Subsequent propagation could become even on both sides or remain asymmetric. Theoretically, as long as the crack remains between the inner rollers, the constant moment condition would be maintained, and Equation 3.3 remains valid. However, in some tests, one of the cracks would run 6-7 mm before the other side delaminated. Therefore, there was a question as to whether the stress intensity at the second crack tip would be modified due to the first crack reaching the inner roller.

5.1.1 Modeling Environment

To confirm the validity of using Equation 3.3 for asymmetrically delaminated specimens, the stress intensity factor and strain energy at both crack tips were found numerically using FRANC2D/L [75]. FRANC2D/L (FRacture ANalysis Code 2-Dimensional) is a finite element based simulator that was developed for solving 2-D fracture problems. After a crack is placed in a structure, remeshing of the structure is done automatically.

Two structures were simulated. Figure 5-1 shows the ideal mesh, in which only half of the beam was modeled. The non-ideal case was simulated with a full beam in order to delaminate the beam asymmetrically. The thickness of the upper and lower beams were 525 μm and 450 μm, respectively, and the full width of the notch area was modeled as 1.2 mm. For simplification, the beams were considered as homogenous Si, without Au at the interface. The Young's modulus, Poisson's ratio, and density values used in the model were 165 GPa, 0.25, and 2.33 g/cm^3, respectively.

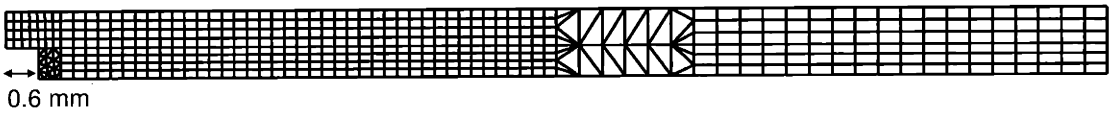

Figure 5-1: Mesh of the ideal four-point bend model used in FRANC.

The initial crack was placed in the interface at the edge of the notch. For propagation, a crack length was chosen and the structure was remeshed and system analyzed. The stress intensity factor, K, and strain energy, $\mathcal{G}$, of both fracture modes were calculated using the J-integral method. In the asymmetric propagation simulation, the growth initially occurred on the right side, to a distance of 3.8 mm. Then the left side was delaminated. K and $\mathcal{G}$ were calculated at regular intervals until the crack length, a_{left}, reached 8.89 mm. At that point, the crack on the left was arrested and the final growth occurred on the right, from a_{right} of 3.8 to 6.35 mm. A constant load of 8 N was applied for all cases.

5.1.2 Simulation Results

The total strain energy, $\mathcal{G}_{tot}$, was obtained by summing the strain energy in both modes. Figure 5-2 shows $\mathcal{G}_{tot}$ as a function of the crack length. A positive crack length indicates growth on the right side while a negative length refers to growth on the left side. No substantial difference between the ideal and the asymmetric case was found. The $\mathcal{G}_{tot}$ stays relatively constant through a crack length of 8.89 mm. Note '$*$' represents the $\mathcal{G}_{tot}$ at the right crack tip. It is plotted in the negative crack length as well to show that its value was not affected by the crack growth on the left side, which grew from the left notch to a distance of -9.9 mm. Therefore, Equation 3.3 is applicable even when the specimens delaminate asymmetrically.

5.2 Non-ideal Load-Displacement

As mentioned in Section 3.6, specimens did not always delaminate under constant load conditions. In some specimens, multiple load plateaux, not necessarily of the same value, were obtained. In others, a load peak was quickly followed by a load drop, corresponding to a sudden increase in crack opening, which suggests rapid crack propagation and eventual arrest. For a given bonding condition, results presented in Chapter 4 showed that there is scatter in the data. The fractured surfaces in some specimens also indicated variation in bond quality and uniformity. Equation 1.2

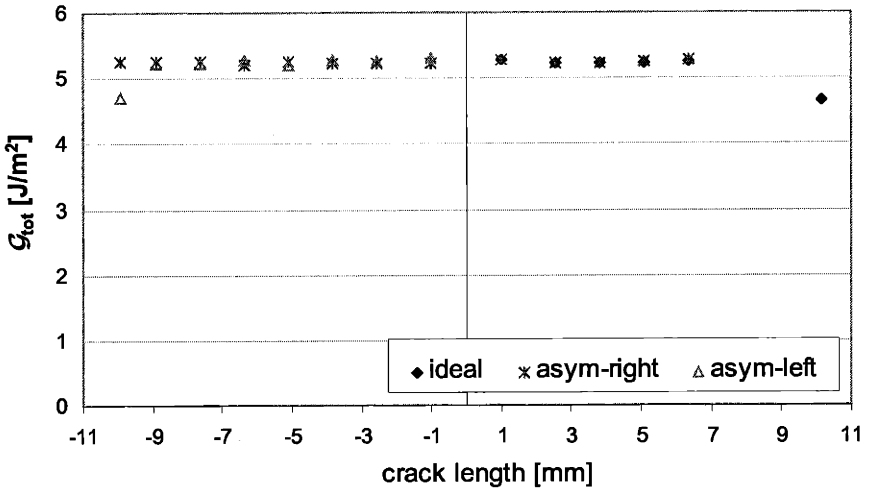

Figure 5-2: $\mathcal{G}_{tot}$ as a function of crack length for symmetric and asymmetric crack propagation.

assumes a continuously bonded specimen with constant toughness. The effects of varying toughness and discontinuous bond geometries were not considered. This section describes the modeling work performed to determine whether some of the non-ideal load-displacement response from varying toughness in the bonds.

5.2.1 Cohesive Zone Model

In elastic systems, the fracture behavior is captured by linear elastic fracture mechanics (LEFM). The crack tip is assumed to be atomically sharp such that the fracture energy is used in overcoming the surface energy of the interface and the process can be described by a single parameter: the fracture toughness. In brittle materials, this is a valid assumption. In systems involving ductile materials, LEFM holds as long as the plastic deformation at the crack tip is small (small scale yielding) such that the load-displacement behavior is essentially linear up to the point of crack growth [54, 76]. However, when there is significant plasticity, toughness alone cannot adequately describe the fracture behavior. Additional parameters – for instance, cohesive stress exerted at the crack tip or critical displacement– is also needed. A common approach is to assign a cohesive law to the material ahead of the physical crack tip. The problem can then be simulated numerically within a standard finite element model

[77].

The cohesive zone model uses a traction-separation law to describe the fracture process. The traction-separation law is defined by a peak stress and a displacement, above which the material cannot carry further loading and is thereby considered fractured. The shape of the curve usually does not significantly affect the fracture behavior of the system [76]. A general traction-separation law used by Yang and Thouless is shown in Figure 5-3 [78]. Each fracture mode has its own traction-separation law, consisting of a peak cohesive stress ($\hat{\sigma}$ in mode I or $\hat{\tau}$ in mode II), a critical displacement (δ_c), and an intrinsic toughness of the material (Γ_I or Γ_{II}), which is the area under the curve. Of the three parameters, the intrinsic toughness and peak cohesive stress are the important parameters from a mechanics point of view [76].

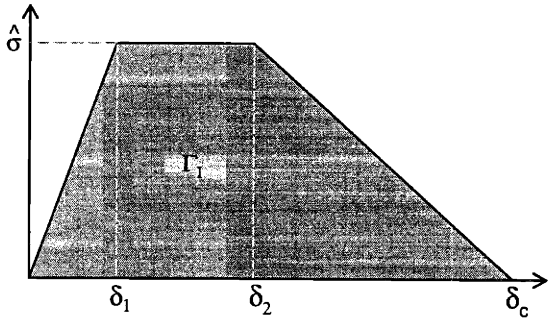

Figure 5-3: Schematic of a mode I traction-separation law used by Yang *et al.* [78]

The $\hat{\sigma}$ and $\hat{\tau}$ values used in the traction-separation laws could be found experimentally in separate tests. The intrinsic toughness could then be obtained by curve fitting various values to the load-deflection curves of the experimental data. Finally, δ_c values were calculated based on the given cohesive stress and intrinsic toughness. The cohesive zone model with the trapezoidal traction-separation law was implemented by Yang and Thouless to predict pure mode I, pure mode II as well as mixed mode fracture problems involving large scale plasticity [77, 78]. Good agreement between model and experimental results was found.

The cohesive zone model approach taken by Yang and Thouless was the basis for the numerical work that will be described in remainder of this section. In fact, Yang's

FORTRAN code, with some modifications, was used.

5.2.2 Model Description

The four-point bend tests were simulated using commercial finite element software ABAQUS, with a standard solver package [79]. Only half of the specimen was modeled. The 2-D models had the same dimensions as the actual test specimens: the upper and lower beam thicknesses were 525 and 450 μm, respectively. To simplify the analysis, the rollers were represented as point loads. The inner roller was placed 1 cm from the axis of symmetry, on top of the upper wafer. It was held fixed in the y-direction and the reaction force at that node was sought. The outer roller was located 1 cm away from the inner roller, below the bottom wafer, and given a constant y-displacement boundary condition. The mesh consisted of 4 noded plane strain elements. The elements near the interface were more refined, as shown in Figure 5-4, while those in the region between inner and outer rollers (x=1.2 to 2 mm) were coarser. The inset of Figure 5-4 also shows the 50 μm wide bonds represented by groups of 8 X's.

The Si beams were assigned to have elastic properties of 169 GPa and 0.22, respectively, as the Young's modulus and the Poisson's ratio. The beams were separated 1 μm apart, and the materials response of the bonding layer was described by the traction-separation law implemented in a 4 noded user-defined element. The three types of bond geometries created are shown in Figure 5-5: continuously bonded, periodic bonds (50 μm bonds separated by 250 μm spaces), and orthogonal four-point bend configurations (groups of 50 μm bonds separated by 250 μm spaces; each group is separated by 2 mm gaps).

The models were solved statically. The solver completes the displacement given by breaking the displacement into steps. Within each step, several iterations of the solution may be sought. As a non-linear problem, the accepted solution is one that meets the force equilibrium and displacement correction criteria, both of which were the default values. One item of note: it was found that the solver must not be allowed to extrapolate the solution when there are discontinuous bonds. Otherwise, an

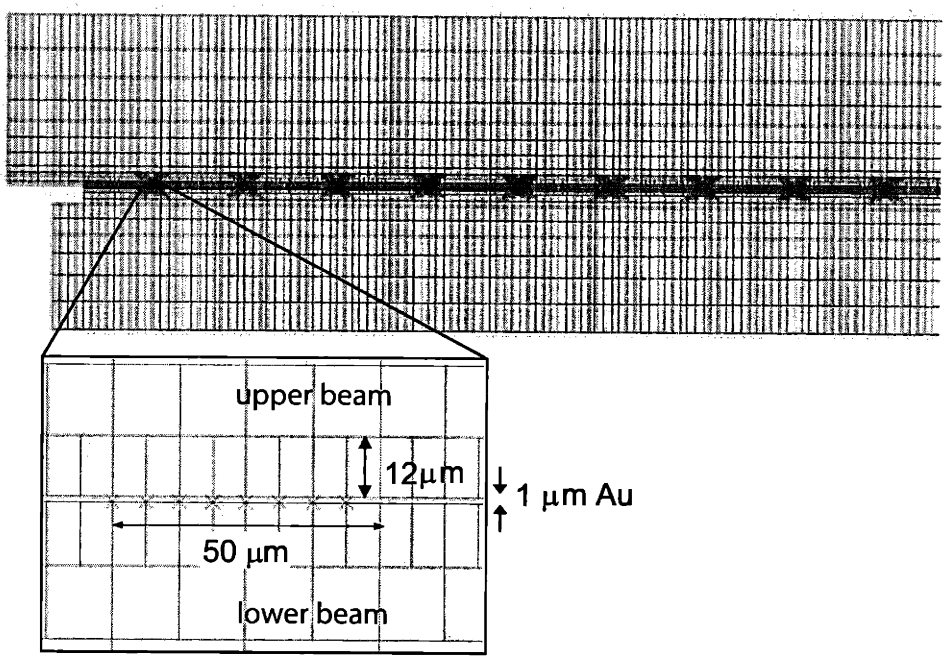

Figure 5-4: Mesh of four-point bend model with periodic bonds.

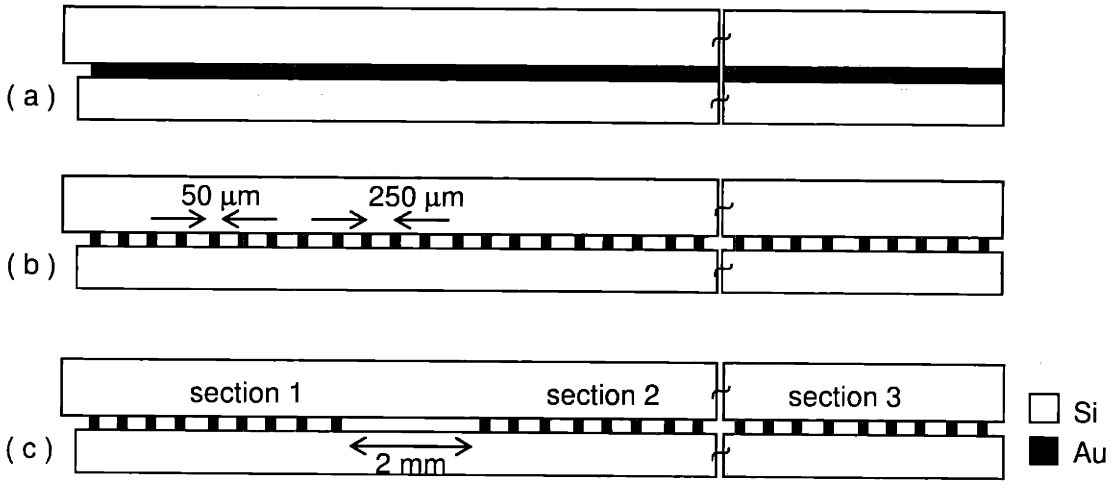

Figure 5-5: Schematic of geometries explored in the simulation. (a) Continuous bonds. (b) Periodic bonds. (c) Periodic bonds with spaces.

erroneous, step size dependent solution would result. The extrapolation was prevented by using the option, EXTRAPOLATION=NO, in the step command.

5.2.3 Traction-Separation Law

The traction-separation law was executed by a FORTRAN code, details of which may be found in Appendix D. The basic scheme of the code is as follows: for each element, the separation of the nodes on the upper and lower beams is found, then the traction followed by the toughness for that given displacement were calculated. This was done for both mode I and mode II at every node pair, defined in Figure 5-6. Then the toughness values were used to determine whether the failure criterion has been met. Of course, if the displacement of the nodes exceeds the critical displacement, the nodes are automatically released.

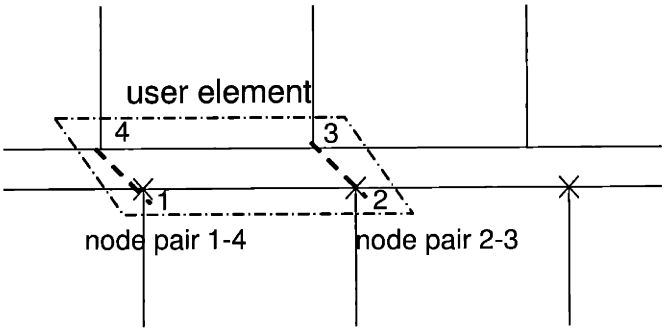

Figure 5-6: Schematic of the user element that defines the gold bonding layer.

Yang and Thouless used the following failure criterion [78]:

$$G_{crt} = \frac{G_1}{\Gamma_{Io}} + \frac{G_2}{\Gamma_{IIo}} = 1, \tag{5.1}$$

where G_1 and G_2 are the toughness at that displacement while Γ_{Io} and Γ_{IIo} are the intrinsic toughness in mode I and II, respectively. For mixed mode problems, the value of the two fractions depends on the mode mixture. In simulating the case of period bonds, it was found that elements carried loads even after the failure criterion had been met. In these cases, G_{crt} can be as high as 1.4. This was not the case with continuous bonds.

Difficulties in achieving convergence were also encountered in some instances with the code as written. The trapezoid contains two sharp corners, which may cause some numerical difficulty, especially on the unloading portion from δ_2 to δ_c. Since smooth curves tend to be more numerically stable, the traction-separation law was changed to a modified sine curve, as shown in Figure 5-7. The curve becomes a linear function for $\delta > 0.65\delta_c$. In order to obtain a more gentle slope in the unloading portion, which also helps with numerical stability, the actual completion of the curve occurs at 1.27 δ_c. The form of the traction law was considered a free variable, and as previously noted, the peak stress and the total toughness are the key variable, whereas the shape has relatively little influence.

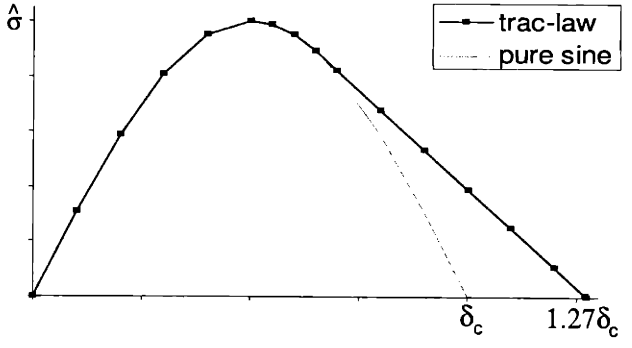

Figure 5-7: Schematic of the traction-separation law used in the simulations

For the four-point bend geometry being studied, the mode mixture is around 41°. To ensure nodal release with approximately equal G_1 and G_2, the failure criterion was also modified:

$$G_{crt} = \frac{G_1}{\Gamma_{Io}} + \frac{G_2}{0.1\Gamma_{IIo}} = 1. \tag{5.2}$$

5.2.4 Simulation Results

Since pure mode I or II fracture tests were not performed on the gold films, the traction-separation law parameters were generated based on expected toughness values and educated guesses as to $\hat{\sigma}$ and $\hat{\tau}$ values. Simulations show that loading was initially all shear, and subsequently the mode I contribution would progressively in-

crease. Approximately equal contribution from both modes was found at the point of separation. Several different combinations of $\widehat{\sigma}$, $\widehat{\tau}$ and δ_c having the same intrinsic toughness value were tried. The resultant load-displacement curves were not significantly affected by the choice of parameters, as reported by Thouless and Yang [76]. The discussion will thus focus on results that used the parameters listed in Table 5.1.

Table 5.1: Traction-separation law parameters.

	$\widehat{\sigma}$ [MPa]	δ_c [μm]	$\widehat{\tau}$ [MPa]	δ_{ct} [μm]	Γ_{Io} [J/m^2]	Γ_{IIo} [J/m^2]
A	9.25	0.65	5	1.2	4.46	4.45
A'	24	0.25	4	1.5	4.45	4.45
B	12	0.5	4.3	1.4	4.45	4.46
C	14	0.5	6.5	1.1	5.19	5.3
D	30	0.25	5	1.5	5.56	5.56
E	40	0.25	4	2.5	7.41	7.41

Continuous Bonds

In the continuously bonded case, constant load-displacement curves was obtained. In agreement with the findings of Charalambides *et al.* [38], the load also increased as the crack tip approached the inner roller. For parameter set A, the critical load, P_c, was 10.32 N. Using Equation 1.2, this correspond to a $\mathcal{G}_c$ of 8.20 J/m^2, which is -2.8% of the expected value based on Γ_{Io} and Γ_{IIo}. Agreement was excellent. Therefore, for bonds that were made with the gold lines parallel, constant loads are to be expected when the bond toughness is constant.

Periodic Bonds

In the periodic bonding case, the delamination of a pad was accompanied by a small decrease in the load, as might be expected. The minute decrease is not detectable on the scale used in Figure 5-9. The overall trend is a gradually increasing load as the crack propagated. The behavior resembles a weak R-curve behavior – but rather than reaching steady-state, the load began to decrease at a crack length around 6 mm. Based on the analysis of Charalambides *et al.*, propagation beyond 7.6 mm

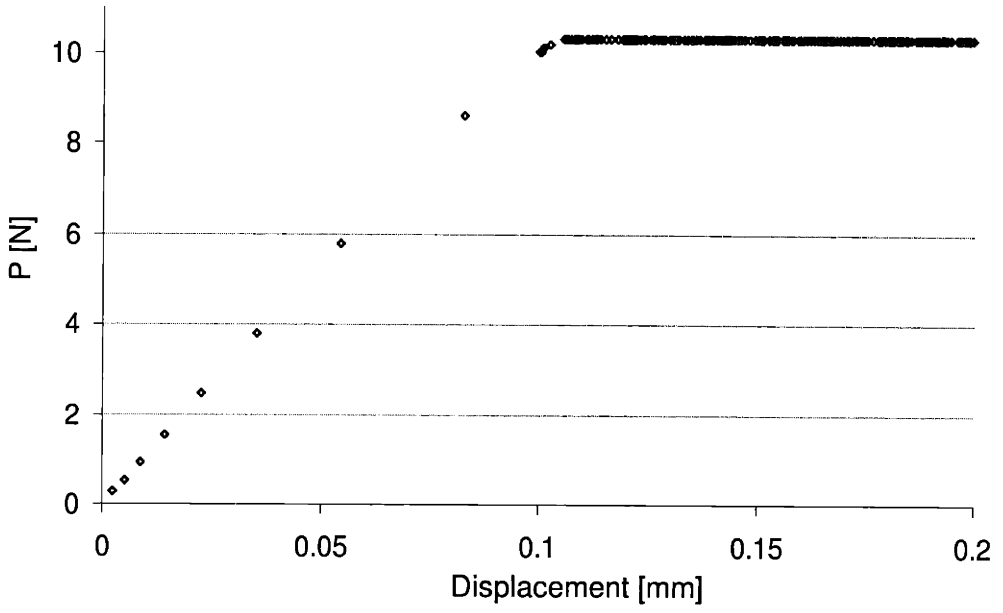

Figure 5-8: Load vs. displacement of continuous bonds with toughness of 8.2 J/m^2.

requires the load to increase, due to the decrease in moment as the crack approaches the inner roller. Indeed, Figure 5-9 shows a saddle shaped load-displacement curve after the load peak.

The strain energy from each pad as it delaminated was found to be stable, as dictated by the failure criterion and the traction-separation laws. However, the increase in load resulted in a gradual increase in $\mathcal{G}_c$, calculated using Equation 1.2. The $\mathcal{G}_c$ in the near notch region was lower while that corresponding to the load peak was higher than the expected $\mathcal{G}_c$. The average of the extrema matched the expected $\mathcal{G}_c$.

A real understanding of the cause of the pseudo-R-curve behavior in these periodic bonds would require further study, including formulation of the traction-separation law based on actual experimental data and reformulation of the traction law and its implementation in the finite element code. Speculation as to the cause can only be offered at this time. The simulation results have shown that loading of the bond pads began in shear, and the shear load may be carried by several pads ahead of the one that was under the highest load, which experiences both tensile and shear loads. Small tensile loads were typically found in one to two pads ahead of the first

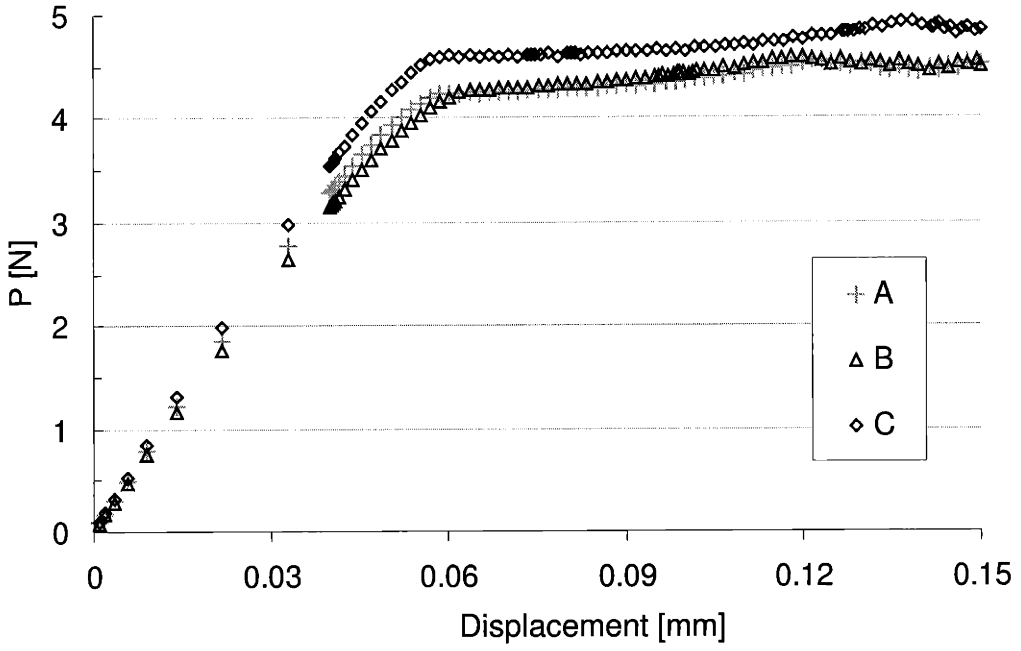

Figure 5-9: Load vs. displacement of periodic pads with constant toughness.

separated pad. This situation does resemble that of crack bridging problems. With each pad separated by 250 μm from its neighbors, the bridging distance can be quite significant. In the continuously bonded case, the crack propagated under constant load because the load carrying elements are contiguous and the process zone in which there is significant deformation does not run very far ahead of the actual crack tip.

Orthogonal bond configuration

The first two scenarios described above were simulated in order to gain confidence in the code. The geometry of interest, of course, is the orthogonal bond configuration, which is atypical of the geometry reported by other groups. The main geometric difference between the periodic structure and the one to be discussed in this section is that, in addition to the 250 μm spacing between pads, there is a 2 mm gap between pads 9 and 10. For reference, sections 1 and 2 will refer to pads 1 - 9 and pads 10 - 30 (which goes beyond inner roller), respectively.

The load-displacement behavior obtained was radically different from those discussed above. First, the load drop at the displacement of approximately 0.09 mm in

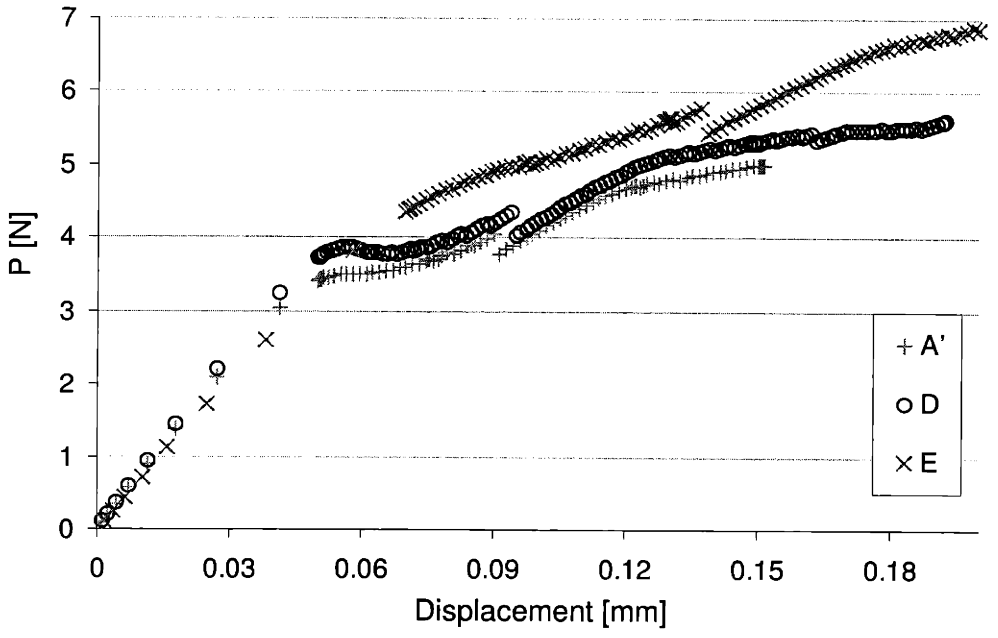

Figure 5-10: Load vs. displacement of orthogonally bonded pads with constant toughness.

Table 5.2: Toughness assignment in toughness variation simulation

case\pad	1	2	3	4	5	6	7	8	9		10	11	12	13-inner roller
v1	E							D		g	D			
v2	E			D				E		a	E	D		
v3	E			D			E			p	E	D		
v4	E										D			

Figure 5-10 corresponds to crack propagation from pad 9 to 10. This was expected because of the large gap between the two. Even though all the pads were assigned to have the same toughness in each case, the load was found to increase as the crack propagated. Moreover, there is a 20-25% increase in the average load going from section 1 to 2.

Observation of the fractured surfaces of actual specimens revealed variation in the degree of deformation, which may be a result of varying toughness. To determine the effects of varying toughness on the load-displacement curve, four simulations were run with two parameter sets, D and E, distributed amongst the pads. Details of the distribution are listed in Table 5.2.

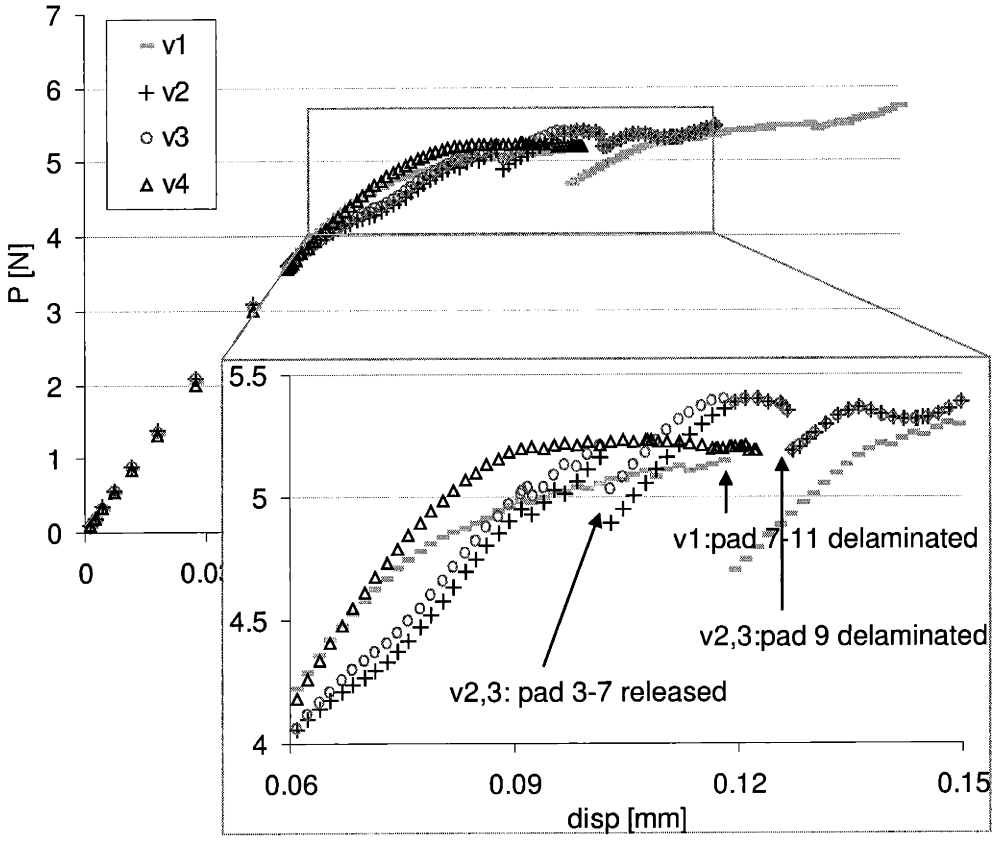

Figure 5-11: Load vs. displacement of orthogonally bonded pads with varying toughness.

The results will be discussed sequentially. In case v1, the material response of the first seven pads corresponded to parameter set E, which is higher than D. As shown in Figure 5-11, the first pad delaminated around 5 N, which is the same as the constant toughness case (E). As subsequent pad delaminated, the load did not increase to 5.8 N, but only went up to ~5.15 N before the entire section 1 was delaminated due to the presence of the lower toughness D in pads 8-9. The load then followed that of the pure D case, as the remainder of the pads were of that toughness.

In case v2, the toughness in section 1 was arranged such that pads with toughness D were sandwiched between higher toughness pads. Two load drops were observed in Figure 5-11. The second load drop at 0.128 mm has been discussed before: it occurred as pad 9 delaminated and the crack suddenly grew another 2 mm due to

the gap between the two sections. The cause of the first load drop requires some explanation. Pad 1 and 2 delaminated at displacements of 0.092 mm and 0.097 mm, respectively. Pad 3 would be expected to delaminate next, but that event coincided with the first load drop around 0.1 mm. The load decrease was a result of "free propagation" through pad 7 upon the delamination of pad 3. Recall that the lower toughness D was assigned to pads 4-7. As the beam was being loaded, strain energy was accumulating. While the energy was not enough to separate pads with cohesive properties of E, the $\mathcal{G}_{crt}$ of D was met. Hence delamination within the beam in pads 4-7 occurred before the first pad even delaminated. This event caused a slight compliance change corresponding to displacements between 0.07 and 0.08 mm that can be seen in Figure 5-11. Section 1 was completely delaminated after the second load drop and recovery. A load saddle was then found. Because pads 10-11 were again of the higher toughness, delamination beyond those pads began as loading continued. The simulation was stopped at a displacement around 0.155 mm because of convergence difficulties. At that point, pads 10 and 11 were still bonded but the crack tip had reached a distance greater than 7.5 mm, nearing the influence of the inner rollers.

Case v3 is very similar to v2, except that there were only three D pads that were sandwiched between E pads in section 1. Therefore, similar load-displacement behavior was found. The initial slope change before delamination of pad 1 is smaller, due to the shorter D region, and hence a stiffer beam than the v2 case.

The last case to be simulated is v4, where the entire section 1 is of toughness E and the rest of the beam was assigned toughness of D. Delamination of the pads occurred at a constant load around 5.2 N. Large scale bridging effect was also observed in this case, where pads 10 and 11 delaminated between the delamination events of pads 7 and 8. This simulation was not completed due to a convergence problem, which occurred soon after pad 8 was released. If the simulation could be completed, one would expect a large load drop when pad 9 delaminates since the process zone would be several mm ahead of the crack tip at that time.

Experimentally, the majority of the load-displacement curves exhibited sharp load

drops. Some did exhibit a more constant load as the crack propagated in the second section, while others maintained the choppy load peak-valley behavior. Some specimens indeed showed a lower first load peak, similar to ones found in the simulation with constant toughness, but that may be the result of an adhesive failure mode or inherently lower toughness in the bonds. In many instances, resemblance of simulations v2 or v3 were found experimentally. The experimental load-displacement curve showed compliance changes, but changes in crack opening was not detected during testing. Examination of the fractured surfaces of these specimens often revealed weak/poor bonds sandwiched between the better bonded ones. This is similar to the case that was analyzed and the behavior can thus be explained from the simulation results. The results of v1 also showed that the presence of a few lower toughness bonds may result in a more constant load-displacement behavior.

5.2.5 Fracture Simulation Conclusions

Modification of the traction-separation law used by Yang and Thouless improved the numerical convergency in the continuous bonding case. When the bonding layer was modeled as discontinuous, either periodically or ones with large separations within, convergence difficulty was still encountered. The problem would have to be solved with more advanced finite element techniques or more sophisticated models that account for dynamic effects, both of which were beyond the scope of this thesis.

However, much was learned from the relatively simple model presented herein. First, in the continuous bonded case, the simulation result showed excellent agreement with the analytical solution given by Equation 1.2 and the theoretical phase angle. As bonding becomes discontinuous, the simulation shows R-curve behavior even though a constant toughness was assigned. The validity of this result cannot be confirmed at the time of writing, given that majority of the test specimens showed varying toughness. Models having the geometry of orthogonally bonded specimens were also built, with the toughness of the bonds varied in different linear arrangements. While a 2-D model and incorporation of a binary toughness is an oversimplification of the complexity of the real system, load-displacement curves that broadly resemble some

experimental ones were found. Qualitatively, this analysis showed that some of the non-idealities found in the experimental curves – such as multiple load drops, changes in compliance with no definitive load plateau – are likely to be the results of varying toughness in the bonds over the area of the test specimens. Moreover, because the load obtained is a far-field measurement, the toughness calculated is an average toughness. A different testing technique would have to be employed to measure subtle variations on the local level. Finally, the simulation results also showed that a simple observation of the crack opening is insufficient to determine the crack length given that the bonds with lower toughness would delaminate if they were ahead of tougher bonds. The full load-displacement curve would have to be analyzed, rather than using a single P_c value. Thus, the technique may not be suitable if there is large variation in toughness distributed over the bonded wafer pair, or specimens cut from it.

5.3 Bond Pressure Distribution

The result of the toughness data showed large scatter that cannot be fully explained by process variations. In addition, nonuniform deformation was found on the fractured surfaces. In the orthogonal bonding configuration, there are 9 x 21 or 10 x 21 pads in the sections on either side of the notch and 21 x 21 pads in each section beyond those. Better bonding, in terms of more deformation, was found more frequently in the pads that were located around the edges of the sections. This observation, together with the qualitative agreement of the experimental results with the simulations of Section 5.2, led to hypothesis that there may be nonuniform pressure across the wafer during bonding. The local pressure is an important parameter in thermocompression bonding. It aids in overcoming some of the barriers imposed by the physical system, such as wafer waviness, and thickness and roughness variation, so that the gold surfaces may be brought to close proximity for bonding to take place. This section describes the modeling work performed to understand how pressure is distributed during the bonding process.

5.3.1 Model Description

The bonding process was simulated using ABAQUS with its standard solver package [79]. A 2-D model 4 mm wide, which encompassed half of a 21x21 pad section, was created with 8 noded plain strain elements. Symmetric boundary conditions in the x-direction were imposed on both ends of the structure. The mesh, shown in Figure 5-12, includes the 3 mm thick stainless steel diffusion plate which was placed on the wafer during the bonding operation. The Young's modulus and Poisson's ratio of the stainless steel are 193 GPa and 0.3, respectively. The wafer is 450 μm thick, with elastic properties of 169 GPa and 0.22 for the Young's modulus and Poisson's ratio, respectively. The 50 μm wide, 0.5 μm thick gold pads were modeled as elastic-plastic: the Young's modulus, Poisson's ratio and the yield stress are 70 GPa, 0.42, and 120 MPa, respectively. The yield stress of 120 MPa was chosen in order to simulate the maximum pressure applied in experiment.

The bottom of the pads were fixed in the y-direction to simulate bonding with the gold on the other wafer, which was not modeled, but represented by a rigid line. Three boundary conditions were simulated: uniform pressure applied to the wafer (with a structure that contained only the wafer and Au pads), uniform pressure applied on the stainless steel plate, and point load applied at the topmost, left corner node of the stainless steel plate. In all cases, the resultant mean pressure on the Au pads is 120 MPa. Each Au pad is formed by 20 columns and 4 rows of elements. The stress on the pad was obtained at the centroids of the elements located on the bottom row of each column.

5.3.2 Result and Discussion

In the model, the left edge of pad 1 is coincident with the axis of symmetry while pad 11 is closest to the diesaw alley. Figure 5-13 shows that the average stress per pad is not uniform from the center of the section to the edge where the diesaw alley is located. The edge pads experienced higher stress than the ones located near the center, in agreement with experimental observations. Moreover, on average, all three

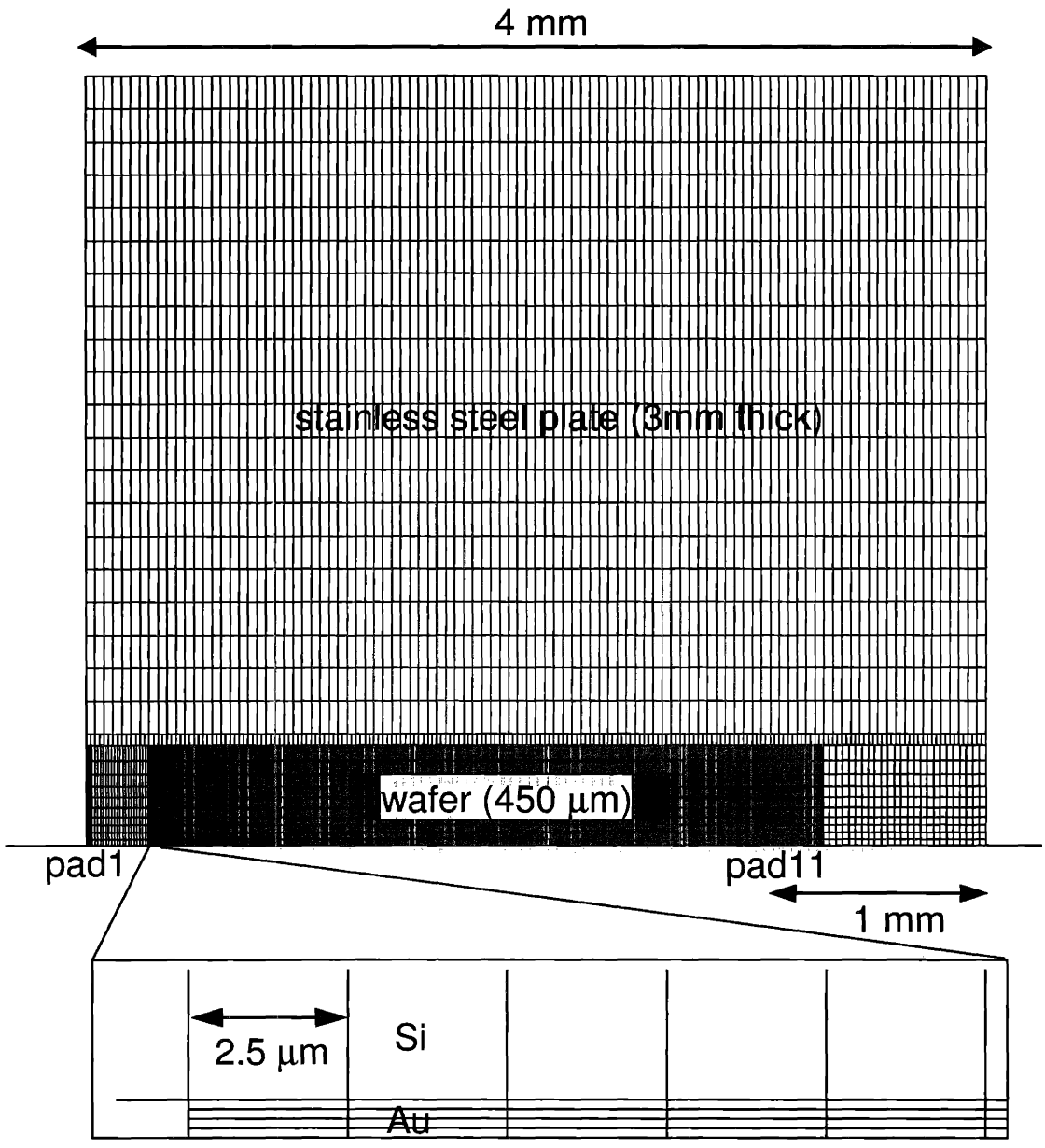

Figure 5-12: 2-D mesh of the bonding process model.

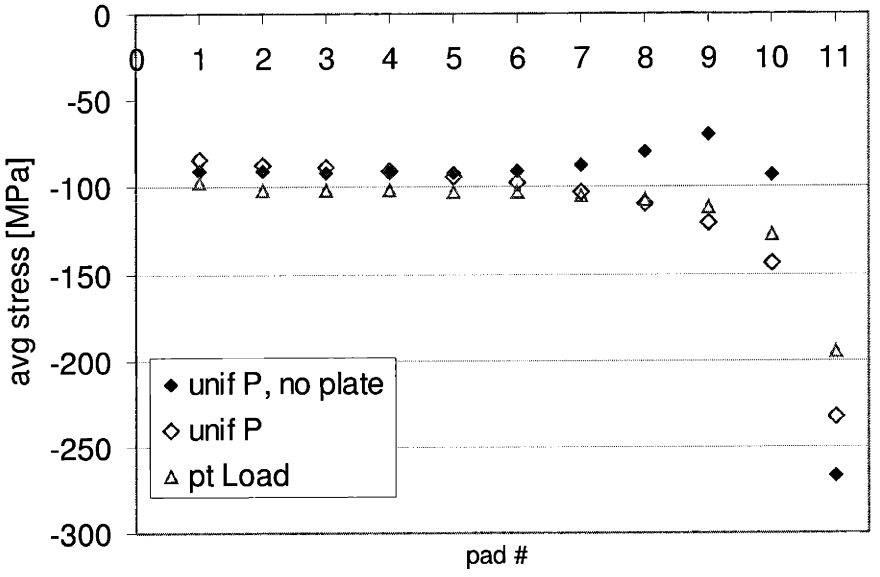

Figure 5-13: Average pressure per pad.

boundary conditions resulted in pads experiencing lower pressure than the nominal applied pressure of 120 MPa. The higher pressure exerted on the edge pads is most likely due to the 2 mm gap that separates sections of bond pads. Figure 5-14 shows the displacement of the wafer at the end of the structure (x=0.3 to 0.4 mm) that is not supported by Au pads underneath. The parabolic profile indicates bending in the wafer. Depending on the boundary condition, the wafers can actually touch near the center of the 2 mm gap.

Experimentally, evidence of wafers touching near the center of the diesaw alley was observed. This matches the result of the simulation of uniform pressure applied directly on the wafer, without the stainless plate. But given that there is a stainless steel plate which was pressed against the wafer in the actual bonding process, that is not a fully accurate boundary condition. The simulations with the stainless steel present should be more representative of the actual bonding condition. While the simulation results also showed bending of the wafer, the displacement was insufficient for the wafer to touch. This may seem to be a contradictory result. However, the model assumed a perfectly uniform Au thickness across a perfectly flat wafer that was pressed by a perfectly flat stainless steel plate. In actuality, the gold thickness

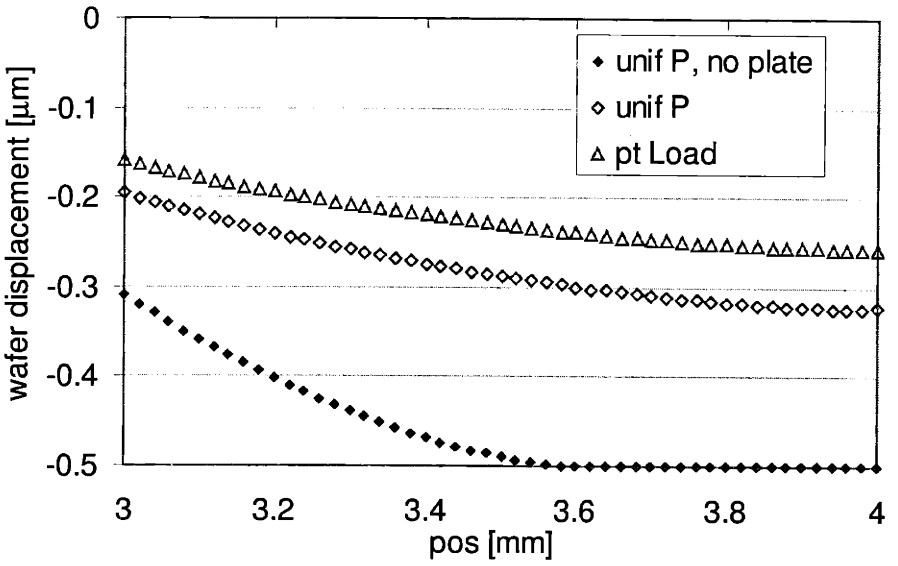

Figure 5-14: Displacement of the wafer in the diesaw alley.

is not uniform, wafer thickness variations and waviness exists, and the bonding tool itself has uniformity issues as well. These factors can cause pressure to redistribute and likely to produce an additional displacement.

The effectiveness of this simple 2-D model in capturing the key features of a 3-D situation was validated by H.S. Moon [80], who built a 3-D model of a quarter of the whole wafer. In his model, the wafer was modeled using shell elements and the Au pads as spring elements. A global simulation was performed, and the result was then used in a local model that had approximately 1/4 of the section (10 x 10 pads) laid out, as shown in Figure 5-15. The uniform pressure was applied without the stainless steel on top. The 3-D result matched very well with the result obtained from the simple 2-D model. Figure 5-16 also shows a nonuniform pressure distribution amongst the pads, with the edge pads experiencing higher pressure than the ones in the center. Because of the boundary condition, the lowest pressure was found in the pads immediately neighboring the edge pads, as in Figure 5-13.

More complicated models must be constructed in order to fully understand the source of the nonuniform bonding observed experimentally. The results of the simple 2-D model presented in this section indicates that some of the nonuniformity may be

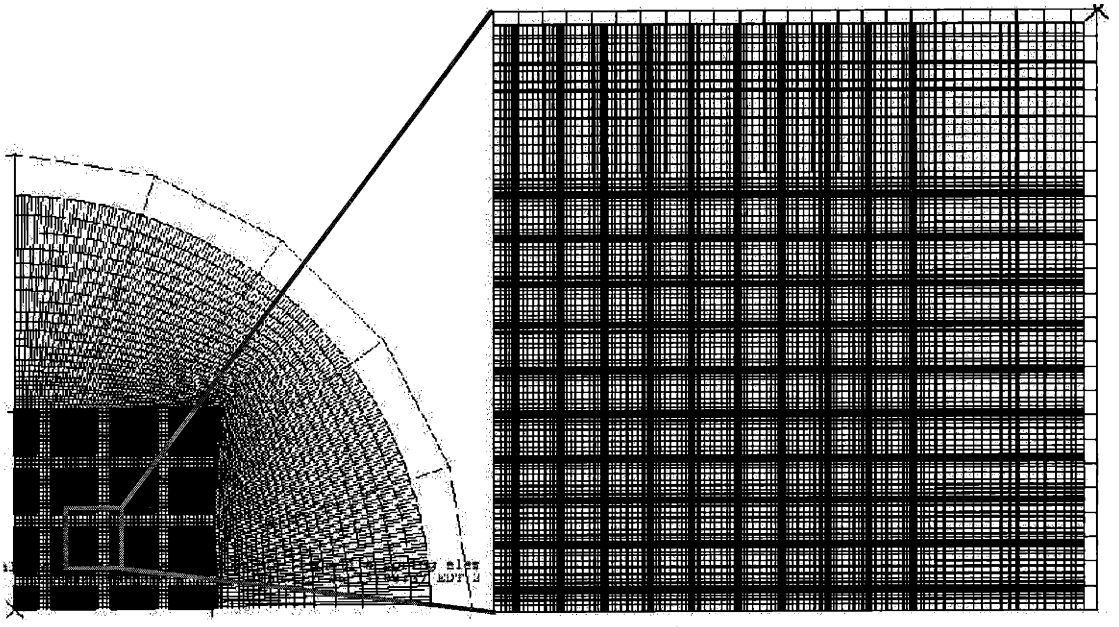

Figure 5-15: Mesh for the local 3-D model. Courtesy of H.-S. Moon.

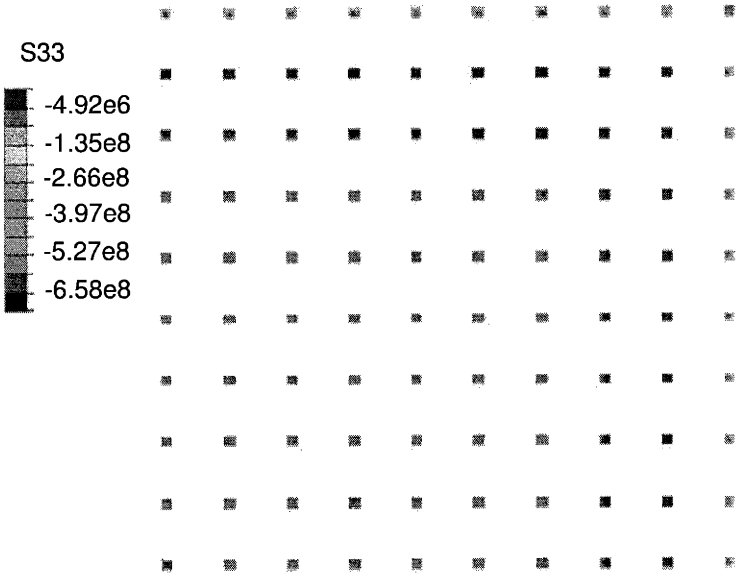

Figure 5-16: Pressure distribution in the pads from the 3-D model. Courtesy of H.-S. Moon.

a result of the layout, where long sections of the wafer were not supported by the Au. Therefore, the wafers undergoes bending during bonding under high applied pressure. This in turn results in a nonuniform pressure distribution across the wafer.

5.4 Conclusion

Finite element simulation results were presented in this chapter. The modeling was motivated by the nonuniform bonding that was found in the specimens and the non-ideal behaviors observed during testing. These models were quite simple, but some correlation between the simulation results and experimental observations and data were found.

The asymmetric delamination behavior of the specimens was shown not to affect the stress intensity at the crack tips. As long as the crack was propagating within the steady state regime, the specimen behaves no differently to the one that delaminates symmetrically.

The cohesive zone model was used to simulate the load-displacement behavior of the specimens. Although the traction-law parameters were chosen based on educated guesses, the result agreed very well with analytical solutions in the continuously bonded case. When discontinuous bonds were introduced in the specimen, pseudo R-curve behavior was found in the simulation results. By varying the toughness of the pads, qualitatively similar load-displacement curves to the experimental ones were obtained. Depending on the arrangement of the toughness variation, large scale bridging can be generated.

Lastly, the bonding process was simulated. Nonuniform pressure distribution due to the patterning of the bond pads was found, in agreement with experimental observation in some of the specimens.

Chapter 6

Conclusions

This chapter summarizes the experimental and finite element simulation results. A brief process guideline and discussion on the direction of future work conclude the thesis.

6.1 Thesis Summary

The first part of the thesis presented the process developed for the fabrication of wafer-level thermocompression bonds via a gold bonding layer. The process was designed to generate four-point bend test specimens so that a quantitative description of the bond toughness could be made. The chapter on fabrication included a discussion of the fabrication challenges encountered during the course of process development. One of the key issues was Si diffusion onto the Au surface, which was countered by incorporation of an oxide diffusion barrier. A 3000 Å thermal oxide barrier was found to be effective up to 300°C. Thicker oxide or nitride will have to be used for higher bonding temperatures. Guidelines for prevention of source spitting during e-beam deposition were presented. Lastly, the photolithography process was optimized once the image reversal process was understood.

Characterization of the bonds was focused on the effects of pressure, temperature and bond time on the bond toughness. The process window examined for the bond pressure, temperature, and time ranged from 1.25 to 120 MPa, 260 to 300°C, and 2 to

90 min, respectively. Large scatter in the bond toughness was found as plasticity was introduced into the system, either by increasing the bond layer thickness or increasing the bond pressure. Despite the scatter, several general trends have emerged from the data:

- Bonding can be achieved at 260°C, but bond toughness increased with increasing temperature and pressure. The $\mathcal{G}_c$ for specimens bonded at or below 7 MPa ranged in the tens of J/m^2. As bond pressure increased, from 30 to 120 MPa, the $\mathcal{G}_c$ as high as 400 J/m^2 was obtained.

- As the bond pressure increased, the plastic deformation on the fractured surface was more readily identifiable under an optical microscope. More energy is dissipated when materials plastically deform. The degree of plastic deformation on the fractured surface correlated with higher $\mathcal{G}_c$ in the majority of the specimens. However, energy can also be dissipated in adhesive failure via the adjacent metal layer, as discussed in [59]. Hence high values of $\mathcal{G}_c$ could be found even in specimens that did not fail cohesively.

- The percentage of bonded pads increased with increases in temperature or pressure. Nearly 100% yield was achieved when the applied pressure was 120 MPa, and the temperature was either 260 or 300°C.

- Bond improvement was not found with increasing time; in fact, virtually no difference in bond toughness was observed regardless of whether the specimen was bonded for 2 or 90 min.

The bonding process was simulated using the finite element method. The results showed a nonuniform pressure distribution during bonding purely as a result of the layout of the bond pads. The pads located near the edges of the sections were shown to undergo higher pressure than those in the center. This agreed with the experimental observations. Additional factors such as wafer bow, wafer and gold thickness variations, and surface roughness, would also affect the local pressure variations encountered in wafer bonding. The effect is more obvious when the applied pressure is

low. Experimentally, the highest applied pressure value resulted in virtually all the pads being bonded.

The toughness scatter could not be attributed entirely to process variations. Finite element modeling was performed to better understand the source of the scatter. Using a cohesive zone model, the fracture process of the specimens was simulated. When the bonds were continuous, excellent agreement with analytical prediction was found. The behavior of discontinuous bonds, formed when metal lines were bonded orthogonally, has not been previously reported in the literature. The simulation results showed an R-curve-like behavior in the load-displacement curve. Moreover, when the toughness of the bonds was varied, the cracks were found to propagate under varying loads. Specific cases of lower toughness pads sandwiched between higher toughness ones were simulated. The results from the simple model qualitatively resembled the experimental load-displacement curves. In the simulation, pads with lower toughness were found to delaminate as their $\mathcal{G}_c$ was reached. Depending on the arrangement, the crack tip can then run very far ahead of the pads that were assigned to have higher toughness. Changes in the compliance of the specimens may be observed even though the crack opening stayed fairly constant. Such behavior was believed to occur in many specimens, and thus explain some of the non-ideality in the load-displacement curves.

The results of the fracture simulation also address broader issues with the test technique. While the technique is favored for the independence of critical load and crack length, this assumption holds only if the toughness of the bond layer is nearly constant. For specimens that contain varying toughness, the entire load-displacement curve must be examined for changes in compliance. Unlike the finite element environment, the pads cannot be tracked individually. The delamination of bonds that are sandwiched between pads that remained bonded are difficult to detect experimentally. The only clues may be changes in compliance in the curve or load drops following observable changes in the crack opening. The "ideal" behavior of a constant load plateau generally does not exist in these situations. Compounded with asymmetric delamination, the determination of critical load or averages of loads may be difficult. Thus, the measured value of $\mathcal{G}_c$ do not necessarily reflect the bond toughness, or the

overall bond quality. The data presented in Sections 4.3-4.5 composed of four nominal $\mathcal{G}_c$ values per each specimen. In some cases, there was no doubt regarding the value of the P_c used in Equation 3.3. In others, the crack opening was used in conjunction with the load peaks to define the average P_c. Given that delamination of the inner pads may well have occurred, overestimation of $\mathcal{G}_c$ was possible in some cases. This is a general problem with the four-point bend delamination test applied to specimens of varying toughness, or discontinuous bonding.

6.2 Process Guidelines

Experimental results in Chapter 4 showed that bonding can be achieved at 260°C, well within the acceptable range for packaging applications. Although bonds can form at pressures as low as 1.25 MPa, the uniformity and yield are critical considerations for implementation in wafer-level packaging. Based on the data collected in this thesis, the following are the processing recommendations:

- The gold film should be deposited on diffusion barrier films such as oxide or nitride.
- As a process that forms bonds when clean metal asperities touch, the e-beam deposition process needs to be controlled to prevent source spitting. While the test structure used in the studies resulted in relatively flat surface, topography will be present in actual devices. It is believed that the process can tolerate surface topography, provided the bonding material is deposited at the highest locations and that wafer curvature is minimized whenever possible.
- The bonding layer thickness can be as thin as 0.25 μm. However, if large thickness variation across the wafer exists due to the device fabrication process, measures must be taken to ensure that the bonding layers can come into contact under the chosen pressure. Thicker films may be required, or the deposition may need multiple runs with substrates positioned differently during each run to compensate for the thickness variation.

- Surface treatment to remove organics, such as the UV-ozone exposure used in this work, is recommended.

- Typically, low processing temperature and pressure are preferred. A bonding temperature and pressure of 260°C and 120 MPa are recommended to ensure the level of repeatability and yield desired in manufacturing environments. Since the pressure may cause damage to the underlying thin films or other structural materials, a trade-off between pressure and temperature can be made. The decision would have to be made on an individual basis.

- The bond time was not shown to affect significantly the bond quality. Given the preference for faster turn-over, the bond time can be as short as 2 min.

- The linewidth should allow for misalignment. While wide seal rings waste valuable space on the wafer, rings that are too narrow may reduce reliability of the package. Linewidth on the order of 50 μm is a good starting point for initial process development.

- Finally, the layout should be designed to have more evenly spaced features to avoid geometry induced pressure nonuniformity. Dummy support structures may be incorporated.

6.3 Future Work

Wafer-level, gold-gold thermocompression bonding is an attractive technique for packaging of MEMS devices. Many of the salient features were described in Chapter 1. Results from the studies reported in this thesis have demonstrated the possibility of large area bonding, and that very high toughness bonds could be obtained. However, continued investigation is required before thermocompression bonding can be widely implemented for packaging applications.

For instance, bond toughness is a good metric for probing the process parameters. But bond toughness data does not translate into knowledge of the the reliability of

the package thus formed. Some form of functional test would have to be devised and carried out.

One of the advantages of gold thermocompression bonding is the possibility of hermetic sealing. This property was not studied in this work. In addition, the electrical performance of the devices thus packaged must be understood before this technology can be deployed in real applications. Based on the simulation results, the pressure nonuniformity stems, in part, from the gap between groups of lines. Work should be done to explore layouts that minimize the geometric effect on the pressure distribution. Features such as dummy support structures may minimize the pressure nonuniformity. Also, limits on wafer bow and flatness specifications for tooling must be determined.

On a more fundamental level, the basic mechanics of the process were not studied. The wafer bow or waviness may play a more important role than previously realized. Besides mechanics, the process would benefit from a better understanding of the materials properties. Section 2.6.1 on film characterization showed very fine grained as-deposited gold, indicating impurity incorporation. If the impurities diffuse to the gold surface during the heating period, the bonding process would be hampered, and relatively high pressure must be applied. Although purer films are obtainable under UHV systems, that option is not always available in manufacturing settings. Therefore, investigation into the effects of impurities and the means to minimize those effects, such as different surface treatment or bonding procedure, may reduce the pressure requirement and broaden the applicability of this bonding technology.

Appendix A

Fabrication flow

The following is a step-by-step description of the fabrication process flow.
Starting wafers: 4" n-type Si. Wafer thicknesses are 525 and 450 μm for regular (REG) and double side polished (DSP), respectively.

Feature	Wafer	Description
Alignment mark	DSP	Photolithogrphy, OCG825 resist, Mask GLOBAL-ALN Dry etch: ~0.5 μm (AME5000) Resist strip (piranha; 20:80 H_2O_2:H_2SO_4)
Trench (KOH)	DSP	RCA clean Oxidation: 20min/40min/20min dry/wet/dry Photolithography, OCG825 resist, Mask KOH Coat backside Wet etch oxide (BOE) Resist strip (piranha) KOH etch: 20%, 80°C, ~50 min (60-70μm deep) Post KOH-clean (double piranha)
Trench Perimeter	DSP	Photolithography, AZ4620 resist, Mask PERIMETER Dry etch: 1-2 μm (AME5000) Resist strip (piranha)

Feature	Wafer	Description
Oxidation	Both	RCA clean Oxidation: 20/40/20min dry/wet/dry
Pattern resist mask	REG	HMDS (optional, often used)
	Both	Coat AZ5214. Spread: 30s at 1500rpm Prebake: 30 min at 90°C Expose: 20s (KS2) with Mask METAL Flat bake: $\sim$ 90s at 120°C Flood expose: 180s (KS2) or 45s (EV1) Develop and inspection
Metal deposition	Both	e-beam deposition: 10 nm Ti, varying thickness Au; use lift-off plate w/ rotation
Lift-off	Both	Soak in acetone, remove excess metal, 1-2 min ultrasonic agitation
Organic clean	Both	Acetone and methanol (5 min in each) DI rinse, spin-dry 90 min UV-ozone exposure
Bonding	Both	Align wafers (immediately after UV exposure) Bond wafers: N_2 purge, pump down to 2 mbar, heat to bond temperature, wait 3 min, piston down, withdraw flags, apply pressure, cool
Diesaw		Dice: 8 mm wide specimens, mode E (2 successive cuts at different depths)

Appendix B

MATLAB code: Fractured surface image processing

The following are the MATLAB functions used to process the optical micrographs of the fractured surfaces and generate Figure 4-10. File "improc.m" is the main program that adjusts for minor misalignments in the the original greyscale images and converts the resulting image file into one that has a uniform background (SiO_2). The program invokes several functions, which were written as separate files. Lastly, file "justcount.m" determined the percentage of pads that meets the bonding criterion.

improc.m

```
% Process greyscale images using some built-in functions
% to even out illumination nonuniformity and write the images
% to filenames that begin with "n-"

file = importdata('list.txt');
[total_file] = length(file);
lines = 10;

for f=1:total_file,
  filename = char( file(f) );
  A = imread (filename, 'jpeg');
  [row,col] = size(A);
  r = fix (row/21);
  c = fix (col/lines);
```

```
  rbig = r*3;
  fprintf(1,'*** Processing %s (file %i of %i)\n', filename, f ...
     total_file);

  background = imopen(A, strel('square', 20));
  A2 = imsubtract(A,background);

  for i = 1:21,
    sec = A2( r*(i-1)+1 : r*i, :);

    for k = 1:lines,
      small = sec(:, c*(k-1)+1: c*k);
      sec3 = imadjust(small, stretchlim(small), [0 1]);
      sec(:, c*(k-1)+1: c*k) = sec3;
    end

    A( r*(i-1)+1 : r*i, :) = sec;
  end        %% intensity has been evened out %%

  A(A > 235) = 250;

  for i = 1:7,
    sec = A( rbig*(i-1)+1 : rbig*i, :);
    output = colpass(sec);
    A( rbig*(i-1)+1 : rbig*i, :) = output;
  end

  for i = 1:21,
    sec = A( r*(i-1)+1 : r*i, :);
    k=i;
    output = rowpass(sec,k); %% adjusts for angular misalignment %%
    A( r*(i-1)+1 : r*i, :) = output;
  end

  A(21*r+1:row, :) = [];
  out = ['n-', filename];
  imwrite(A, out, 'jpeg', 'Quality', 100);

end
```

==========

function: colpass

==========

```
function y = colpass(A)

% Turn oxides into columns of blacks.  Assume 9 px wide.
% Takes matrix A and returns A after the change.

proc = sum(A==250);
darks = sum(A<150);

flag = 0;

i = 0;
while (i < length(proc))
%  keyboard
  i = i + 1;
  if flag == 0
    % Have we hit the first non-zero entry yet?
    if proc(i) > 0
      flag = 1;
      start_index = i;
    end
  else
    % Look for last entry
    if proc(i) == 0
      flag = 0;
      last_index = i-1;
      width = last_index - start_index + 1;

      % Is it wide enough?
      while (width < 9)
        if last_index == length(proc)
          proc(start_index -1) = proc(start_index);
          start_index = start_index - 1;
        elseif darks(start_index-1) < darks(last_index+1)
          proc(start_index-1) = proc(start_index);
          start_index = start_index - 1;
        else
          proc(last_index+1) = proc(last_index);
          last_index = last_index + 1;
          i = i+1;
        end
        width = width+1;
```

```
      end

      % Is it too wide?
      while (width > 9)
        if start_index == 1
          proc(last_index-1) = proc(last_index);
          last_index = last_index - 1;
        elseif last_index == length(proc)
          proc(start_index-1) = proc(start_index-2);
          start_index = start_index - 1;

        elseif darks(start_index) > darks(last_index)
          proc(start_index) = 0;
          start_index = start_index - 1;
        else
          proc(last_index) = 0;
          last_index = last_index - 1;
        end
        width = width-1;
      end
    end
  end
end

mask = ones(size(A,1),1) * proc;
A( find(mask==0) ) = 1;

y = A;
```

==========

function: rowpass

==========

```
 function y = rowpass(A,k)

% Used after colpass program -- turn Au into rows of whites.
% Assume each Au line is 9 pixel wide and 10 pixel tall.
% Takes matrix A and returns A after the change.

c = fix(size(A,2) / 7);
main = sum(A' > 215);
[dummy,M_start] = min(main);

for i=1:7,
  a = A(:, c*(i-1)+1 : c*i);
```

```
  colproc = sum(a > 50);
  mask = ones(size(a,1),1) * colproc;
  a( find(mask==0) ) = 1;
  width = 1;
  proc = sum(a' > 215);
  orig = proc;
  proc(:) = 200;
  [dummy,start_index] = min(orig);

  if  ( (abs(M_start - start_index) > 8) | start_index == 1),
    start_index = M_start;
  end
  proc(start_index) = orig(start_index);
  last_index = start_index;

  while (width < 10)
    if start_index == 1
      proc(last_index+1) = orig(last_index+1);
      last_index = last_index + 1;
    elseif last_index == length(proc)
      proc(start_index-1) = orig(start_index-1);
      start_index = start_index - 1;
    elseif orig(start_index-1) > orig(last_index+1)
      proc(last_index+1) = orig(last_index+1);
      last_index = last_index + 1;
    else
      proc(start_index-1) = orig(start_index-1);
      start_index = start_index - 1;
    end
    width = width+1;
  end

  mask2 = proc' * ones(1,size(a,2));
  mask3 = (mask > 0) .* (mask2 == 200);
  a( find(mask3 == 1) ) = 250;
  A(:, c*(i-1)+1 : c*i) = a;

end
y = A;
```

```
=======================================
justcount.m
=======================================

file = importdata('count10.txt'); % use appropriate list
[total_file] = length(file);
%n_unbonded = ones(total_file,1);  % # pads not bonded in file
%n_fubonded = ones(total_file,1);  % # pads totally bonded in file

lines = 10;  % number of vertical lines in file.

for f=1:total_file,

  filename = char( file(f) );
  A = imread (filename, 'jpeg');
  fprintf(1,'*** Processing %s (file %i of %i)\n', filename, ...
      f, total_file);
  [row,col] = size (A);
  A( A  >= 247) = 250;

  b_80 = zeros (lines, 1);  B_80 = zeros (lines, 1);
  b_70 = zeros (lines, 1);  B_70 = zeros (lines, 1);
  b_60 = zeros (lines, 1);  B_60 = zeros (lines, 1);
  b_45 = zeros (lines, 1);  B_45 = zeros (lines,1);
  b_30 = zeros (lines, 1);  B_30 = zeros (lines, 1);
  b_15 = zeros (lines, 1);  B_15 = zeros (lines, 1);
  b_10 = zeros (lines, 1);  B_10 = zeros (lines, 1);
  b_3 = zeros (lines, 1);  B_3 = zeros (lines, 1);

  r = fix (row/21);  m = fix (col/lines);

  for i=1:21,
   sec = A( r*(i-1)+1 : r*i, :);

   %  count by column
   for k=1:lines,
     %  find # columns that are white (using the the 1st row)
     n = sum(sum( sec(1, m*(k-1)+1 : m*k) == 250 ));
     if n == 0
       percentage = 0;
     else
       %  find the total pixels that are white/grey
       w = sum(sum( sec(:, m*(k-1)+1 : m*k) == 250 ));
       grey = sum(sum( sec(:, m*(k-1)+1 : m*k) > 227 ));
       %  find the percentage of pixels that are white/grey
```

```
        percentage = (w - n*(r-10)) / (n*10);
        percentage2 = (grey - n*(r-10)) / (n*10);

        %  count as 1 if it's got > x% unbonded
        b_80(k) = (percentage >= 0.8);
        b_70(k) = (percentage >= 0.7);
        b_60(k) = (percentage >= 0.6);
        b_45(k) = (percentage >= 0.45);
        b_30(k) = (percentage >= 0.3);
        b_15(k) = (percentage >= 0.15);
        b_10(k) = (percentage >= 0.10);
        b_3(k)  = (percentage >= 0.03);
      end
    end

    B_80(i) = sum(b_80);  B_70(i) = sum(b_70);  B_60(i) = sum(b_60);
    B_45(i) = sum(b_45);  B_30(i) = sum(b_30);  B_15(i) = sum(b_15);
    B_10(i) = sum(b_10);  B_3(i) = sum(b_3);

  end

  p80 = sum(B_80); p70 = sum(B_70); p60 = sum(B_60); p45 = sum(B_45);
  p30 = sum(B_30); p15 = sum(B_15); p10 = sum(B_10); p3 = sum(B_3);

  pert80 = (p80 / (21*lines)) * 100; % [%] pads w >80% white
  pert70 = (p70 / (21*lines)) * 100;
  pert60 = (p60 / (21*lines)) * 100;
  pert45 = (p45 / (21*lines)) * 100;
  pert30 = (p30 / (21*lines)) * 100;
  pert15 = (p15 / (21*lines)) * 100;
  pert10 = (p10 / (21*lines)) * 100;
  pert3 = (p3 / (21*lines)) * 100;

  fid = fopen('result.txt', 'a');

  fprintf( fid, '%s \t %3.3f \t %3.3f \t %3.3f \t %3.3f \t %3.3f \t ...
     %3.3f \t %3.3f \t %3.3f \n', filename, pert80, pert70, pert60, ...
     pert45, pert30, pert15, pert10, pert3);
  fclose(fid);

end
```

Appendix C

ABAQUS code: Fracture process

The following is the ABAQUS input file used to simulate the fracture process, of the actual specimens. The FORTRAN code is invoked by the "*USER ELEMENT" command.

```
*HEADING
*PREPRINT,HISTORY=NO,MODEL=NO
**4pt bend configuration, all toughness same.
**
*NODE
    1,      0,       0
    1921,   12.0e-3, 0
    2081,   20.0e-3, 0
    18001,  0,       3.9e-4
    19921,  12.0e-3, 3.9e-4
    20081,  20.0e-3, 3.9e-4
    30001,  0,       4.50e-4
    31921,  12.0e-3, 4.50e-4
    32081,  20.0e-3, 4.50e-4
    33001,  0,       4.51e-4
    34921,  12.0e-3, 4.51e-4
    35081,  20.0e-3, 4.51e-4
    45001,  0,       5.11e-4
    46921,  12.0e-3, 5.11e-4
    47081,  20.0e-3, 5.11e-4
    66001,  0,       9.76e-4
    67921,  12.0e-3, 9.76e-4
    68081,  20.0e-3, 9.76e-4
```

```
**
**          --- create wafer nodes ---
*NGEN, NSET=b1
    1,      1921, 1
    1921,   2081, 1
*NGEN, NSET=b2
    18001,  19921, 1
    19921,  20081, 1
*NGEN, NSET=b3
    30001,  31921, 1
    31921,  32081, 1
*NGEN, NSET=t1
    33001,  34921, 1
    34921,  35081, 1
*NGEN, NSET=t2
    45001,  46921, 1
    46921,  47081, 1
*NGEN, NSET=t3
    66001,  67921, 1
    67921,  68081, 1
*NFILL, bias=1.15
    b1, b2, 6,  3000
    b2, b3, 4,  3000
*NFILL, bias=0.85
    t1, t2, 4,  3000
    t2, t3, 7,  3000
**
****        reference nodes for MPC ****
*NSET, NSET=t_left1, GENERATE
    36041, 37919, 2
*NSET, NSET=t_mid1, GENERATE
    36042, 37920, 2
*NSET, NSET=t_right1, GENERATE
    36043, 37921, 2
*NSET, NSET=t_left2, GENERATE
    39041, 40917, 4
*NSET, NSET=t_mid2, GENERATE
    39043, 40919, 4
*NSET, NSET=t_right2, GENERATE
    39045, 40921, 4
**
*NSET, NSET=b_left1, GENERATE
    27041, 28919, 2
*NSET, NSET=b_mid1, GENERATE
    27042, 28920, 2
```

```
*NSET, NSET=b_right1, GENERATE
    27043, 28921, 2
*NSET, NSET=b_left2, GENERATE
    24041, 25917, 4
*NSET, NSET=b_mid2, GENERATE
    24043, 25919, 4
*NSET, NSET=b_right2, GENERATE
    24045, 25921, 4
**
**
** ELEMENTS
**          --- create elements in wafers ---
*ELEMENT, type=CPE4
    4007,   25,    29,    3029,  3025
    4481,   1921,  1922,  4922,  4921
    8211,   18041, 18045, 21045, 21041
    9611,   24041, 24043, 27043, 27041
    10551,  25921, 25922, 28922, 28921
    10801,  27041, 27042, 30042, 30041
**
    13001,  33001, 33005, 36005, 36001
    13011,  33041, 33042, 36042, 36041
    14891,  34921, 34922, 37922, 37921
    15511,  36041, 36043, 39043, 39041
    16701,  39001, 39005, 42005, 42001
    17181,  40921, 40922, 43922, 43921
**
*ELGEN, ELSET=DSPwf
    4007,   474, 4, 1,  6, 3000, 700
    4481,   160, 1, 1,  8, 3000, 700
    8211,   470, 4, 1,  2, 3000, 700
    9611,   940, 2, 1
    10551,  160, 1, 1,  2, 3000, 2130
    10801,  1880,1, 1
*ELGEN, ELSET=REGwf
    13001,  10, 4, 1,  2, 3000, 2500
    13011,  1880, 1, 1
    14891,  160, 1, 1,  2, 3000, 1570
    15511,  940, 2, 1
    16701,  480, 4, 1,  9, 3000, 700
    17181,  160, 1, 1,  9, 3000, 700
**
**          --- create pad elements ---
*USER ELEMENT,node=4,TYPE=U1,properties=8,coordinates=2,variable=2,unsymm
    1, 2
```

```
*ELEMENT, TYPE=U1
    1,      30073,  30074,  33074,  33073
    9,      30121,  30122,  33122,  33121
    17,     30169,  30170,  33170,  33169
    25,     30217,  30218,  33218,  33217
    33,     30265,  30266,  33266,  33265
    41,     30313,  30314,  33314,  33313
    49,     30361,  30362,  33362,  33361
    57,     30409,  30410,  33410,  33409
    65,     30457,  30458,  33458,  33457
    121,    30793,  30794,  33794,  33793
    129,    30841,  30842,  33842,  33841
    137,    30889,  30890,  33890,  33889
    145,    30937,  30938,  33938,  33937
    153,    30985,  30986,  33986,  33985
    161,    31033,  31034,  34034,  34033
    169,    31081,  31082,  34082,  34081
    177,    31129,  31130,  34130,  34129
    185,    31177,  31178,  34178,  34177
    193,    31225,  31226,  34226,  34225
    201,    31273,  31274,  34274,  34273
    209,    31321,  31322,  34322,  34321
    217,    31369,  31370,  34370,  34369
    225,    31417,  31418,  34418,  34417
    233,    31465,  31466,  34466,  34465
    241,    31513,  31514,  34514,  34513
    249,    31561,  31562,  34562,  34561
    257,    31609,  31610,  34610,  34609
    265,    31657,  31658,  34658,  34657
    273,    31705,  31706,  34706,  34705
    281,    31753,  31754,  34754,  34753
    2005,   31945,  31946,  34946,  34945
**
*ELGEN, ELSET=pads
    1,      8,  1,  1
    9,      8,  1,  1
    17,     8,  1,  1
    25,     8,  1,  1
    33,     8,  1,  1
    41,     8,  1,  1
    49,     8,  1,  1
    57,     8,  1,  1
    65,     8,  1,  1
    121,    8,  1,  1
    129,    8,  1,  1
```

```
    137,    8,  1,  1
    145,    8,  1,  1
    153,    8,  1,  1
    161,    8,  1,  1
    169,    8,  1,  1
    177,    8,  1,  1
    185,    8,  1,  1
    193,    8,  1,  1
    201,    8,  1,  1
    209,    8,  1,  1
    217,    8,  1,  1
    225,    8,  1,  1
    233,    8,  1,  1
    241,    8,  1,  1
    249,    8,  1,  1
    257,    8,  1,  1
    265,    8,  1,  1
    273,    8,  1,  1
    281,    8,  1,  1
    2005, 22, 6, 1
**
**  -- assign trac-sep law properties [J/m^2, MPa] ---
** format:  σ̂, 0.15, 0.65, δ_c, τ̂, 0.15, 0.65, δ_c
**
*UEL PROPERTY, ELSET=pads
** 9.25e6, 0.15, 0.65, 0.65e-6, 5e6, 0.15, 0.65, 1.2e-6 (V)
**   24e6, 0.15, 0.65, 0.25e-6, 4e6, 0.15, 0.65, 1.5e-6  (V2)
**   12e6, 0.15, 0.65, 0.5e-6, 6e6, 0.15, 0.65, 1.0e-6 (W)
**   14e6, 0.15, 0.65, 0.5e-6, 6.5e6, 0.15, 0.65, 1.1e-6 (X)
**   30e6, 0.15, 0.65, 0.25e-6, 5e6, 0.15, 0.65, 1.5e-6 (X2)
**   40e6, 0.15, 0.65, 0.25e-6, 4e6, 0.15, 0.65, 2.5e-6 (J)
**
***** MATERIAL PROPERTIES ********
**
*solid section, ELSET=DSPwf, material=Si
*solid section, ELSET=REGwf, material=Si
**
*Material, name=Si
*Elastic 1.69e+11, 0.22
**
**
***** BOUNDARY CONDITIONS  ********
**
*NSET, NSET=fixed_node
    67601
```

```
*NSET, NSET=load_node
    2081
*NSET, NSET=vert, GENERATE
    33001, 66001, 3000
*NSET, NSET=disp
    30041, 33041
**
*MPC
    LINEAR, t_mid1, t_left1, t_right1
    LINEAR, t_mid2, t_left2, t_right2
    LINEAR, b_mid1, b_right1, b_left1
    LINEAR, b_mid2, b_right2, b_left2
**
*BOUNDARY
    fixed_node, 2
    vert,   xsymm
**
****** STEP 1 ******
**
*STEP, INC=1800, NLGEOM
*STATIC
  0.025, 1.0, 1.0e-10, 0.3
*BOUNDARY, type=displacement
  load_node,  2, 2, 0.00007
**
*Restart, write
*Node print, NSET=fixed_node, SUMMARY=NO
RF2
*Node print, NSET=disp, SUMMARY=NO
U2
*END STEP
**
******** STEP 2 ************
**
*STEP, INC=1800, NLGEOM, EXTRAPOLATION=NO
*STATIC
   0.0025, 1.0, 1.0e-10, 0.01
*BOUNDARY, type=displacement
  load_node,  2, 2, 0.0002
*Restart, write
*Node print, NSET=fixed_node, SUMMARY=NO
RF2
*Node print, NSET=disp, SUMMARY=NO
U2
*END STEP
```

Appendix D

FORTRAN code: Cohesive zone model

The following is the FORTRAN code that defined the traction-separation law used in the simulation of the fractured process. The original code was created by Qingda Yang. Modifications/additions are commented with CHT.

```
SUBROUTINE UEL(RHS,AMATRX,SVARS,ENERGY,NDOFEL,NRHS,NSVARS,
 1  PROPS,NPROPS,COORDS,MCRD,NNODE,U,DU,V,A,JTYPE,TIME,DTIME,
 2  KSTEP,KINC,JELEM,PARAMS,NDLOAD,JDLTYP,ADLMAG,PREDEF,NPREDF,
 3  LFLAGS,MLVARX,DDLMAG,MDLOAD,PNEWDT,JPROPS,NJPROP,PERIOD)

INCLUDE 'ABA_PARAM.INC'

DIMENSION RHS(MLVARX,*),AMATRX(NDOFEL,NDOFEL),PROPS(*),
 1  SVARS(*),ENERGY(8),COORDS(MCRD,NNODE),U(NDOFEL),
 2  DU(MLVARX,*),V(NDOFEL),A(NDOFEL),TIME(2),PARAMS(*),
 3  JDLTYP(MDLOAD,*),ADLMAG(MDLOAD),DDLMAG(MDLOAD,*),
 4  PREDEF(2,NPREDF,NNODE),LFLAGS(*),JPROPS(*)

DIMENSION C_COOR(2,4), R_COOR(2,4), R_F(8), R_MATRX(8,8)
open(unit=16, file='D:\chtsau\sinfunc2\D4_ou.dat',access='append')

SCAP=PROPS(1)
RTN1=PROPS(2)
RTN2=PROPS(3)
```

```
      DLTN=PROPS(4)

      PI=3.14159265D0                                          ! CHT
      Q=RTN2-TAN(PI*RTN2)/PI                                   ! CHT

      G_IC=SCAP*DLTN/PI*(1.0D0-COS(PI*RTN2)) -
     1    0.5D0*SCAP*DLTN*SIN(PI*RTN2)*TAN(PI*RTN2)/PI         ! CHT

      TCAP=PROPS(5)
      RTT1=PROPS(6)
      RTT2=PROPS(7)
      DLTT=PROPS(8)

      G_IIC=TCAP*DLTT/PI*(1.0D0-COS(PI*RTT2)) -
     1    0.5D0*TCAP*DLTT*SIN(PI*RTT2)*TAN(PI*RTT2)/PI         ! CHT

CCC   initialize the local variables
      G_I_14=0.0001D0
      G_II_14=0.0001D0
      G_I_23=0.0001D0
      G_II_23=0.0001D0
      G_CRT_14=0.0001D0
      G_CRT_23=0.0001D0

CCC   SYMBOL_1 and SYMBOL_2 are solution dependable variables. SYMBOL_1
C     > 1 means NODE1 and NODE4 have been separated and will never
C     support any load thereafter. SYMBOL_2 controls the same relation
C     between NODE2 and NODE3.

      SYMBOL_1=SVARS(1)
      SYMBOL_2=SVARS(2)

      DO 100 K1=1,NDOFEL
      DO 110 KRHS=1,NRHS
        RHS(K1,KRHS)=0.0D0
110   CONTINUE
      DO 120 K2=1,NDOFEL
        R_MATRX(K2,K1)=0.0D0
120   CONTINUE
100   CONTINUE

      DO 130 I=1,8
      R_F(I)=0.0
      DO 130 J=1,8
      R_MATRX(I,J)=0.0D0
```

```
130 CONTINUE


CCC  compute the length and thickness of an EPZ element (assume that
CC   the length does not change much with deformation)
    ALEN1=SQRT((COORDS(1,1)-COORDS(1,2))**2 +
    1   (COORDS(2,1)-COORDS(2,2))**2.0)
    ALEN2=SQRT((COORDS(1,4)-COORDS(1,3))**2 +
    1   (COORDS(2,4)-COORDS(2,3))**2.0)
    ALEN=(ALEN1+ALEN2)/2.0D0

    THIK1_0=SQRT((COORDS(1,1)-COORDS(1,4))**2 +
    1   (COORDS(2,1)-COORDS(2,4))**2.0)
    THIK2_0=SQRT((COORDS(1,2)-COORDS(1,3))**2 +
    1   (COORDS(2,2)-COORDS(2,3))**2.0)

CCCC   set the current coordinates for the four points of an element
    C_COOR(1,1)=COORDS(1,1)+U(1)
    C_COOR(2,1)=COORDS(2,1)+U(2)
    C_COOR(1,2)=COORDS(1,2)+U(3)
    C_COOR(2,2)=COORDS(2,2)+U(4)
    C_COOR(1,3)=COORDS(1,3)+U(5)
    C_COOR(2,3)=COORDS(2,3)+U(6)
    C_COOR(1,4)=COORDS(1,4)+U(7)
    C_COOR(2,4)=COORDS(2,4)+U(8)

CCCC     compute the rotation angle
    P1_X=(C_COOR(1,1)+C_COOR(1,4))/2.0D0
    P1_Y=(C_COOR(2,1)+C_COOR(2,4))/2.0D0
    P2_X=(C_COOR(1,2)+C_COOR(1,3))/2.0D0
    P2_Y=(C_COOR(2,2)+C_COOR(2,3))/2.0D0

    IF(ABS(P2_X-P1_X).LE.1.0E-10) THEN
        FI=3.14159265/2.0D0
    ELSE
        FI=ATAN((P2_Y - P1_Y)/(P2_X - P1_X))
    ENDIF

CCCC     compute the coordinates in local coordinate system
    R_COOR(1,1)=C_COOR(1,1)*COS(FI) + C_COOR(2,1)*SIN(FI)
    R_COOR(2,1)=-1.0D0*C_COOR(1,1)*SIN(FI) + C_COOR(2,1)*COS(FI)
    R_COOR(1,2)=C_COOR(1,2)*COS(FI) + C_COOR(2,2)*SIN(FI)
    R_COOR(2,2)=-1.0D0*C_COOR(1,2)*SIN(FI) + C_COOR(2,2)*COS(FI)
    R_COOR(1,3)=C_COOR(1,3)*COS(FI) + C_COOR(2,3)*SIN(FI)
    R_COOR(2,3)=-1.0D0*C_COOR(1,3)*SIN(FI) + C_COOR(2,3)*COS(FI)
```

```
      R_COOR(1,4)=C_COOR(1,4)*COS(FI) + C_COOR(2,4)*SIN(FI)
      R_COOR(2,4)=-1.0D0*C_COOR(1,4)*SIN(FI) + C_COOR(2,4)*COS(FI)

CCCCC   compute the relative displacements in local coordinate system

      DUX1=R_COOR(1,4) - R_COOR(1,1)              !U(7)-U(1)
      DUX2=R_COOR(1,3) - R_COOR(1,2)              !U(5)-U(3)
      DUY1=R_COOR(2,4) - R_COOR(2,1) - THIK1_0    !U(8)-U(2)
      DUY2=R_COOR(2,3) - R_COOR(2,2) - THIK2_0    !U(6)-U(4)
      RN_14=DUY1/DLTN
      RT_14=DUX1/DLTT
      RN_23=DUY2/DLTN
      RT_23=DUX2/DLTT

CCCCC     compute the current thickness of the EPZ element
      XXL1=R_COOR(1,1)              !COORDS(1,1)+U(1)
      YYL1=R_COOR(2,1)              !COORDS(2,1)+U(2)
      XXL2=R_COOR(1,4)              !COORDS(1,4)+U(7)
      YYL2=R_COOR(2,4)              !COORDS(2,4)+U(8)
      XXR1=R_COOR(1,2)              !COORDS(1,2)+U(3)
      YYR1=R_COOR(2,2)              !COORDS(2,2)+U(4)
      XXR2=R_COOR(1,3)              !COORDS(1,3)+U(5)
      YYR2=R_COOR(2,3)              !COORDS(2,3)+U(6)
      THIK1_1=SQRT((XXL1-XXL2)**2.0 + (YYL1-YYL2)**2.0)
      THIK2_1=SQRT((XXR1-XXR2)**2.0 + (YYR1-YYR2)**2.0)

CCCCC compute the local stiffness matrix and residual forces for
CC    node pair 1-4

CCCCC check if critical displacement is reached: if either DLTN OR
CC    DLTT is reached, the total stiffness matrix and residual force
CC    will be set to be zero

      IF((RN_14.GT.Q).OR.(ABS(RT_14).GT.Q)) THEN      ! CHT
      TN1=0.0D0
      TT1=0.0D0

      DO 140 I=1,4
        R_MATRX(I,1)=0.0D0
        R_MATRX(I,2)=0.0D0
        R_MATRX(I,7)=0.0D0
        R_MATRX(I,8)=0.0D0
140   CONTINUE

      ELSE
```

```
      IF(SYMBOL_1.GT.1.0D0) THEN                          ! CHT
          TN1=0.0D0
          TT1=0.0D0
      GOTO 146
      ENDIF

CCCCC check the energy fracture criterion
      CALL ENRG_T(RT_14, TCAP, RTT1, RTT2, DLTT, G_IIC, G_II_14, Q)
      CALL ENRG_N(RN_14, SCAP, RTN1, RTN2, DLTN, G_IC, G_I_14, Q)


CC************     failure criteria for node1,4     ************
      G_CRT_14=G_I_14/G_IC + G_II_14/(10.0D0*G_IIC)       ! CHT
CC*************************************************************

      IF (G_CRT_14.GE.1.0D0) THEN
         TN1=0.0D0
         TT1=0.0D0
         SYMBOL_1=10.0D0

      ELSE

CCCCC  compute the stiffness matrix related to node pair 1-4
      CALL SHR(RT_14, TCAP,RTT1, RTT2, DLTT,STRT_14, STFT_14, Q)
      CALL TEN(RN_14, SCAP,RTN1, RTN2, DLTN,STRN_14, STFN_14, Q)
      TN1=STRN_14
      TT1=STRT_14

CCC***************STIFF MATRIX A(1,J), J=1,2,3,4)**************
      R_MATRX(1,1)= ALEN*STFT_14/3.0D0/DLTT
          R_MATRX(1,2)= 0.0D0
      R_MATRX(1,7)= -1.0D0*ALEN*STFT_14/3.0D0/DLTT
          R_MATRX(1,8)= 0.0D0

          R_MATRX(2,1)= 0.0D0
      R_MATRX(2,2)= ALEN*STFN_14/3.0D0/DLTN
          R_MATRX(2,7)= 0.0D0
      R_MATRX(2,8)= -1.0D0*ALEN*STFN_14/3.0D0/DLTN

      R_MATRX(3,1)= ALEN*STFT_14/6.0D0/DLTT
          R_MATRX(3,2)= 0.0D0
      R_MATRX(3,7)= -1.0D0*ALEN*STFT_14/6.0D0/DLTT
          R_MATRX(3,8)= 0.0D0
```

```
        R_MATRX(4,1)= 0.0D0
    R_MATRX(4,2)= ALEN*STFN_14/6.0D0/DLTN
        R_MATRX(4,7)= 0.0D0
    R_MATRX(4,8)= -1.0D0*ALEN*STFN_14/6.0D0/DLTN

      ENDIF

      ENDIF

146 CONTINUE

CCCCC  compute the local stiffness matrix and residual forces for
CC     node pair 2-3

CCCCC  judge if critical displacement is reached: if either DLTN or
CC     DLTT is reached, the total stiffness matrix and residual force
CC     will be set to be zero

    IF((RN_23.GT.Q).OR.(ABS(RT_23).GT.Q)) THEN          ! CHT
        TN2=0.0D0
        TT2=0.0D0

    DO 150 I=1,4
        R_MATRX(I,3)=0.0D0
        R_MATRX(I,4)=0.0D0
        R_MATRX(I,5)=0.0D0
        R_MATRX(I,6)=0.0D0
150 CONTINUE

    ELSE

    IF(SYMBOL_2.GT.1.0D0) THEN
        TN2=0.0D0
        TT2=0.0D0
    GOTO 199
    ENDIF

CCCC    check the energy fracture criterion

    CALL ENRG_T(RT_23, TCAP, RTT1, RTT2, DLTT, G_IIC, G_II_23, Q)
    CALL ENRG_N(RN_23, SCAP, RTN1, RTN2, DLTN, G_IC, G_I_23, Q)

CC************     failure criteria for node2,3     ************
    G_CRT_23=G_I_23/G_IC + G_II_23/(10.0D0*G_IIC)       ! CHT
CC*************************************************************
```

```
      IF (G_CRT_23.GE.1.0D0) THEN                                ! CHT
          TN2=0.0D0
          TT2=0.0D0
          SYMBOL_2=10.0D0

      ELSE

CCCCC  compute the stiffness matrix related to node pair 2,3
      CALL SHR(RT_23, TCAP,RTT1, RTT2, DLTT,STRT_23, STFT_23, Q)
      CALL TEN(RN_23, SCAP,RTN1, RTN2, DLTN,STRN_23, STFN_23, Q)

      TN2=STRN_23
      TT2=STRT_23

      R_MATRX(1,3)= ALEN*STFT_23/6.0D0/DLTT
          R_MATRX(1,4)= 0.0D0
      R_MATRX(1,5)= -1.0D0*ALEN*STFT_23/6.0D0/DLTT
          R_MATRX(1,6)= 0.0D0

          R_MATRX(2,3)= 0.0D0
      R_MATRX(2,4)= ALEN*STFN_23/6.0D0/DLTN
          R_MATRX(2,5)= 0.0D0
      R_MATRX(2,6)= -1.0D0*ALEN*STFN_23/6.0D0/DLTN

      R_MATRX(3,3)= ALEN*STFT_23/3.0D0/DLTT
          R_MATRX(3,4)= 0.0D0
      R_MATRX(3,5)= -1.0D0*ALEN*STFT_23/3.0D0/DLTT
          R_MATRX(3,6)= 0.0D0

          R_MATRX(4,3)= 0.0D0
      R_MATRX(4,4)= ALEN*STFN_23/3.0D0/DLTN
          R_MATRX(4,5)= 0.0D0
      R_MATRX(4,6)= -1.0D0*ALEN*STFN_23/3.0D0/DLTN

      ENDIF
      ENDIF

199 CONTINUE

      DO 200 I=1,8
          R_MATRX(5,I)=-1.0D0*R_MATRX(3,I)
          R_MATRX(6,I)=-1.0D0*R_MATRX(4,I)
          R_MATRX(7,I)=-1.0D0*R_MATRX(1,I)
          R_MATRX(8,I)=-1.0D0*R_MATRX(2,I)
```

```
200 CONTINUE

CCCCC  compute the residual forces in local coordin. sys.
    R_F(1)=(TT1*ALEN/3.0D0+TT2*ALEN/6.0D0)
    R_F(2)=(TN1*ALEN/3.0D0+TN2*ALEN/6.0D0)
    R_F(3)=(TT1*ALEN/6.0D0+TT2*ALEN/3.0D0)
    R_F(4)=(TN1*ALEN/6.0D0+TN2*ALEN/3.0D0)
    R_F(5)=-R_F(3)
    R_F(6)=-R_F(4)
    R_F(7)=-R_F(1)
    R_F(8)=-R_F(2)

CCCCC  form the global stiffness matrix and residual force
    DO 300 I=1,7,2
    DO 300 J=1,7,2
    AMATRX(  I,  J)  = R_MATRX(  I,  J)*COS(FI)**2.0D0  +
     1                 R_MATRX(I+1,J+1)*SIN(FI)**2.0D0  -
     2                 R_MATRX(  I,J+1)*SIN(FI)*COS(FI) -
     3                 R_MATRX(I+1,  J)*SIN(FI)*COS(FI)

    AMATRX(I+1,  J) = R_MATRX(  I,  J)*SIN(FI)*COS(FI) -
     1                R_MATRX(I+1,J+1)*SIN(FI)*COS(FI) -
     2                R_MATRX(  I,J+1)*SIN(FI)**2.0D0  +
     3                R_MATRX(I+1,  J)*COS(FI)**2.0D0

    AMATRX(  I,J+1) = R_MATRX(  I,  J)*SIN(FI)*COS(FI) -
     1                R_MATRX(I+1,J+1)*SIN(FI)*COS(FI) +
     2                R_MATRX(  I,J+1)*COS(FI)**2.0D0  -
     3                R_MATRX(I+1,  J)*SIN(FI)**2.0D0


    AMATRX(I+1,J+1) = R_MATRX(  I,  J)*SIN(FI)**2.0D0  +
     1                R_MATRX(I+1,J+1)*COS(FI)**2.0D0  +
     2                R_MATRX(  I,J+1)*SIN(FI)*COS(FI) +
     3                R_MATRX(I+1,  J)*SIN(FI)*COS(FI)

300 CONTINUE

    DO 310 I=1,7,2
       RHS( I ,1)=R_F(I)*COS(FI) - R_F(I+1)*SIN(FI)
       RHS(I+1,1)=R_F(I)*SIN(FI) + R_F(I+1)*COS(FI)
310 CONTINUE

    SVARS(1)=SYMBOL_1
    SVARS(2)=SYMBOL_2
```

```
      do 500 i=64, 192
      ke=1+(i-1)
      IF(JELEM.EQ.ke) THEN
      write(16,*)'**************',KINC,'******************'
      write(16,'(i5)')JELEM
      write(16,*)'G_I_14, G_II_14, G_I_23, G_II_23'
      write(16,'(4f10.5)')G_I_14,G_II_14,G_I_23,G_II_23
c     write(16,*)' G_CRT_14 ',' G_CRT_23 '
      write(16,'(2f10.5)')G_CRT_14,G_CRT_23
cc    WRITE(16,*)' SYMBOL_1 ', ' SYMBOL_2 '
cc    WRITE(16,'(2F10.5)')SVARS(1), SVARS(2)
      write(16,*)'trac_14, trac_23', TN1, TT1, TN2, TT2
      write(16,*)
      ELSE
      ENDIF
500   continue

      RETURN
      END

CCC ************************************************************
CCC   The following subroutines have been modified to reflect the
C     traction-separation law used in the thesis.  Most details have
C     been changed but the structure follows that of Yang.  -- CHT

      SUBROUTINE SHR(RTT, TAO, RTT1, RTT2, DLTT, STRT, STFT, Q)
      IMPLICIT DOUBLE PRECISION(A-H, O-Z)

      PI=3.14159265D0

      IF(ABS(RTT).LE.RTT2) THEN
          STRT=TAO*SIN(RTT*PI)
          STFT=PI*TAO*COS(RTT*PI)
      GO TO 1000
      ELSE
      ENDIF

      IF((ABS(RTT).GT.RTT2).AND.(ABS(RTT).LE.Q)) THEN
          STRT=TAO*(PI*COS(RTT2*PI)*(ABS(RTT)-RTT2) +
          1   SIN(RTT2*PI))*ABS(RTT)/RTT
          STFT=PI*TAO*COS(RTT2*PI)
      GO TO 1000
      ELSE
      ENDIF
```

```
      IF(ABS(RTT).GT.Q) THEN
          STRT=0.0D0
          STFT=0.0D0
      ELSE
      ENDIF

1000  CONTINUE

      RETURN
      END

CCC ***********************************************************
      SUBROUTINE TEN(RTN, SCAP, RTN1, RTN2, DLTN, STRN, STFN, Q)
      IMPLICIT DOUBLE PRECISION(A-H, O-Z)

      PI=3.14159265D0

      IF(RTN.LE.RTN2) THEN
          STRN=SCAP*SIN(RTN*PI)
          STFN=PI*SCAP*COS(RTN*PI)
      GO TO 2000
      ELSE
      ENDIF

      IF((RTN.GT.RTN2).AND.(RTN.LE.Q)) THEN
          STRN=SCAP*(PI*COS(RTN2*PI)*(ABS(RTN)-RTN2) +
          1   SIN(RTN2*PI))*ABS(RTN)/RTN
          STFN=PI*SCAP*COS(RTN2*PI)
      GO TO 2000
      ELSE
      ENDIF

      IF(RTN.GT.Q) THEN
          STRN=0.0D0
          STFN=0.0D0
      GO TO 2000
      ELSE
      ENDIF

2000  CONTINUE

      RETURN
      END
```

```
CCC ************************************************************
    SUBROUTINE ENRG_N(RTN, SCAP, RTN1, RTN2, DLTN, G_IC, G_I, Q)
    IMPLICIT DOUBLE PRECISION(A-H, O-Z)

    PI=3.14159265D0

    IF(RTN.LE.1.0E-10) THEN
        G_I=0.0D0
    GO TO 3000
    ELSE
    ENDIF

    IF((RTN.GT.1.0E-10).AND.(RTN.LE.RTN2)) THEN
        G_I=(SCAP*DLTN/PI)*(1.0D0-COS(RTN*PI))
    GO TO 3000
    ELSE
    ENDIF

    IF((RTN.GT.RTN2).AND.(RTN.LE.Q)) THEN
        A_TRAP=0.5D0*SCAP*DLTN*(ABS(RTN)-RTN2)*
    1   (2*SIN(RTN2*PI)+PI*COS(RTN2*PI)*(ABS(RTN)-RTN2))
        G_I=SCAP*DLTN*(1.0D0-COS(RTN2*PI))/PI + A_TRAP
    GO TO 3000
    ELSE
    ENDIF

    IF(RTN.GT.Q) THEN
        G_I=G_IC
    GO TO 3000
    ELSE
    ENDIF

3000    CONTINUE

    RETURN
    END

CCC ************************************************************
    SUBROUTINE ENRG_T(RTT, TAO, RTT1, RTT2, DLTT, G_IIC, G_II, Q)
    IMPLICIT DOUBLE PRECISION(A-H, O-Z)

    PI=3.14159265D0

    IF(ABS(RTT).LE.1.0E-10) THEN
        G_II=0.0D0
```

```
        GO TO 4000
      ELSE
      ENDIF

      IF((ABS(RTT).GT.1.0E-10).AND.(ABS(RTT).LE.RTT2)) THEN
          G_II=(TAO*DLTT/PI)*(1.0D0-COS(ABS(RTT)*PI))
          GO TO 4000
      ELSE
      ENDIF

      IF((ABS(RTT).GT.RTT2).AND.(ABS(RTT).LE.Q)) THEN
          A_TRAP=0.5D0*TAO*DLTT*(ABS(RTT)-RTT2)*
     1    (2*SIN(RTT2*PI)+PI*COS(RTT2*PI)*(ABS(RTT)-RTT2))
          G_II=TAO*DLTT*(1.0D0-COS(RTT2*PI))/PI + A_TRAP
      GO TO 4000
      ELSE
      ENDIF

      IF(ABS(RTT).GT.Q) THEN
          G_II=G_IIC
      GO TO 4000
      ELSE
      ENDIF

 4000     CONTINUE

      RETURN
      END
```

Appendix E

ABAQUS code: Bonding simulation

The following is the ABAUQS code used to simulate the bonding process. This model included the stainless steel plate, and used the uniform pressure boundary condition.

```
*HEADING
Symmetric Case
*PREPRINT,HISTORY=NO,MODEL=NO
**
** 11 pads, 0.5um thick, 20 elements/row/pad
**
*NODE
    1,      0.0005,     5.00E-07
    10,     0.0005,     4.51E-04
    280,    0.001,      5.00E-07
    320,    0.001025,   5.00E-07
    400,    0.001275,   5.00E-07
    480,    0.001325,   5.00E-07
    600,    0.001575,   5.00E-07
    680,    0.001625,   5.00E-07
    800,    0.001875,   5.00E-07
    880,    0.001925,   5.00E-07
    1000,   0.002175,   5.00E-07
    1080,   0.002225,   5.00E-07
    1200,   0.002475,   5.00E-07
    1280,   0.002525,   5.00E-07
    1400,   0.002775,   5.00E-07
```

```
1480,   0.002825,   5.00E-07
1600,   0.003075,   5.00E-07
1680,   0.003125,   5.00E-07
1800,   0.003375,   5.00E-07
1880,   0.003425,   5.00E-07
2000,   0.003675,   5.00E-07
2080,   0.003725,   5.00E-07
2200,   0.003975,   5.00E-07
2280,   0.004025,   5.00E-07
2400,   0.004275,   5.00E-07
100280, 0.001,      1.00E-06
100320, 0.001025,   1.00E-06
100400, 0.001275,   1.00E-06
100480, 0.001325,   1.00E-06
100600, 0.001575,   1.00E-06
100680, 0.001625,   1.00E-06
100800, 0.001875,   1.00E-06
100880, 0.001925,   1.00E-06
101000, 0.002175,   1.00E-06
101080, 0.002225,   1.00E-06
101200, 0.002475,   1.00E-06
101280, 0.002525,   1.00E-06
101400, 0.002775,   1.00E-06
101480, 0.002825,   1.00E-06
101600, 0.003075,   1.00E-06
101680, 0.003125,   1.00E-06
101800, 0.003375,   1.00E-06
101880, 0.003425,   1.00E-06
102000, 0.003675,   1.00E-06
102080, 0.003725,   1.00E-06
102200, 0.003975,   1.00E-06
102280, 0.004025,   1.00E-06
102400, 0.004275,   1.00E-06
102600, 0.005,      1.00E-06
200280, 0.001,      4.51E-04
200320, 0.001025,   4.51E-04
200400, 0.001275,   4.51E-04
200480, 0.001325,   4.51E-04
200600, 0.001575,   4.51E-04
200680, 0.001625,   4.51E-04
200800, 0.001875,   4.51E-04
200880, 0.001925,   4.51E-04
201000, 0.002175,   4.51E-04
201080, 0.002225,   4.51E-04
201200, 0.002475,   4.51E-04
```

```
    201280, 0.002525,   4.51E-04
    201400, 0.002775,   4.51E-04
    201480, 0.002825,   4.51E-04
    201600, 0.003075,   4.51E-04
    201680, 0.003125,   4.51E-04
    201800, 0.003375,   4.51E-04
    201880, 0.003425,   4.51E-04
    202000, 0.003675,   4.51E-04
    202080, 0.003725,   4.51E-04
    202200, 0.003975,   4.51E-04
    202280, 0.004025,   4.51E-04
    202400, 0.004275,   4.51E-04
    202600, 0.005,      4.51E-04
    203001, 0.001,      4.51E-04
    203401, 0.005,      4.51E-04
    204001, 0.001,      5.01E-04
    204401, 0.005,      5.01E-04
    224001, 0.001,      0.003451
    224401, 0.005,      0.003451
**
**          --- Create nodes in the pad region ---
**
*NGEN, NSET=padBot
    280,    320,    2
    400,    480,    2
    600,    680,    2
    800,    880,    2
    1000,   1080,   2
    1200,   1280,   2
    1400,   1480,   2
    1600,   1680,   2
    1800,   1880,   2
    2000,   2080,   2
    2200,   2280,   2
*NGEN, NSET=padTop
    100280, 100320, 2
    100400, 100480, 2
    100600, 100680, 2
    100800, 100880, 2
    101000, 101080, 2
    101200, 101280, 2
    101400, 101480, 2
    101600, 101680, 2
    101800, 101880, 2
    102000, 102080, 2
```

```
    102200, 102280, 2
**
*NFILL, NSET=padnodes
    padBot, padTop, 8,  12500
**
**          ---  Create nodes in the wafer ---
*NGEN, NSET=wfspaceBot
    100320, 100400, 2
    100480, 100600, 2
    100680, 100800, 2
    100880, 101000, 2
    101080, 101200, 2
    101280, 101400, 2
    101480, 101600, 2
    101680, 101800, 2
    101880, 102000, 2
    102080, 102200, 2
    102280, 102400, 2
*NGEN, NSET=wfspaceTop
    200320, 200400, 2
    200480, 200600, 2
    200680, 200800, 2
    200880, 201000, 2
    201080, 201200, 2
    201280, 201400, 2
    201480, 201600, 2
    201680, 201800, 2
    201880, 202000, 2
    202080, 202200, 2
    202280, 202400, 2
*NGEN, NSET=wfpadTop
    200280, 200320, 2
    200400, 200480, 2
    200600, 200680, 2
    200800, 200880, 2
    201000, 201080, 2
    201200, 201280, 2
    201400, 201480, 2
    201600, 201680, 2
    201800, 201880, 2
    202000, 202080, 2
    202200, 202280, 2
**
*NFILL, NSET=mwfNodes,  BIAS=0.95
    padTop, wfpadTop,   20, 5000
```

```
    wfspaceBot, wfspaceTop, 20, 5000
**
*NGEN, NSET=endsBot
    102400, 102600, 4
*NGEN, NSET=endsTop
    202400, 202600, 4
**
*NFILL, NSET=endnodes,  BIAS=0.95
    endsBot, endsTop, 20, 5000
**
*NGEN, NSET=ssbot
    203001, 203401, 1
*NGEN, NSET=ssmid
    204001, 204401, 1
*NGEN, NSET=sstop
    224001, 224401, 1
*NFILL
    ssbot,  ssmid,  2, 500
    ssmid,  sstop,  40, 500
**
**          ---  Create reference node sets  ---
**
*NSET, NSET=wfBot
        padTop, wfspaceBot
**
*NSET, NSET=wfTop
        wfpadTop, wfspaceTop
**
*NSET, NSET=Top
    wfTop, endsTop
**
*NSET, NSET=Verts, GENERATE
       280, 100280, 12500
    100280, 200280, 10000
    102600, 202600, 10000
    203001, 224001, 500
*NSET, NSET=p, GENERATE
    203002, 203398, 4
*NSET, NSET=left, GENERATE
    203001, 203397, 4
*NSET, NSET=right, GENERATE
    203005, 203401, 4
*NSET, NSET=mid, GENERATE
    203003, 203399, 4
*MPC
```

```
quadratic, p, left, mid, right
**
** ELEMENTS
**          ---  Create elements in wafer ---
**
*ELEMENT, type=CPE8
    5021,   100280, 100284, 110284, 110280,
            100282, 105284, 110282, 105280
    5951,   102400, 102408, 112408, 112400,
            102404, 107408, 112404, 107400
*ELGEN, ELSET=wafer
    5021,   530, 4, 1,  10, 10000,  1000
    5951,   25,  8, 1,  10, 10000,  1000
**
**          ---  Create elements in pads ---
**
*ELEMENT, type=CPE8
    211,    280,    284,    25284,  25280,
            282,    12784,  25282,  12780
    401,    400,    404,    25404,  25400,
            402,    12904,  25402,  12900
*ELGEN, ELSET=padUnits
    401,    10, 200, 200
*ELGEN, ELSET=pads
    211,    10, 4,  1,  4,  25000,  20
    401,    20, 4,  1,  4,  25000,  20
    601,    20, 4,  1,  4,  25000,  20
    801,    20, 4,  1,  4,  25000,  20
    1001,   20, 4,  1,  4,  25000,  20
    1201,   20, 4,  1,  4,  25000,  20
    1401,   20, 4,  1,  4,  25000,  20
    1601,   20, 4,  1,  4,  25000,  20
    1801,   20, 4,  1,  4,  25000,  20
    2001,   20, 4,  1,  4,  25000,  20
    2201,   20, 4,  1,  4,  25000,  20
**
**          ---  Create elements in plate---
**
*ELEMENT, type=CPE8
    20000, 203001,  203003, 204003, 204001,
           203002,  203503, 204002, 203501
    20200, 204001,  204005, 205005, 205001,
           204003,  204505, 205003, 204501
*ELGEN, ELSET=sselement
    20000,  200,    2,  1
```

```
    20200,  100,    4,  1, 20, 1000, 200
**
**    reference element
*ELSET, ELSET=botPad, GENERATE
    211,    220,    1
    401,    420,    1
    601,    620,    1
    801,    820,    1
    1001,   1020,   1
    1201,   1220,   1
    1401,   1420,   1
    1601,   1620,   1
    1801,   1820,   1
    2001,   2020,   1
    2201,   2220,   1
**
**          ********** Create surfaces **********
**
*ELSET, ELSET=topElements, GENERATE
        14021, 14550, 1
        14951, 14975, 1
*SURFACE, name=wfTopS, type=element
        topElements, S3
**
*ELSET, ELSET=endElbot, GENERATE
        5951, 5975, 1
*SURFACE, name=end-wf, type=element
    endElbot, S1
**
*SURFACE, type=SEGMENTS, NAME=master
    start, 0.0003,  5E-7
    line,    0.0055,    5E-7
*RIGID BODY, ANALYTICAL SURFACE=master, REF NODE=1
**
*ELSET, ELSET=ssBotel, GENERATE
        20000, 20199, 1
*SURFACE, name=ssBotS, type=element
        ssBotel, S1
*Boundary
    1,  ENCASTRE
**
**
*CONTACT PAIR, INTERACTION=symmplane
    end-wf, master
    wfTopS, ssBotS
```

```
*SURFACE INTERACTION, name=symmplane
*friction, slip tolerance=0.02
0.01
**
*ELSET, ELSET=plateTop, GENERATE
    24000, 24099, 1
*SURFACE, name=plateTopS, type=element
        plateTop, S3
**
**          ****************************************
**  MATERIAL PROPERTIES
**
*solid section, ELSET=wafer, material=Si
0.008
*solid section, ELSET=pads, material=Au
0.008
*solid section, ELSET=sselement, material=SS
0.008
**
*Material, name=Si
*Elastic
    1.69e+11, 0.22
*Material, name=Au
*Elastic
    7.0e+10, 0.42
*Plastic
    1.2e+08, 0.
*Material, name=SS
*Elastic
    1.93e11, 0.3
**
**
** BOUNDARY CONDITIONS
**
*Boundary
    padBot, 2, 2
    Verts, 1, 1
**
*STEP
*static, DIRECT
        .3, 1
**
**  load = uniform pressure, P;  -> 120MPa on Au
**
*Dsload
```

```
    plateTopS, P, 15.75e6
**cload
**  224001, 2, -504
**
** OUTPUT REQUESTS
**
*Restart, write
*Node print, NSET=padBot
U2
*Node print, NSET=endsBot
U2
*El print, ELSET=botPad, position=centroidal
S22
**
*END STEP
```

Bibliography

[1] H. Reichl and V. Grosser, "Overview and development trends in the field of MEMS packaging," in *14th IEEE International Conference on MEMS*, (Interlaken, Switzerland), pp. 1–5, 2001.

[2] W. Eaton, S. Risbud, and R. Smith, "Silicon wafer-to-wafer bonding at T < 200°C with polymethylmethacrylate," *Appl. Phys. Lett.*, vol. 65, no. 4, pp. 439–441, 1994.

[3] P. Turmezei *et al.* , "Low-cost microfilter for red blood cell membrane stiffness measurement using photosensitive BCB," in *12th International Conference on Solid State Sensors, Actuator and Microsystems*, (Boston, MA), pp. 107–110, 2003.

[4] H. Kim and K. Najafi, "Wafer bonding using parylene and wafer-level tranfer of free-standing parylene membranes," in *12th International Conference on Solid State Sensors, Actuator and Microsystems*, (Boston, MA), pp. 790–793, 2003.

[5] M. Desponte *et al.* , "Wafer-scale micrdevice transer/interconnect: from a new integration method to its application in an AFM-based data-storage system," in *12th International Conference on Solid State Sensors, Actuator and Microsystems*, (Boston, MA), pp. 1907–1910, 2003.

[6] W. Ko, "Packaging of microfabricated devices and systems," *Mater. Cem. Phys.*, vol. 42, pp. 169–175, 1995.

[7] M. Shimbo, K. Furukawa, K. Fukuda, and K. Tanzawa, "Silicon-to-silicon direct bonding method," *J. Appl. Phys.*, vol. 60, no. 8, pp. 2987–2989, 1986.

[8] J. Lasky, "Wafer bonding for silicon-on-sinsulator technologies," *Appl. Phys. Lett.*, vol. 48, no. 1, pp. 78–80, 1986.

[9] S. Bengtsson, "Semiconductor wafer bonding: A review of interfacial properties and application," *J. Electron. Mater.*, vol. 21, no. 8, pp. 841–862, 1992.

[10] A. Plossl and G. Krauter, "Wafer direct bonding: tailoring adhesion between brittle materials," *Mater. Sci. Eng.*, vol. R25, pp. 1–88, 1999.

[11] H. Tilmans, D. Van de Peer, and E. Beyne, "The indent reflow sealing (IRS) technique – A method for the fabrication of sealed cavities for MEMS devices," *J. Microelectromech. Syst.*, vol. 9, no. 2, pp. 206–217, 2000.

[12] G. Kissinger and W. Kissinger, "Void-free silicon-wafer-bond strengthening in the 200-400 degrees C range," *Sensor Actuator*, vol. A36, no. 2, pp. 149–156, 1993.

[13] S. Bengtsson and P. Amirfeiz, "Room temperature wafer bonding of silicon, oxidized silicon, and crystalline quartz," *J. Electron. Mater.*, vol. 29, no. 7, pp. 909–915, 2000.

[14] C. Gui, M. Elwenspoek, N. Tas, and J. Gardeniers, "The effect of surface roughness on direct wafer bonding," *J. Appl. Phys.*, vol. 85, no. 10, pp. 7448–7454, 1999.

[15] G. Wallis and D. Pomerantz, "Field assisted glass-metal sealing," *J. Appl. Phys.*, vol. 40, no. 10, pp. 3946–3949, 1969.

[16] S. Mack, H. Baumann, and U. Gosele, "Gas tightness of cavities sealed by silicon wafer bonding," in *MEMS 1997*, (Nagoya, Japan), pp. 488–493, IEEE, 1997.

[17] M. Schmidt, "Wafer-to-wafer bonding for microstructure formation," *Proc. IEEE*, vol. 86, no. 8, pp. 1575–1585, 1998.

[18] "Corning Silicon Glass constraint substrates." Available from: http://www.corning.com/lightingmaterials/images/wafersheet.pdf.

[19] K. Schjø lberg Henriksen, J. Plaza, J. Rafi, J. Esteve, F. Campabadal, J. Santander, G. Jense, and A. Hanneborg, "Protection of mos capacitors during anodic bonding," *J. Micromech. Microeng.*, vol. 12, pp. 361–367, 2002.

[20] S. Cho and F. Erdmann, "An on-chip hermetic packaging technology for micromechanical devices," in *Solid-State Sensor and Actuator Workshop*, (Hilton Head, S.C.), pp. 229–232, 1998.

[21] G. Matijasevic, C. Wang, and C. Lee, "Void free bonding of large silicon dice using gold-tin alloys," *IEEE Trans. on Components, Hybrids and Manufacturing Technology*, vol. 13, no. 4, pp. 1128–1134, 1990.

[22] C. Wang and C. Lee, "An eutectic bonding technology at a temperature below the eutectic point," in *42nd Electronic Components and Technology Conference*, (San Diego), pp. 502–507, 1992.

[23] C. Hoge and S. Thomas, "Some considerations of the gold-silicon die bond based on surface chemical analysis," in *18th Annual Proceedings of Reliability Physics*, pp. 301–311, IEEE, 1980.

[24] Y. Li and R. Bower, "Systematic low temperature silicon bonding using pressure and temperature," *Jpn. J. Appl. Phys.*, vol. 37, no. 3A, pp. 737–741, 1998.

[25] A. Sayah, D. Solignac, T. Cueni, and M. Gijs, "Development of novel low temperature bonding technologies for microchip chemical analysis applications," *Sensor Actuat. A-Phys.*, vol. 84, no. 1-2, pp. 103–108, 2000.

[26] M. Waelti, N. Schneeberger, O. Paul, and H. Baltes, "Low temperature packaging of cmos infrared microsystems by Si-Al-Au bonding," in *4th International Symposium on Semiconductor Wafer Bonding: Science, Technology, and Applications.*, (Paris, France), pp. 147–154, 1998.

[27] Y. Cheng, W. Hsu, L. Lin, C. Nguyen, and K. Najafi, "Vacuum packaging technology using localized aluminum/silicon-to-glass bonding," in *14th IEEE International Conference on MEMS*, (Interlaken, Switzerland), pp. 18–21, 2001.

[28] D. Sparks, G. Queen, R. Weston, G. Woodward, M. Putty, L. Jordan, S. Zarabadi, and K. Jayakar, "Wafer-to-wafer bonding of nonplanarized mems surfaces using solder," *J. Micromech. Microeng.*, vol. 11, pp. 630–634, 2001.

[29] J. Jellison, "Effect of surface contamination on the thermcompression bondability of gold," *IEEE Trans. Parts, Hybrids and Packag.*, vol. PHP-11, no. 3, pp. 206–211, 1975.

[30] L. Condra, J. J. Svitak, and A. Pense, "The high temperature deformation properties of gold and thermocomression bonding," *IEEE Trans. Parts, Hybrids Packag.*, vol. PHP-11, no. 4, pp. 290–296, 1975.

[31] Y. Kim, J. Pavuluri, J. White, I. Busch-Vishniac, and G. Masada, "Thermocompression bonding effects on bump-pad adhesion," *IEEE Trans. Comp., Packag., Manufact. Technol. A*, vol. 18, no. 1, pp. 192–199, 1995.

[32] B. Furman and S. Mita, "Gold-gold (Au-Au) thermocompression (TC) bonding of very large arrays," in *42nd Electronic Components and Technology Conference*, pp. 883–889, 1992.

[33] L. Parameswaran, *Silicon pressure sensor using wafer bonding technology.* S.M., MIT, 1993.

[34] A. Drost, G. Klink, S. Scherbaum, and M. Feil, "Simultaneous fabrication of dielectric and electrical joints by wafer bonding," in *SPIE - Micromachined Devices and Components IV*, (Santa Clara, CA), pp. 62–71, 1998.

[35] W. Maszara, G. Goetz, A. Caviglia, and J. McKitterick, "Bonding of silicon wafers for silicon-on-insulator," *J. Appl. Phys.*, vol. 64, no. 10, pp. 4943–4950, 1988.

[36] D. Pasquariello and K. Hjort, "Mesa-spacers: Enabling nondestructive measurement of surface energy in room temperature wafer bonding," *J. Electrochem. Soc.*, vol. 147, no. 6, pp. 2343–2346, 2000.

[37] Q.-Y. Tong, G. Cha, R. Gafiteanu, and U. Gosele, "Low temperature wafer direct bonding," *J. Microelectromecahnical Systems*, vol. 3, no. 1, pp. 29–35, 1994.

[38] P. Charalambides, J. Lund, A. Evans, and R. McMeeking, "A test specimen for determining the fracture resistance of bimaterial interfaces," *J. Appl. Mech.*, vol. 56, no. 1, pp. 77–82, 1989.

[39] C. Tsau, M. Schmidt, and S. Spearing, "Characterization of low temperature, wafer-level gold-gold thermocompression bonds," in *Materials Science of Microelectromechanical Systmes (MEMS) Devices II*, vol. 605, (Boston, MA), pp. 171–176, MRS, 1999.

[40] K. Turner, A. Ayon, D. Choi, B. Miller, and S. Spearing, "Characterization of silicon fusion bonds using a four-point bend specimen," in *Materials Science of Microelectromechanical Systems (MEMS) Devices III*, vol. 657, (Boston, MA), pp. EE6.3.1–EE6.3.6, MRS, 2000.

[41] K. Nakashima, M. Iwami, and A. Hiraki, "Low temperature diffusion of Au into Si in the Si(substrate)-Au(film) system," *Thin Solid Films*, vol. 25, no. 2, pp. 423–430, 1975.

[42] H. Hieber, "Aging properties of gold layers with different adhesion layers," *Thin Solid Films*, vol. 37, no. 3, pp. 335–343, 1976.

[43] K. Masahiro and S. Noboru, "Effects of temperature, thickness and atmosphere on mixing in Au-Ti bilayer thin films," *J. Mater. Sci.*, vol. 28, no. 18, pp. 5088–5091, 1993.

[44] H. Moritz, "Optical single layer lift-off process," *IEEE Trans. Electron Devices*, vol. ED-32, no. 3, pp. 672–676, 1985.

[45] R. W. Berry, P. M. Hall, and M. T. Harris, *Thin Film Technology.* D. Van Nostrand, 1968.

[46] M. Rappaport and B. Berkovitz, "A graphite crucible for spitting-free high rate e-gun evaporation of Ge," *J. Vac. Sci. Technol.*, vol. 21, no. 1, p. 102, 1982.

[47] C. Thompson, "Structure evolution during processing of polycrystalline films," *Annu. Rev. Mater. Sci.*, vol. 30, pp. 159–190, 2000.

[48] D. Porath, Y. Goldstein, A. Grayevsky, and O. Millo, "Scanning tunneling microscopy studies of annealing of gold films," *Surf. Sci.*, vol. 321, pp. 81–88, 1994.

[49] J. Hwang and M. Dubson, "Atomically flat gold films grown on hot glass," *J. Appl. Phys.*, vol. 72, no. 5, pp. 1852–1857, 1992.

[50] J. Blakely, "Mechanical properties of vacuum-deposited gold films," *J. Appl. Phys.*, vol. 35, no. 6, pp. 1756–1759, 1964.

[51] M. Lozinskiy, V. Ferenets, and V. Zinchenko, "Plastic deformation mechanism of gold exposed to heat and tensile stress in vacuo," *Physics of Metals and Metallography*, vol. 28, no. 3, pp. 151–156, 1969.

[52] Y. Choi and S. Suresh, "Size effectsw on teh mechanical properties of thin polycrystalline metal films on substrates," *Acta Mater.*, vol. 50, pp. 1881–1893, 2002.

[53] R. Saha and W. Nix, "Effects of the substrate on the determination of thin film mechanical properties by nanoindentation," *Acta Mater.*, vol. 50, pp. 23–38, 2002.

[54] S. Suresh, *Fatigue of Materials.* Cambridge University Press, 2nd ed., 1998.

[55] O. Leung, A. Munkholm, S. Brennan, and W. Nix, "A search for strain gradients in gold thin films on substrates using x-ray diffraction," *J. Appl. Phys.*, vol. 88, no. 3, pp. 1389–1396, 2000.

[56] J. Hutchinson and Z. Suo, "Mixed mode cracking in layered materials," *Adv. Appl. Mech.*, vol. 29, pp. 63–191, 1992.

[57] P. Charalambides, H. Cao, J. Lund, and A. Evans, "Development of a test method for measuring the mixed mode fracture resistance of bimaterial interfaces," *Mech. Mater.*, vol. 8, pp. 269–283, 1990.

[58] R. Dauskardt, M. Lane, Q. Ma, and N. Krishna, "Adhesion and debonding of multi-layer thin film structures," *Eng. Fract. Mech.*, vol. 61, pp. 141–162, 1998.

[59] A. Evans and B. Dalgleish, "The fracture resistance of metal-ceramic interfaces," *Acta Metall. Mater.*, vol. 40, no. S, p. S295, 1992.

[60] Z. Suo and J. Hutchinson, "Sandwich test specimens for measuring interface crack toughness," *Mater. Sci. Eng.*, vol. A107, pp. 135–143, 1989.

[61] N. Fleck, J. Hutchinson, and Z. Suo, "Crack path selection in a brittle adhesive layer," *Int. J. Solids Structures*, vol. 27, no. 13, pp. 1683–1703, 1991.

[62] N. Klingbeil and J. Beuth, "Interfacial fracture testing of deposited metal layers under four-point bending," *Eng. Fract. Mech.*, vol. 56, no. 1, pp. 113–126, 1997.

[63] S. Howard, A. Phillipps, and T. Clyne, "The interpretation of data from the four-point bend delamination test to measure interfacial fracture toughness," *Composites*, vol. 24, no. 2, pp. 103–112, 1993.

[64] Q. Ma, "A four-point bending technique for studying subcritical crack growth in thin films and at interfaces," *J. Mater. Res.*, vol. 12, no. 3, pp. 840–845, 1997.

[65] M. Lane, R. Dauskardt, A. Vainchtein, and H. Gao, "Plasticity contributions to interface adhesion in thin-film interconnect structures," *J. Mater. Res.*, vol. 15, no. 12, pp. 2758–2769, 2000.

[66] I. Reimanis, "The measurement of crack front profiles in the fracture of Au/Al_2O_3 interfaces," *Acta Mater.*, vol. 46, no. 7, pp. 2479–2484, 1998.

[67] I. Reimanis, B. Dalgleish, M. Brahy, M. Ruhle, and A. Evans, "Effects of plasticity on the crack propagation resistance of a metal/ceramic interface," *Acta Metall. Mater.*, vol. 38, no. 12, pp. 2645–2652, 1990.

[68] I. Reimanis, B. Dalgleish, and A. Evans, "The fracture resistance of a model metal/ceramic interface," *Acta Metall. Mater.*, vol. 39, no. 12, pp. 3133–3141, 1991.

[69] K. Turner, *An evaluation of critical issues for microhydraulic transducers: silicon wafer bonding, strength of silicon on insulator membranes and gold-tin solder bonding.* S.M., MIT, 2001.

[70] R. Tylecote, *The solid phase welding of metals.* New York: St. Martin's Press, 1968.

[71] S. Collard and R. McLellan, "High-temperature elastic constants of gold single-crystals," *Acta Metall. Mater.*, vol. 39, no. 12, pp. 3143–3151, 1991.

[72] C. K. Malek, B. Kebabi, A. Charai, and P. de la Houssaye, "Effect of thermal treatment on the mechanical and structural properties of gold thin films," *J. Vac. Sci. Technol.*, vol. B 9, no. 6, pp. 3329–3332, 1991.

[73] D. Milner and G. Rowe, "Fundamentals of solid-phase welding," *Metallurgical Reviews*, vol. 7, no. 28, pp. 433–480, 196.

[74] K. Turner. private communication.

[75] M. James and D. Swenson, "FRANC2D/L: A crack propagation simulator for plane layered structures." Available from: http://www.mne.ksu.edu/~franc2d/.

[76] M. Thouless and Q. Yang, "Measurement and analysis of the fracture properties of adhesive joints," in *Adhesion Science and Engineering* (D. Dillard, A. Pocious, and M. Chaudhury, eds.), vol. 1, pp. 235–271, Elsevier Science Ltd., 2001.

[77] Q. Yang, M. Thouless, and S. Ward, "Elastic-plastic mode-II fracture of adhesive joints," *Int. J. Solids Struct.*, vol. 38, pp. 3251–3262, 2001.

[78] Q. Yang and M. Thouless, "Mixed-mode fracture analyses of plastically deforming adhesive joints," *Int. J. Fracture*, vol. 110, pp. 175–187, 2001.

[79] Hibbitt, Karlsson, and Sorensen, Inc. ABAQUS version 6.3.

[80] H.-S. Moon. private communication.